

USL Report No. 747

AD 638133

# Effects of Pressure Gradients On Turbulent Boundary-Layer Wall-Pressure Fluctuations

HOWARD H. SCHLOEMER  
*Special Developments Branch*  
*Submarine Sonar Division*



CLEARINGHOUSE FOR FEDERAL SCIENTIFIC AND TECHNICAL INFORMATION			
Hardcopy	Microfiche		
\$3.00	\$0.75	89	22
ARCHIVE COPY			

code 1

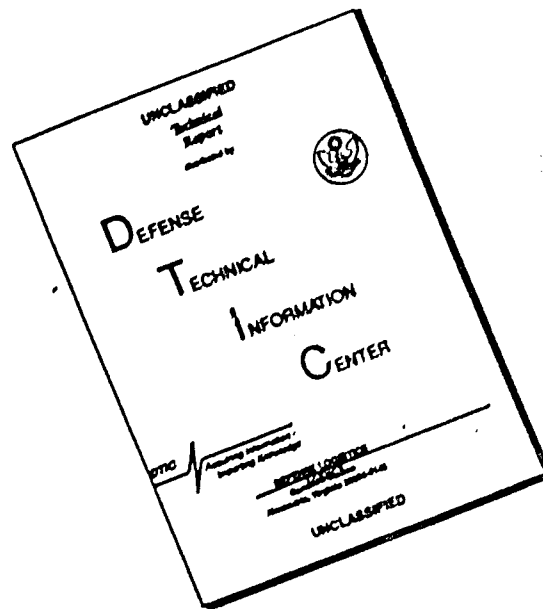
1 July 1966

DDC  
SEP 14 1966  
B

Distribution of this document is unlimited.

U. S. Navy Underwater Sound Laboratory  
Fort Trumbull, New London, Connecticut

# DISCLAIMER NOTICE



THIS DOCUMENT IS BEST QUALITY AVAILABLE. THE COPY FURNISHED TO DTIC CONTAINED A SIGNIFICANT NUMBER OF PAGES WHICH DO NOT REPRODUCE LEGIBLY.

## ABSTRACT

The low-turbulence subsonic wind tunnel at Stevens Institute of Technology was significantly modified so that turbulent boundary-layer pressure fluctuation measurements could be made with adequate signal-to-noise ratio over a wide frequency range. Measurements were made in a mild adverse and a mild favorable pressure gradient with natural transition occurring in the boundary layer. To make certain that the facility was operating correctly and to establish a basis for comparison, the zero-pressure gradient case was investigated. For this case, the spectral density, magnitude of the normalized longitudinal and lateral cross-spectral density functions, and convection velocity as a function of longitudinal separation and frequency were in excellent agreement with other experimenters.

When comparison is made to the zero-pressure gradient in the same non-dimensionalized frequency band and at similar non-dimensionalized longitudinal spacings, the convection velocity ratio is higher in the favorable and lower in the adverse pressure gradients, primarily due to the change in shape of the mean velocity profile. As in the zero-pressure gradient case, the increase in convection velocity with increasing longitudinal separation and decrease with increasing frequency was observed for both the adverse and favorable pressure gradient. The longitudinal decay of a particular frequency component was more rapid for the adverse gradient and slower for the favorable gradient than for the zero-pressure gradient, as indicated by the magnitude of the normalized longitudinal cross-spectral density measured for each gradient. Within the experimental accuracy of the measurements no differences were found for the magnitude of the normalized lateral cross-spectral density due to the pressure gradients imposed.

The effect of an adverse pressure gradient on the non-dimensionalized spectral density is to increase the low-frequency content without influencing the high-frequency portion appreciably, when compared to the zero-pressure gradient case. As expected the root-mean-square values (for a broad frequency band) are greater in the adverse pressure gradient when non-dimensionalized with respect to free stream dynamic pressure. The major change due to the favorable pressure gradient is a sharp decrease in the high-frequency content, with a resultant lowering of the root-mean-square values. The spectral densities were corrected for finite pressure transducer size, using Corcos' correction factors.

Qualitative agreement with theoretical predictions by White, as to the effects of favorable and adverse pressure gradients, was found for convection velocities, including the effects of spatial separations and frequency, and the general shape of the magnitude of the normalized longitudinal and lateral cross-spectral density curves.

SECTION FOR \_\_\_\_\_

WHITE SECTION ☒

BUFF SECTION ☐

RESERVED ☐

NOTIFICATION.....

.....

.....

.....

SECTION/AVAILABILITY CODES

ST.	AVAIL. and/or SPECIAL
2	

**REVIEWED AND APPROVED: 1 July 1966**

**H. E. Nash**  
**Technical Director**

*R. L. Corkran, Jr.*  
R. L. Corkran, Jr., Captain, USN  
Commanding Officer and Director

## **ADMINISTRATIVE INFORMATION**

This study was originally prepared as a dissertation submitted in partial fulfillment of the requirements for the degree of Doctor of Science in Mechanical Engineering at Stevens Institute of Technology. The work was accomplished under USL Project No. 1-052-00-00 and Navy Sub-project and Task No. SR 011 01 01-0401.

## **ACKNOWLEDGMENT**

The author wishes to thank Professor R. J. Nickerson, of the Stevens Institute of Technology, for serving as his thesis adviser and Professor F. Sisto for his valuable criticism and discussion. He is also grateful to E. Rakowsky for use of the wind tunnel and for his assistance in construction of the muffler.

The author is indebted to the U. S. Navy Underwater Sound Laboratory, particularly G. F. Carey, for support and assistance in all phases of the work. The cooperation of J. J. Libuha in setting up the instrumentation is gratefully acknowledged.

## TABLE OF CONTENTS

Chapter		Page
	ADMINISTRATIVE INFORMATION . . . . .	i
	LIST OF ILLUSTRATIONS . . . . .	v
	LIST OF TABLES . . . . .	vii
	LIST OF SYMBOLS . . . . .	ix
1	INTRODUCTION . . . . .	1
2	EXPERIMENTAL FACILITY . . . . .	4
3	INSTRUMENTATION . . . . .	9
4	DESCRIPTION OF MEAN FLOW . . . . .	12
5	FREQUENCY SPECTRA . . . . .	15
6	CORRELATIONS . . . . .	21
	Measurements of Convection Velocities and Longitudinal Cross	
	Spectral Density . . . . .	25
	Lateral Cross Spectral Measurements . . . . .	29
7	ACCURACY OF THE EXPERIMENTAL MEASUREMENTS . . . . .	30
8	CONCLUSIONS . . . . .	32
	APPENDIX . . . . .	34
	LIST OF REFERENCES . . . . .	76
	INITIAL DISTRIBUTION LIST	Inside Back Cover

## LIST OF ILLUSTRATIONS

<u>Figure</u>	<u>Page</u>
1. Schematic of Subsonic Wind Tunnel . . . . .	36
2. Muffler Details . . . . .	37
3. Muffler and Diffuser Attenuation as a Function of Frequency . . . .	38
4. Flat Plate and Leading Edge Details . . . . .	39
5. Comparison of Experimental Laminar Velocity Profile to Blasius Profile . . . . .	40
6. Transducer Mounting Details . . . . .	41
7. Vibration Isolation of Transducer Mount from Aluminum Plate . . .	42
8. Schematic of Airfoil Sections Used in Obtaining Pressure Gradients . . . . .	43
9. Typical Vertical Velocity Profile Upstream of Transducer Location ( $U_{\infty} = 105$ ft/sec at transducer location) Adverse Pressure Gradient	44
10. Typical Horizontal Velocity Profile ( $U_{\infty} = 105$ ft/sec at transducer location) Adverse Pressure Gradient . . . . .	45
11. Block Diagram of Instrumentation System . . . . .	46
12. Typical Non-Dimensional Velocity Profile for the Zero Pressure Gradient . . . . .	47
13. Typical Non-Dimensional Velocity Profile for the Adverse Pressure Gradient . . . . .	48
14. Typical Non-Dimensional Velocity Profile for the Favorable Pressure Gradient . . . . .	49
15. Universal Mean Velocity Profile for the Zero Pressure Gradient . . . . .	50
16. Universal Mean Velocity Profile for the Adverse Pressure Gradient . . . . .	51
17. Universal Mean Velocity Profile for the Favorable Pressure Gradient . . . . .	52

# LIST OF ILLUSTRATIONS (cont)

<u>Figure</u>		<u>Page</u>
18.	Typical Static Pressure Distribution for the Zero Pressure Gradient . . . . .	53
19.	Typical Static Pressure Distribution for the Adverse Pressure Gradient . . . . .	54
20.	Typical Static Pressure Distribution for the Favorable Pressure Gradient . . . . .	55
21.	Shape Factor as a Function of Reynolds Number . . . . .	56
22.	Comparison of Spectrum Levels for Each Pressure Gradient to Ambient and Apparent Spectrum Level due to Acceleration Response of Pressure Transducer . . . . .	57
23.	Comparison of Non-Dimensional Spectral Density for the Zero Pressure Gradient to Other Investigators . . . . .	58
24.	Non-Dimensional Spectral Density for the Zero Pressure Gradient . . . . .	59
25.	Non-Dimensional Spectral Density for the Adverse Pressure Gradient . . . . .	60
26.	Non-Dimensional Spectral Density for the Favorable Pressure Gradient . . . . .	61
27.	Longitudinal Turbulence Intensity Profiles in the Zero, Adverse and Favorable Pressure Gradients . . . . .	62
28.	Convection Velocities as a Function of Frequency at Different Longitudinal Separations for the Zero Pressure Gradients . . . . .	63
29.	Convection Velocities as a Function of Frequency and Non-Dimensional Longitudinal Separation for the Zero-Pressure Gradient . . . . .	64
30.	Convection Velocities as a Function of Frequency at Different Longitudinal Separations for the Adverse Pressure Gradient . . . . .	65
31.	Convection Velocities as a Function of Frequency and Non-Dimensional Longitudinal Separations for the Adverse Pressure Gradient . . . . .	66
32.	Convection Velocities as a Function of Frequency at Different Longitudinal Separations for the Favorable Pressure Gradient . . . . .	67
33.	Convection Velocities as a Function of Frequency and Non-Dimensional Longitudinal Separation for the Favorable Pressure Gradient . . . . .	68

## LIST OF ILLUSTRATIONS (cont)

<u>Figure</u>		<u>Page</u>
34.	Broad-Band Convection Velocities as a Function of Pressure Gradient and Longitudinal Separation . . . . .	69
35.	Magnitude of the Normalized Longitudinal Cross-Spectral Density for the Zero Pressure Gradient . . . . .	70
36.	Magnitude of the Normalized Longitudinal Cross-Spectral Density for the Favorable Pressure Gradient . . . . .	71
37.	Magnitude of the Normalized Longitudinal Cross-Spectral Density for the Adverse Pressure Gradient . . . . .	72
38.	Magnitude of the Normalized Lateral Cross-Spectral Density for the Zero Pressure Gradient . . . . .	73
39.	Magnitude of the Normalized Lateral Cross-Spectral Density for the Favorable Pressure Gradient . . . . .	74
40.	Magnitude of the Normalized Lateral Cross-Spectral Density for the Adverse Pressure Gradient . . . . .	75

## LIST OF TABLES

<u>Table</u>		<u>Page</u>
1.	Properties of Turbulent Boundary Layers . . . . .	14
2.	Comparison of Transducer Size to Boundary-Layer Thickness . . .	20
3.	Root-Mean-Square Values of Pressure Fluctuations at the Wall in Broad Frequency Bands . . . . .	20



## LIST OF SYMBOLS

<u>English</u>	
a, b	real and imaginary parts of the longitudinal cross spectral density
db	decibel
A	magnitude of the normalized longitudinal cross spectral density
B	magnitude of the normalized lateral cross spectral density
$C_f$	skin friction coefficient
f	frequency in hertz
H	boundary layer shape factor $\frac{\delta^*}{\theta}$
$k_c, k_\infty$	turbulence wave numbers
p	fluctuating wall pressure
$\sqrt{p_E^2}, \sqrt{p_I^2}$	root-mean-square acoustic pressure measured at muffler exit and test section, respectively
$q_\infty$	freestream dynamic pressure
r	active radius of transducer face
$R_\theta$	Reynolds number based on momentum thickness $\frac{U_\infty \theta}{\nu}$
t	time
U	local mean velocity
$U_c$	longitudinal convection velocity
$U_\infty$	freestream velocity
$U^*$	shear stress velocity = $\sqrt{\frac{\tau_w}{\rho}}$
$\sqrt{u^2}, \sqrt{v^2}, \sqrt{w^2}$	root mean square value of turbulent velocity fluctuations in x, y and z directions, respectively
x, y	longitudinal and lateral space coordinates

# LIST OF SYMBOLS (cont)

## Greek

$$\sqrt{a_r^2}, \sqrt{a_e^2}$$

root mean square acceleration, designating the response and excitation values, respectively

$\delta$

boundary layer thickness, point at which  $\frac{U}{U_\infty} = .99$

$\delta_A$

average boundary layer thickness  $\delta_A = \frac{\delta_1 + \delta_2}{2}$   
where  $\delta_1$  and  $\delta_2$  are the boundary layer thickness at the high and low speeds for the pressure gradient in question.

$\delta^*$

boundary layer displacement thickness  $\int_0^\delta (1 - \frac{U}{U_\infty}) dy$

$\eta$

lateral separation between transducers

$\theta$

boundary layer momentum thickness  $\int_0^\delta \frac{U}{U_\infty} (1 - \frac{U}{U_\infty}) dy$

$\lambda_\xi$

longitudinal microscale

$\mu$

viscosity

$\nu$

kinematic viscosity

$\xi$

longitudinal separation between transducers

$\rho$

density

$\tau$

time delay

$\tau_{MAX}$

time delay between upstream and downstream transducer which maximizes correlation between them

$\tau_w$

wall shear stress

$$\Phi(f) = \frac{\overline{p^2}}{\text{Bandwidth}}$$

where  $\overline{p^2}$  is the mean square pressure within the bandwidth, measured

$\Phi(\omega)$

spectral density also  $\frac{\Phi(f)}{2\pi}$  (see equation (5))

$\omega$

angular frequency

## CHAPTER 1

### INTRODUCTION

Since the advent of high-speed aircraft and submarines, the noise generated by turbulence has created many problems and stirred much interest, both theoretical and experimental. Panel flutter, internal cabin noise in aircraft, flow-induced structural vibrations, and masking of sonar-sensing elements in high-speed submarines by intense local noise fields are examples of the effects of surface pressure fluctuations created in the turbulent boundary layer. The last two effects are responsible for a marked decrease in the range at which a sonar target can be detected and are therefore of importance to the military. In almost every case the speed of the body moving through the fluid is sufficiently high to induce rapid transition in the boundary layer from laminar to turbulent flow. Hence, knowledge of the frequency spectrum and some of the statistical properties of wall pressure fluctuations in a turbulent boundary layer is essential in solving the aforementioned problems.

Pressure gradients are imposed on the turbulent boundary layer by the motion of the body in a fluid. An appropriate question would be "What are the effects, if any, of pressure gradients on the properties and spectrum of the wall pressure fluctuations"? The present work will attempt to evaluate some of these effects for adverse and favorable pressure gradients.

The statistical properties and frequency spectrum of the wall pressure fluctuations in subsonic two-dimensional zero-pressure gradient flow have been measured by several experimenters, (namely Willmarth and Wooldridge,<sup>1</sup> Bull,<sup>2</sup> Skudrzyk & Haddle<sup>3</sup>). Bakewell (et al),<sup>4</sup> Corcos,<sup>5</sup> Bull and Willis<sup>6</sup> and VonWinkle<sup>7</sup> have made similar measurements for fully developed turbulent pipe flow. The relatively weak favorable pressure gradient created in pipe flow produced no discernible difference between zero

pressure gradient (in the subsonic flow case) and pipe flow measurements. Except for a few isolated measurements, such as Murphy, (et al)<sup>8</sup> in an adverse pressure gradient at a Mach number of 3.46, no consistent experimental measurements in either favorable or adverse pressure gradients are available in the literature. All of the theoretical predictions<sup>9,10,11,12</sup> to date, for incompressible turbulent shear flow except for White,<sup>13</sup> have neglected or not considered the effect of pressure gradients on the surface pressure fluctuations. White's paper, which is based on some work done by Gardner<sup>14</sup>, is of special interest since he presents results of the important statistical properties such as longitudinal and lateral cross spectral density and the effect of spacing and frequency on convection velocities, as well as frequency spectra. Agreement between White's predictions and experimental data for the zero pressure gradient case, except for frequency spectra, is qualitatively good.

One of the major effects of a pressure gradient is to distort the turbulent velocity profile; thus, White's predictions of the effect on the convection velocity ratio due to different velocity profiles is of considerable interest. Further theoretical work by White<sup>15</sup> indicated the effect of adverse and favorable pressure gradients on the frequency spectrum and important statistical properties. These will be discussed later and compared at least qualitatively to experimental results.

To undertake a systematic experimental study of the effects of pressure gradients on turbulent wall pressure fluctuations, a suitable facility was needed. Fortunately, a facility (low speed subsonic wind tunnel at Stevens Institute of Technology) existed which, with major modifications and additions, would be suitable for this study. Some of the major requirements of such a facility are:

1. The turbulent boundary layer should be developed with natural transition on a smooth surface. Willmarth and Wooldridge<sup>1</sup> and Bull and Willis<sup>6</sup> indicate the higher noise levels observed with tripping the boundary layer. Skudrzyk & Haddle<sup>3</sup> and Willmarth & Wooldridge<sup>1</sup> indicate that the effects of roughness on the

frequency spectrum are undesirable, because roughness increases the pressure fluctuation level, particularly at high frequencies.

2. Interference from extraneous disturbances should be eliminated or reduced to tolerable levels. These requirements, though obvious, are difficult to achieve because of the great care and effort required to attain meaningful attenuations of low-frequency acoustic noise and structural vibrations. Electromagnetic radiation is always a problem when large amplifications are required because of the small size and correspondingly poor sensitivity of the pressure transducer.

3. Adequate signal-to-noise ratio must be maintained. Part of this requirement is actually contained in (2) above, i. e., total elimination of all unwanted disturbances would guarantee a sufficient signal-to-noise ratio for almost any flow velocity. The problem may be solved from the other direction, by creating very high flow velocities and not attempting to reduce noise levels. In most cases adequate signal-to-noise ratio is obtained by "trading off" an increase in muffler attenuation against a decrease in flow velocity for the same blower horsepower and noise. Therefore the muffler and other noise suppressing devices must be designed for a very small static pressure drop with sufficient acoustic attenuation.

4. Flow in the test section should be uniform, free of large vortices and secondary flows, with low free-stream turbulence. This is a prerequisite in obtaining a representative turbulent boundary layer for comparison with the work of other investigators.

5. The method of introducing adverse and favorable pressure gradients should not create excessive noise or flow interference.

The five requirements outlined above were fulfilled with the completed wind tunnel at Stevens Institute of Technology. The existing tunnel and instrumentation necessary to carry out the research program are described in the next two chapters.

## CHAPTER 2

### EXPERIMENTAL FACILITY

The basic facility is a subsonic, induction-type wind tunnel at Stevens Institute of Technology, as shown in Fig. 1. This facility, except for the muffler, was designed by Rakowsky<sup>16</sup> and constructed by him with major assistance by the author. To ensure uniform, low-turbulence flow, an inlet with a 15-to-1 contraction ratio was built. Prevention of boundary-layer separation at the edges of the 5 x 6-foot entrance was attained by using 28-inch-diameter paper cylinders, which produced a rectangular "doughnut" shaped entrance. One inch back from the intersection of the paper cylinder and wall of the contraction, some 3300 paper cylinders, 1-1/4-inch in diameter and 10-inches long, were glued in place to form a flow straightener. Two 60-mesh screens, separated by 1-5/8 inches, were mounted 13 inches downstream of the straightener tubes. Following this was the contraction to the 1 x 2-foot test section of the tunnel.\*

The test sections were constructed of 3/4-inch plywood, with two 1 x 2-foot plexiglass windows on each side; these windows were removable for installation of probes and other equipment. Various other access ports for static pressure taps and probes were provided in the top and bottom sections.

To reduce structure-borne vibrations (particularly in the floor), the inlet and working sections were suspended by steel cables, from pipes placed across the ceiling joists. This arrangement also allowed a section to be easily moved aside to permit installation of large pieces (flat plate, for instance) and cleaning of screens.

---

\*Additional information concerning the design and checkout of the tunnel may be found in Reference 16.

Aft of the test sections, a 2-foot-long, canvas vibration isolation section was attached and covered with 4 inches of fiberglass wool mounted on the inside of a box constructed of 3/4-inch plywood. A 1-inch layer of fiberglass was glued on the outside of the plywood box. This resulted in an effective decoupler which was also shielded from the exhaust noise of the blowers.

The diffuser, muffler, and blower sections were mounted on a steel framework with wheels which rode on flat steel strips secured to the floor to facilitate moving these heavy sections. Four jack screws located at the corners of each section were used for leveling and steadying the diffuser, muffler, and blower boxes, when the tunnel was ready for operation.

Following the vibration isolation section the flow was diffused to a 24 x 36-inch cross-sectional area in a 3-foot long unlined plywood transition section, cantilevered from the large diffuser section. The 8-foot main section of the diffuser was contoured internally to follow the streamlines established in the cantilevered section. (Refer to Fig. 1.) To reduce the transmission of sound from the blowers, the 8-foot section of the diffuser was lined with 4 inches of PF 612 fiberglass wool (2-1/2 lb per cubic ft) having a Noise Reduction Coefficient of 0.95. Addition of the fiberglass reduced the exit cross-sectional area to 40 x 40 inches, but this was still sufficient to reduce the flow velocity and obtain a large static pressure recovery.

To further reduce acoustic noise from the blower, a muffler, shown in Fig. 2, was designed and constructed of 3/4-inch plywood and 4-inch-thick PF 612 fiberglass. To maintain the large cross-sectional area for air flow, and still achieve high attenuations, the muffler was divided longitudinally by two vertical partitions. This increased the effective length for sound absorption as described in Beranek,<sup>17</sup> while permitting a very small static pressure drop across the muffler.

The attenuation of the muffler and diffuser combination was measured under no flow conditions by driving a speaker with "pink" noise and measuring the output with a

**General Radio Type 1551-B Sound Level Meter.** The speaker was placed at the exit plane of the muffler with the sound level meter 16 inches inside the muffler, and the speaker output was recorded. The sound level meter was then moved into the test section at the pressure transducer location and its output recorded. The difference between these two readings is the attenuation of the muffler and diffuser combination. Several different locations of the speaker in the exit plane of the muffler and locations of the sound level meter in the muffler were used in attaining an average attenuation, the results being displayed in Fig. 3. The major portion of the attenuation with a peak at about 1200 Hz is caused by the smaller lateral dimensions in each longitudinal section of the muffler. A second, smaller peak at about 270 Hz is attributed to the larger lateral dimension of the diffuser (40 inches as compared to 8-1/2 inches). The muffler was attached to the diffuser and blower section by a 4-inch canvas strip with a 16-foot-long zipper sewn in the middle of it. This permitted a particular section to be uncoupled easily and quickly for inspection or maintenance.

Two 7.5-hp. Hartzell vane, axial blowers rated at 7700 C. F. M. at 1.35 in. H<sub>2</sub>O provided the flow necessary to obtain sufficiently high velocities in the test section. They were mounted on steel cross-members in a 4 x 4 x 6 foot box of 3/4-inch plywood which was lined with a 4-inch-thick layer of PF 612 fiberglass. A plexiglass window was installed on the top and provided a means of flow control by allowing air to be bled in when desired.

Since a naturally developed turbulent boundary layer on a smooth surface was desired, it was decided to use a flat plate in the test section of the tunnel. The tunnel floor was too rough and presented pressure transducer mounting problems, particularly in obtaining a flush surface and freedom from vibrations.

After unsuccessful attempts, with several different leading edges and plates, to obtain a suitable laminar velocity profile, such as a Blasius profile just downstream of the leading edge for the zero-pressure gradient case, the flat plate and



leading edge configuration shown in Fig. 4 was evolved and proved successful. The velocity profile was obtained and its comparison to a Blasius profile is shown in Fig. 5. The laminated rear section of the plate was made of three 0.125-inch-thick pieces of aluminum, cemented together with Carbolite S-1 under 2,000-psi pressure for 24 hours. No precise measurements were made as to the improvement in damping characteristics of the laminated section, but the section sounded "dead" when struck with a mallet as compared to the "live" ringing tone of a solid piece of aluminum when struck. The joint between the solid and laminated portions was oil lapped, so that the boundary layer at this point was not disturbed. Rubber stripping and vinyl tape sealed the edges of the plate for its entire length, so that there was no air leakage from beneath it. This retarded the formation of secondary flows and helped to preserve the two-dimensional character of the flow.

Even with a stiff aluminum plate and a damped rear section, the vibration levels were still high enough to mask some of the pressure fluctuation signal from the transducers. To overcome this problem, and to make certain that the transducer was sensing turbulent boundary-layer pressure fluctuations and not the acceleration of the plate, a unique rubber isolation mount was designed by the author. Details of the mount are shown in Fig. 6. The natural frequency of the mount was approximately 90 Hz and its acceleration transmissibility as a function of frequency is displayed in Fig. 7. Further evidence will be presented in Chapter 5 to demonstrate that the vibration levels at the inner plug were sufficiently low so that, within the frequency band used, essentially only wall-pressure fluctuations were measured.

To obtain both favorable and adverse pressure gradients, several different methods were contemplated or attempted. A method using sucking or blowing of additional air was rejected as being too noisy and complicated. Use of a thick rubber sheet as a flexible top wall was attempted, but excessive stretching of the rubber and air leakage doomed this attempt. The pressure gradients were finally produced by two half-airfoil

sections attached to the top wall of the tunnel as shown in Fig. 8. The half sections were made of masonite screwed to two pieces of 2 x 6-inch wood, cut to either a NACA 0015 or NACA 0021 profile. The hollow space was filled with rubberized hair packing material and the edges taped to prevent air leakage due to the pressure differential imposed by the pressure gradient. Except for the boundary layers developed on the four walls, the flow at the transducer location was uniform and two-dimensional. This was true for zero, adverse, and favorable pressure gradients. Typical vertical and horizontal profiles are shown in Figs. 9 and 10 for the adverse pressure gradients with one fan operating. The horizontal profile was measured several inches downstream of the vertical profile, accounting for the slight difference in free-stream velocity. The static pressure distributions, as measured by the 42 taps along the plate, are presented in Chapter 4 along with boundary-layer, velocity-profile measurements.

The experimental facility just described provided a means of establishing a naturally developed turbulent boundary layer on a smooth flat plate and imposing on it adverse and favorable pressure gradients. Incorporation of mufflers and vibration isolation and damping devices reduced the structure and air-borne vibrations produced by the blowers to levels which did not contaminate the measurements of the properties of the turbulent wall-pressure fluctuations.

### CHAPTER 3

#### INSTRUMENTATION

Velocity fluctuations and mean velocity profiles were measured with a constant temperature hot-wire anemometer (Disa Type 55A01), using platinum-plated, tungsten wires, 5 microns in diameter. A small total head tube with a rectangular open area of 0.004 by 0.040 inches was also used in conjunction with wall static pressure in determining the flow velocity. Movement of the probes was accomplished by a traversing mechanism which could accurately resolve distances down to 0.0001 inches. Further details concerning the velocity measuring instrumentation can be found in Rakowsky<sup>16</sup>.

Wall-pressure fluctuation measurements were made with Atlantic Research type LD 107-M transducers, flush-mounted in a vibration isolation mount as described in Chapter 2, which used a lead zirconate titanate ceramic disk 0.060 inches in diameter with the following nominal characteristics:

sensitivity =  $-120 \text{ db//1V/}\mu\text{bar}$  or  $1\mu\text{V/}\mu\text{bar}$

frequency range = 90 to 20,000 Hz

capacitance = 40 picofarads

The accelerometers used in measuring the vibrations were Endevco Model 2226 with the following nominal characteristics:

sensitivity in peak mV/peak g = 4.90

frequency range = 20 to 4000 Hz. Flat to within  $\pm 3\%$

capacitance = 301 picofarads

The pressure transducers used were calibrated by three different methods:

1. Comparison to a known standard. This was accomplished by comparing frequency spectra obtained by both the test and standard transducers in the turbulent

pipe flow facility at the U.S. Navy Underwater Sound Laboratory in New London, Connecticut. The facility is described in Bakewell.<sup>4</sup>

2. Mounting the transducer in a special adapter and using a Bruel and Kjaer Type 4220 Pistonphone to determine the sensitivity.

3. By the tap test, described in Gilchrist and Strawderman,<sup>24</sup> to determine the effective radius and also the broad-band sensitivity.

Results for the transducer used in taking the spectral data by method 1. were: sensitivity 90 Hz to 5000 Hz, -118 db//1V/ $\mu$ bar; 5000 to 20,000 Hz -117 db//1V/ $\mu$ bar. Pistonphone calibration from 250 to 800 Hz yielded a value of -118 db//1V/ $\mu$ bar. An effective radius of 0.0317 inches and a broad band sensitivity of -121 db//1V/ $\mu$ bar were determined by the tap test. The sensitivity used for the frequency spectral calculations were those obtained by methods 1. and 2., as these were considered the more reliable.

Frequency spectrums were obtained by boosting the signal from the LD 107-M transducer with an Ithaco Model No. 114 fixed gain preamplifier (40 db) before using a General Radio Sound and Vibration Analyzer Type 1554-A and Graphic Level Recorder Type 1521-A to complete the analysis. The narrow frequency band (8%) was used for all wall-pressure measurements, which were then corrected to spectrum level, i. e., the mean square wall pressure contained in a one hertz wide frequency band, expressed in decibels.

Accelerations as a function of frequency were obtained in the same manner except on some runs an Endevco Model No. 2607 fixed gain preamplifier (40 db) was used.

Data to be correlated were recorded on magnetic tape, using two identical channels of instrumentation as shown in Fig. 11. Each channel consisted of an LD 107-M transducer and a matching Ithaco preamplifier, a Daven decade attenuator, and Burr-Brown and Keithley amplifiers. Recordings were made with a specially modified 7-channel Ampex FR 1100 tape recorder capable of F.M. operation out to 20,000 Hz at a 60 ips tape speed. The reels of tape were then replayed on the same machine and the signals passed through two matched Gertsch 1/2 octave filters and two Ithaco Model

225A variable gain amplifiers to obtain the proper signal level for the filter bank used, before being processed by a GPS Analog Computer. Both auto- and cross-correlations were performed on this computer, using program 6-1-052, at the U. S. Navy Underwater Sound Laboratory.

Frequent calibrations of each channel showed that the system response was linear and flat from 100 to 20,000 Hz and was in phase between channels throughout this frequency range.

## CHAPTER 4

### DESCRIPTION OF MEAN FLOW

In all three pressure gradient cases the turbulent boundary layer was developed with natural transition. The turbulence level as determined by measuring the free-stream longitudinal turbulence intensity and assuming isotropy, i. e.,  $\frac{\sqrt{3u'^2}}{U_\infty} \approx \frac{\sqrt{u'^2 + v'^2 + w'^2}}{U_\infty} \leq 0.2\%$  indicating that a low turbulence level was attained. Hot wire measurements made ahead of the test location, for each freestream gradient, showed that the boundary layer was fully developed with zero intermittency. Velocity profiles were obtained using both the hot wire anemometer and the total head probe. The total head probe was used for the pressure gradient measurements, since the narrow space between the airfoil section and plate (3.6 inches) prevented the free vertical motion of the hot wire support and probe.

For the zero-pressure gradient case both the hot wire and total pressure methods were used with negligible differences between them.

Non-dimensionalized velocity profiles taken over the transducer mount are presented in Figs. 12, 13, and 14 for the highest speed in the three pressure gradient cases. Velocity profile at different speeds for a particular pressure gradient case were similar.

Measurements taken just forward and aft of the transducer mount demonstrated that the mounting arrangement produced no noticeable effect in the shape of the velocity profile. The profiles at the upstream and downstream locations were the same for a particular pressure gradient.

The agreement between the data and Clauser's universal law for the zero-pressure gradient case is excellent up to  $(\frac{yU^*}{\nu}) = 1000$  as seen in Fig. 15. Beyond this point

it shows a slight departure which is in general agreement with other investigators as given by Clauser<sup>18</sup> and Robertson<sup>19</sup>.

For the moderate adverse pressure gradient (see Fig. 16) the profile follows the law of the wall up to  $(\frac{yU^*}{\nu}) = 500$  and then has the characteristic upward trend as displayed by Coles<sup>20</sup>.

The experimental points for the favorable pressure gradient as displayed in Fig. 17 lie along Clauser's curve up to  $(\frac{yU^*}{\nu}) = 600$  and then decrease slowly after this, similar to other favorable pressure gradient data presented by Coles.

The static pressure distribution was measured along the plate for several speeds in each pressure gradient. Typical distributions are shown for the zero, adverse and favorable pressure gradients in Figs. 18, 19 and 20 respectively.

Properties of turbulent boundary layers are presented in Table 1. The shape factor as a function of  $R_\theta$  for the zero and favorable pressure gradients is within the range of values for a large number of experimental measurements compiled by Robertson as shown in Fig. 21. The curve shown (Ross 1953) represents the mean of a large number of experimental investigations with zero pressure gradient.

As seen in Table 1 the pressure gradient parameter was approximately the same for both speeds in the adverse pressure gradients. Similarly, a smaller negative value of the parameter is constant for both speeds in the favorable pressure case. Because of this fact most of the data presented are for these speeds, with occasional pressure fluctuation measurements at an intermediate speed.

	Adverse Pressure Gradient		Favorable Pressure Gradient		Zero Pressure Gradient	
	105	143	134	157	79	105
$U_{\infty}$ FT/SEC						
$\delta$ INCHES	1.102	1.006	0.356	0.406	1.100	1.050
$\delta^*$ INCHES	0.227	0.207	.0276	.0263	0.1583	0.1535
$\theta$ INCHES	0.144	0.131	.0204	.0192	0.1175	0.114
H	1.577	1.585	1.35	1.37	1.345	1.34
$C_f$	.00182	.00176	.0047	.0045	.0031	.0030
$R_{\theta}$	7,380	9,180	1340	1470	4500	5800
$\tau_w$ LB/FT <sup>2</sup>	.0224	.0416	.0962	.1261	.0221	.0384
$\frac{\theta}{\tau_w} \frac{dp}{dx}$	2.12	2.07	-.218	-.216	-	-
$\delta/\delta^*$	4.86	4.86	12.9	14.7	6.95	6.97

Table 1  
Properties of Turbulent Boundary Layers



## CHAPTER 5

### FREQUENCY SPECTRA

To insure that adequate signal-to-noise ratio existed for the frequency spectral measurements, both the ambient noise and acceleration of the pressure transducer were measured. The ambient noise was measured with the tunnel not running and is essentially a measure of the electronic noise in the pressure transducer and accompanying amplification system. As seen in Fig. 22, the ambient noise was low enough so that the signal plus noise minus noise level of at least 10 db was maintained for the zero-pressure gradient data except at 10,000 Hz. The spectral levels for the lowest speeds in each pressure gradient were about 3 db lower than the highest speed shown in Fig. 22. For this reason the zero-pressure gradient data above 6300 Hz for the lowest speed were not included in the non-dimensionalized spectral density curve, as the signal-to-noise ratio was less than 10 db. A signal plus noise minus noise level of 10 db results in less than a 0.5 db correction to be subtracted from the signal plus noise to obtain the signal level. This results from the fact that the ambient or background noise is uncorrelated with the pressure fluctuations. Further discussion of this may be found in Peterson and Gross.<sup>21</sup> The precision of the frequency measurement was less than 0.5 db so that for this study a signal plus noise minus noise level difference of 10 db was considered a signal-to-noise ratio of 10 db, and to be adequate.

The acceleration of the brass plug containing the pressure transducers total weight 375 grams was measured with an accelerometer weighing 2.8 grams glued on to the bottom surface of the plug. The apparent acoustic spectrum level due to acceleration response of the pressure transducer was determined by the following procedure: the acceleration response of the transducer was determined by rigidly mounting it in a fixture and then driving it with a shaker. By subtracting the pressure transducer acoustic sensitivity

from this, a relation between acoustic level in  $\mu\text{bar}$ , and acceleration in g's was obtained. For the transducer used, the values were  $-67 \text{ db}/1\text{V/g} - (-118 \text{ db}/1\text{V}/1\mu\text{bar}) = 51 \text{ db}/1\mu\text{bar/g}$ . Since the acceleration of the transducer as a function of frequency was known, the apparent spectrum level ( $\text{db}/1\mu\text{bar}^2/\text{Hz}$ ) was computed using the above relation.

The apparent spectrum level due to accelerations of the transducer as a function of frequency is depicted on Fig. 22 for the favorable pressure gradient at the highest speed. The apparent spectrum level due to accelerations of the pressure transducer dropped off sharply after 2500 Hz and is not shown, since the ambient level is much higher and controls the background noise after 1000 Hz. The acceleration spectra for the zero, adverse, or favorable pressure gradient at the highest speed for each gradient (two-fan operation) were essentially similar. Hence the curve shown is representative of all three gradients for two-fan operation. Spectrum levels for two-fan operation for each gradient are presented so that appropriate comparison between the two curves can be made. Two-fan operation was selected for presentation after inspection of the data had revealed it to be the worst case, i.e., the difference between the apparent spectrum levels and actual spectrum levels measured by the pressure transducers was least. Thus, at the lower speeds the frequency range is not reduced as much because of the acceleration of the transducer. The frequency spectrum for the zero-pressure gradient case is truncated at 250 Hz, as shown, to maintain a 10-db signal-to-noise ratio, with the apparent spectrum level as background. For the same reason the data for the adverse pressure gradient are eliminated below 160 Hz. Acceleration response of the transducer was not critical for the favorable pressure gradient as its frequency spectrum was terminated at 1000 Hz because of acoustic noise, as explained in the next paragraph.

A measure of the acoustic noise as a function of frequency inside the tunnel at the test section while it was running was obtained by correlation techniques described in Chapter 6. This measurement revealed that for the adverse and zero-pressure gradient,

effects of blower noise was not a problem above 150 Hz. For the favorable pressure gradient, blower noise along with other extraneous noise was present up to about 900 Hz. The decrease in spectrum level with frequency due to the thin boundary layer in the favorable pressure gradient case (note the downward trend in Fig. 22) is masked sooner by the blower noise. For the favorable pressure gradient the frequency spectrum below 900 Hz was not repeatable and appeared to be very sensitive to extraneous disturbances. A very slight misalignment of the transducer mount or a loose piece of tape in the immediate area caused a 5 or 10 db rise (in the frequency spectrum) at various frequencies below 900 Hz. Despite great care in alignment of the transducer and use of a different central brass plug with fewer transducers mounted in it, the spectra below 900 Hz were still not repeatable. For these reasons the spectral information presented in Figs. 22 and 26 is confined to the range 1,000 to 20,000 Hz for the favorable gradient.

The non-dimensionalized spectral density for the zero-pressure gradient in the frequency range 250 and 10,000 Hz was measured for comparative purposes. Comparison to other investigators as shown in Fig. 23 is excellent. The spectrum is shown in Fig. 24 plotted against several different ordinates and abscissas. The corrections for transducer size were omitted for clarity but in all cases they are about the same and match the corrected curve shown in Fig. 24. The Willmarth curve was corrected for experimental error as described by Willmarth.<sup>22</sup> This agreement along with other evidence to be presented in following chapters proves that turbulent boundary-layer pressure fluctuations were measured within the frequency range indicated. The spectral curves corrected for transducer size were obtained by using the correction factors developed theoretically by Corcos<sup>23</sup> and verified experimentally by Gilchrist and Strawderman.<sup>24</sup> Further discussion may be found in the Appendix.

The non-dimensionalized spectral density curve for the adverse pressure gradient (Fig. 25) is practically identical to the zero pressure gradient (Fig. 24) at the high non-dimensional frequencies for  $\frac{x}{\delta^*} \geq 0.4$ . This is true when comparison is made on

the  $10 \log_{10} \left[ \frac{\rho(f)}{\rho^2 \delta^* U_\infty^3} \right]$  vs.  $\frac{f \delta^*}{U_\infty}$  coordinates. The spectrum level for the adverse pressure gradient is higher, particularly at the lower frequencies, as the turbulent longitudinal intensity  $\sqrt{u^2}/U_\infty$  is greater than that for the zero-pressure gradient boundary layer over the inner two-thirds of the boundary layer as shown in Fig. 27. Based on the hypothesis that the convection velocity is the local mean speed of the noise producing turbulent eddies (as will be discussed in Chapter 6) most of the pressure fluctuations measured at the wall originate within the inner region of the boundary layer.

White's theory predicts that the pressure fluctuation spectral density depends primarily on the details of the velocity fluctuation profile as a function of  $y/\delta$ . To verify this premise experimentally, measurements of  $\sqrt{u^2}$ ,  $\sqrt{v^2}$  and  $\sqrt{w^2}$  would have to be made as a function of  $y/\delta$  along with wall-pressure fluctuation measurements. As only the longitudinal turbulence intensities were measured by Rakowsky,<sup>16</sup> in all three types of pressure gradients these were assumed to be indicative of the variation of  $\sqrt{u^2 + v^2 + w^2}/3U_\infty$  across the boundary layer. This assumption seems reasonable, based on measurements of turbulence intensities by Sandborn and Slogar<sup>23</sup> as well as Schubauer and Klebanoff<sup>24</sup>. The longitudinal turbulence intensity is presented for the zero, adverse, and favorable pressure gradients in Fig. 27. Their differences are discussed in conjunction with the explanation for the changes in the pressure fluctuation spectral density due to the imposed pressure gradients. Because of the space limitations mentioned previously the turbulent intensity for the adverse and favorable pressure gradients were measured 4 inches forward of the transducer location. This accounts for the slightly different free stream velocities in the adverse and favorable pressure gradient cases.

The favorable pressure gradient spectral density (see Fig. 26) reveals a sharp decrease of level at non-dimensional frequencies greater than  $\frac{f \delta^*}{U_\infty} = 0.1$ . This same trend is evident when comparison is made to the zero-pressure gradient spectral density with the aid of the  $\frac{f \delta}{U_\infty}$  scale. That is, the difference in the spectra between the zero and favorable pressure gradient cases cannot be explained on the basis of  $-\frac{\delta}{\delta^*}$ . The value of  $-\frac{\delta}{\delta^*}$  for the favorable pressure gradient is about 14 as compared to the zero pressure gradient value of approximately 7. Examination of the longitudinal turbulent intensity (Fig. 27) reveals that it is lower for the entire boundary layer indicating perhaps less energy for the entire frequency range. This explains, at least partially, the differences in spectral density between the favorable and zero pressure gradients. Another reason for the rapid decrease with frequency is that more averaging of the pressure fluctuations by the finite sized pressure transducer occurs because of their smaller scale at a higher frequency. Note that the spectral curve corrected for transducer size is noticeably higher in this case as compared to the other pressure gradients, with the corrections increasing rapidly with increasing frequency.

An indication of the effects of transducer size on pressure fluctuation measurements is the ratio  $\frac{r}{\delta}$  or  $\frac{r}{\delta^*}$ . Corcos<sup>(25)</sup> states that for the corrections to be valid, the ratio  $\frac{r}{\delta}$  must be sufficiently low, but he does not mention a numerical value. Gilchrist and Strawderman<sup>(26)</sup> used  $\frac{r}{\delta}$  ratios of .051 to .0193 and confirmed Corcos' theoretical prediction within the accuracy of the experiment. Comparison of these ratios to those of other investigations, as tabulated in Table 2, indicates a satisfactorily low value for the zero and adverse pressure gradient case.

Investigator	$r/\delta$	$r/\delta^*$	Pressure Distribution
Bakewell (1962)	0.0193	--	Pipe flow
Willmarth (1965)	0.0160	0.165	Zero
Bull (1963)	unknown	0.185 to 0.0875	Zero
Schloemer (1966)	0.0295	0.203	Zero
	0.0295	0.146	Adverse
	0.0832	1.18	Favorable

Table 2

## Comparison of Transducer Size to Boundary Layer Thickness

When all the pressure gradients are compared on the basis of  $\tau_w$ , i. e.,  $10 \log_{10} \left[ \phi(f) U_\infty / \delta^* \tau_w^2 \right]$  vs.  $\frac{f \delta^*}{U_\infty}$ , the difference in spectra is more pronounced, due primarily to the difference in wall shear. The root-mean-square pressure levels within the frequency bands indicated are shown in Table 3 for the three different pressure gradients. They were obtained by integration of the non-dimensional spectral density.

Pressure Gradient	Frequency Band Hz	$\sqrt{p^2}/q_\infty$	$\sqrt{p^2}/q_\infty$ (corrected)	$\sqrt{p^2}/\tau_w$	$\sqrt{p^2}/\tau_w$ (corrected)
Zero	250-10,000	0.00463	0.00520	1.46	1.63
Favorable	1000-20,000	0.00362	0.00502	0.78	1.09
Adverse	160-20,000	0.00585	0.00775	3.73	4.35

Table 3

## Root-Mean-Square Value of Pressure Fluctuations at the Wall in Broad Frequency Bands

## CHAPTER 6

### CORRELATIONS

Since the mean value, auto-correlation and cross-correlation of the wall-pressure fluctuations do not vary with time under steady flow conditions, these fluctuations may be considered as stationary random processes. Some of the properties of stationary random functions will therefore be employed in their description.

The cross-correlation of the wall-pressure fluctuation is defined as:

$$R(\xi, \eta, \tau) = \lim_{T \rightarrow \infty} \frac{1}{T} \int_0^T P(x, y, t) P(x + \xi, y + \eta, t + \tau) dt$$

Special cases of this are the longitudinal cross-correlation  $R(\xi, 0, \tau)$ , lateral cross-correlation  $R(0, \eta, \tau)$ , and auto-correlation  $R(0, 0, \tau)$ . Using Fourier transforms the following quantities are defined:

Longitudinal cross spectral density:

$$\Gamma(\xi, 0, \omega) = \frac{1}{2\pi} \int_{-\infty}^{\infty} R(\xi, 0, \tau) e^{-i\omega\tau} d\tau \quad (1)$$

Inversion:

$$R(\xi, 0, \tau) = \int_{-\infty}^{\infty} \Gamma(\xi, 0, \omega) e^{i\omega\tau} d\omega \quad (2)$$

Lateral cross-spectral density.

$$\Gamma(0, \eta, \omega) = \frac{1}{2\pi} \int_{-\infty}^{\infty} R(0, \eta, \tau) e^{-i\omega\tau} d\tau \quad (3)$$

Inversion:

$$R(0, \eta, \tau) = \int_{-\infty}^{\infty} \Gamma(0, \eta, \omega) e^{i\omega\tau} d\omega \quad (4)$$

Spectral density.

$$\Phi(\omega) = \frac{1}{2\pi} \int_{-\infty}^{\infty} R(0, 0, \tau) e^{-i\omega\tau} d\tau, \quad (5)$$

Inversion:

$$R(0, 0, \tau) = \int_{-\infty}^{\infty} \Phi(\omega) e^{i\omega\tau} d\omega, \quad (6)$$

Also note that the mean-square pressure is related to the spectral density by

$$\overline{p^2} = R(0, 0, 0) = \int_{-\infty}^{\infty} \Phi(\omega) d\omega. \quad (7)$$

The longitudinal cross-spectral density, Eq. (1), may be rewritten in polar form as

$$R(\xi, 0, \tau) = \int_{-\infty}^{\infty} |\Gamma(\xi, 0, \omega)| e^{i(\omega\tau + \alpha)} d\omega, \quad (8)$$

with  $|\Gamma(\xi, 0, \omega)| = \sqrt{a^2 + b^2}$  and  $\alpha = \tan^{-1}(-\frac{b}{a})$ ,

where  $a$  and  $b$  are the real and imaginary parts of  $\Gamma(\xi, 0, \omega)$

Since  $R(\xi, 0, \tau)$  is real, it may be reduced to

$$R(\xi, 0, \tau) = \int_{-\infty}^{\infty} |\Gamma| \cos(\omega\tau + \alpha) d\omega. \quad (9)$$

Corcos<sup>5</sup> and others have shown that when boundary-layer noise (which is nearly "white" in narrow frequency bands) is passed through two identical ideal narrow-band filters of bandwidth  $w$  having a center frequency of  $\omega_0$ , the cross-correlation may be expressed as:

$$R_w(\xi, 0, \tau) = w |\Gamma(\xi, 0, \omega_0)| \frac{\sin \frac{w}{2}(\tau + \theta)}{\frac{w}{2}(\tau + \theta)} \cos \omega_0(\tau + \theta), \quad (10)$$

where  $\alpha = \omega\theta$ .



When  $\tau = -\phi$ ,  $R_w(\xi, 0, \tau)$  is a maximum, as the absolute value of  $\Gamma(\xi, 0, \omega)$  is independent of the phase angle  $\phi$ , this particular value of  $\phi$  will be referred to as  $\tau_{MAX}$ . Physically  $\tau_{MAX}$  may be described as  $\frac{\xi}{U_c}$ , where  $U_c$  is an effective longitudinal convection velocity. Hence, at the point of interest  $\tau = \frac{-\xi}{U_c}$ , Eq. (10) may be expressed as:

$$R_w(\xi, 0, -\frac{\xi}{U_c}) = w |\Gamma(\xi, 0, \omega_0)|. \quad (11)$$

Normalizing Eq. (11), by noting that

$$R_{wx}(0, 0, 0) = R_{w(x+\xi)}(0, 0, 0) = w |\Gamma(0, 0, \omega_0)| = w \Phi(\omega_0),$$

assuming that points  $x$  and  $(x + \xi)$  are sufficiently close so that the boundary layer and mean-square wall pressure have not changed appreciably, results in:

$$\frac{R_w(\xi, 0, -\frac{\xi}{U_c})}{\sqrt{R_{wx}(0, 0, 0) R_{w(x+\xi)}(0, 0, 0)}} = \frac{w |\Gamma(\xi, 0, \omega_0)|}{w \Phi(\omega_0)} \quad (12)$$

$A(\frac{\omega \xi}{U_c})$  is defined as

$$A(\frac{\omega \xi}{U_c}) = \frac{|\Gamma(\xi, 0, \omega)|}{\Phi(\omega)}. \quad (13)$$

Thus  $A(\frac{\omega \xi}{U_c})$  is the magnitude of the normalized longitudinal cross spectral-density.

This function was measured experimentally by using Eq. (12), i.e., the signal from the upstream pressure transducer was delayed so that maximum correlation with the downstream transducer was obtained. The convection velocity  $U_c$  was determined by dividing the longitudinal separation distance  $\xi$  by  $\tau_{MAX}$ , the time measured from  $\tau = 0$  to the maximum peak. The correlation was normalized with respect to the mean-square pressure for the frequency band in question.

The lateral cross-correlation after narrow-band filtering may be written, with the aid of Eq. (10), as:

$$R_w(o, \eta, \tau) = w |\Gamma(o, \eta, \omega_o)| \frac{\sin \frac{w}{2} (\tau + \theta)}{\frac{w}{2} (\tau + \theta)} \cos \omega_o (\tau + \theta). \quad (14)$$

For two-dimensional flow, as would be expected on physical grounds,  $\theta = 0$  or the "convection" velocity in the lateral direction is infinite. This has been confirmed by the present measurements. With this change Eq. (14) is condensed to:

$$R_w(o, \eta, \tau) = w |\Gamma(o, \eta, \omega_o)| \frac{\sin \frac{w}{2} \tau}{\frac{w}{2} \tau} \cos \omega_o \tau. \quad (15)$$

The maximum value occurs at  $\tau = 0$ , so that Eq. (12) may be rewritten for the lateral case as:

$$\frac{R_w(o, \eta, 0)}{\sqrt{R_{wy}(o, o, 0) R_{w(y+\eta)}(o, o, 0)}} = \frac{w |\Gamma(o, \eta, \omega_o)|}{w \Phi(\omega_o)} \quad (16)$$

and the ratio  $B(\frac{\omega \eta}{U_\infty})$  defined as:

$$B(\frac{\omega \eta}{U_\infty}) = \frac{|\Gamma(o, \eta, \omega)|}{\Phi(\omega)}. \quad (17)$$

The function  $B(\frac{\omega \eta}{U_\infty})$ , the magnitude of the normalized lateral cross-spectral density, was determined experimentally by correlating the output of two transducers spaced a distance  $\eta$  apart and normalizing the maximum peak  $\tau = 0$  with respect to the mean-square pressure for the frequency band of interest.

Physically the function  $A(\frac{\omega \xi}{U_c})$  indicates the decay or loss of coherence of the pressure producing sources or eddies as they progress downstream. Similarly, the function  $B(\frac{\omega \eta}{U_\infty})$  measures the lateral decay or decrease of coherence of the eddies in the

direction normal to the flow. The implied dependence of these functions on  $\frac{\omega \xi}{U_c}$  or  $\frac{\omega \eta}{U_\infty}$  only is somewhat misleading. It neglects a dependence on some non-dimensional frequency of the flow, say  $\frac{\omega \delta^*}{U_\infty}$  or  $\frac{\omega \delta}{U_\infty}$ . This point has been discussed by Corcos<sup>27</sup> and Bull<sup>2</sup>. White<sup>13</sup> has shown theoretically that the  $\frac{\omega \delta}{U_\infty}$  effect on the function  $A(\frac{\omega \xi}{U_c})$  is slight for values of  $\frac{\omega \delta}{U_\infty}$  greater than 2.5. The effect on the function  $B(\frac{\omega \eta}{U_\infty})$  is not as pronounced. That is, values of  $\frac{\omega \delta}{U_\infty}$  within the range of  $1.25 \leq \frac{\omega \delta}{U_\infty} < 10.0$  do not appreciably alter the magnitude or shape of the curve  $B(\frac{\omega \eta}{U_\infty})$  when plotted against  $\frac{\omega \eta}{U_\infty}$ .

### MEASUREMENTS OF CONVECTION VELOCITIES AND LONGITUDINAL CROSS SPECTRAL DENSITY

The spacing between transducers was varied from 0.200 to 1.220 inches for each pressure gradient. Measurements of longitudinal cross-spectral density and convection velocities were made in 1/2-octave bands with the frequency range determined by keeping the signal-to-noise ratio at 25 db or better. A signal-to-noise ratio of 25 db reduces the true magnitude of the correlation peak by 5.3%. For the typical ranges used this reduces the correlation by about 3 to 4%. This is roughly equivalent to the experimental error of  $\pm 3\%$  when the same tapes are run through the correlation system several times. The frequency range used (1/2-octave band center frequencies) was 360 to 4000 Hz for the adverse, 715 to 4000 Hz for the zero, and 2860 to 11,400 Hz for the favorable pressure gradients. It was necessary to use a 550-Hz high pass filter for some of the zero and favorable pressure gradient runs to improve the signal-to-noise ratio at the lower frequencies.

Convection velocity ratio  $U_c/U_\infty$  as a function of  $\frac{\omega \delta^*}{U_\infty}$  and  $\frac{\omega \delta}{U_\infty}$  and non-dimensional separation distances  $\frac{\xi}{\delta^*}$  is shown for the zero pressure gradients in Fig. 28. Comparison to Bull<sup>2</sup> shows good agreement when it is realized that Bull's data is a mean curve for two non-dimensional separation distances and he showed no systematic differences between  $\frac{\xi}{\delta^*} = 1.66$  or 3.07. The zero-pressure gradient data confirms again two interesting characteristics of the wall pressure field, which are:

1. Convection velocity is a function of non-dimensional frequency based on some boundary layer thickness parameter either  $\delta$  or  $\delta^*$ . This can be explained by realizing that small eddies, (those associated with higher frequencies) must physically exist closer to the wall in the lower velocity region of the boundary layer. Appropriately, the larger eddies would have a faster effective speed or convection velocity. Fig. 28 shows that the decrease of convection velocity with increasing frequency occurs for all the separation distances used. Another method of depicting this dependence is to non-dimensionalize the separation distance with respect to  $k_\infty = \frac{\omega}{U_\infty}$ , a characteristic boundary-layer wave number for the wall pressure. This dependence is illustrated in Fig. 29. By keeping the parameter  $\frac{\omega \xi}{U_\infty}$  approximately constant, which can be interpreted as fixing the ratio of distance traveled to eddy size, independent of the eddy size, the decrease in convection velocity with increasing frequency is more clearly shown.

2. As the longitudinal spacing is increased the convection velocity, in a particular frequency band, increases. The larger eddies in the particular bandwidth measured have a "longer life" than the smaller eddies. Therefore, as the group of eddies travels downstream, the small scale effects die out rapidly and the larger eddies (low frequency - high convection velocities) dominate, thereby indicating an increase in convection velocity with increasing spatial separation. This is true for all the frequency bands measured, as shown in Fig. 30.

The convection velocity ratio  $U_c/U_\infty$  as a function of  $\frac{\omega \delta^*}{U_\infty}$  and  $\frac{\omega \delta}{U_\infty}$  for the adverse pressure gradient is presented in Figs. 30 and 31. For a particular value of  $\frac{\omega \delta}{U_\infty}$  and separation distance, the ratio  $\frac{U_c}{U_\infty}$  is lower than that for the zero pressure gradient case. This is to be expected as the mean velocity ratio  $\frac{U}{U_\infty}$  at some distance  $(\frac{y}{\delta})$  from the wall is less in the adverse pressure gradient than for the corresponding distance  $(\frac{y}{\delta})$  in the zero pressure gradient. The non-dimensional distance  $(\frac{y}{\delta})$  can be used as a very crude approximation of half the non-dimensional eddy size, and the mean velocity at this position, the apparent eddy center, approximates the convection velocity. Wooldridge and

Willmarth<sup>28</sup> and Bull<sup>2</sup> show that the convection speed of a velocity disturbance that is correlated with the wall pressure is the local mean speed. As in the zero-pressure gradient case, the dependence of  $U_c/U_\infty$  on frequency and longitudinal separation is apparent from the results presented. The slower convection speeds agree qualitatively with White's theoretical work for the adverse pressure gradient.

For the favorable pressure gradient the opposite is true, as can be seen from Figs. 32 and 33. Again this follows directly from the explanation above, but here the mean velocity ratio  $U/U_\infty$  in the favorable pressure gradient boundary layer is higher for a fixed  $y/\delta$  than for the same non-dimensional distance in the zero-pressure gradient boundary layer. Again, the dependence of  $U_c/U_\infty$  on frequency and longitudinal separation is shown, and these agree qualitatively with White's predictions.

Broad band convection speeds for the three pressure gradients are shown in Fig. 34 with the zero-pressure gradient case compared to Bull<sup>2</sup>. These indicate, on an "average" basis, the detailed results presented previously: that convection velocities depend on the shape of the mean velocity profile and longitudinal separation.

The magnitude of the normalized longitudinal cross-spectral density for the zero-pressure gradient is compared to that of Willmarth and Wooldridge<sup>1</sup> in Fig. 35 and the agreement is seen to be very good. A dependence on the parameter  $\frac{\omega \delta}{U_\infty}$  as proposed theoretically by White was not found. This is probably due to the high values of  $\frac{\omega \delta}{U_\infty}$  used, namely, between 5 and 21. A convected wave number for the particular frequency component in question can be defined as  $k_c = \frac{\omega}{U_c}$  and this becomes a ratio of distance traveled to wavelength  $\lambda_c$ , i.e.  $\frac{\omega \xi}{U_c} = \frac{2\pi \xi}{\lambda_c}$  where  $\lambda_c f = U_c$ . Hence, for the data examined, the conclusion is drawn that a particular eddy loses coherence in traveling a distance proportional to its "size" or wavelength regardless of its size.

The function A is higher in the favorable pressure gradient than in the zero pressure gradient, for a particular value of  $\frac{\omega \xi}{U_c}$  as seen in Fig. 36. This experimental evidence supports White's theoretical work that the longitudinal cross-spectral density curve for a

favorable pressure gradient should be above that for a zero pressure gradient. As might be expected the opposite is true for the adverse pressure gradient; that is, the function A is lower for a particular value of  $\frac{\omega \xi}{U_c}$ . The measurements bear this out for an adverse pressure gradient as demonstrated in Fig. 37. Again, as in the zero-pressure gradient, no dependence on the parameter  $\frac{\omega \delta}{U_\infty}$  was found for either the adverse or zero-pressure gradient cases. The reasons for this are similar to those proposed for the zero-pressure gradient case, i. e., the boundary-layer thickness Strouhal number ( $\frac{\omega \delta}{U_\infty}$ ) ranged from 4 to 17 for the favorable and 2 to 10 for the adverse pressure gradient.

Physically the change in the function A between the adverse, zero, and favorable pressure gradients is due primarily to the differences in convection velocities between them. For a fixed non-dimensional distance from the wall ( $\frac{y}{\delta}$ ) the convection velocity is greater for the favorable gradient, and smaller for the adverse gradient when compared to the zero-pressure gradient case. Using the rough approximation of non-dimensional eddy size (ie.  $\frac{2y}{\delta}$ ), it is seen that the  $\tau_{MAX}$  for a particular eddy is shorter in the favorable gradients than in the others. Hence the correlation is higher for the eddy in question, since its travel or decay time is shorter in the favorable pressure gradient case. For the adverse pressure gradient the opposite is true, i. e., longer delay times and lower values of correlation when compared to the zero-pressure gradient case.

The longitudinal microscale (a rough estimate of the average dimension of the smallest eddies) is obtained by approximating the broad-band auto-correlation function with a parabola near zero  $\tau$ . The intersection of this parabola with the time-delay axis determines the time delay  $\tau_0$ , which, when multiplied by the broad-band convection velocity, yields the longitudinal microscale. By approximating the auto-correlation function  $R(0, 0, \tau)$  about  $\tau = 0$  with a Taylor series expansion, the following relation is obtained:

$$\frac{1}{\lambda^2 \xi} \approx -\frac{1}{U_c^2} \cdot \frac{1}{2P^2} \left[ \frac{\partial^2 R(0, 0, \tau)}{\partial \tau^2} \right]_{\tau=0} \quad (18)$$

By neglecting all but the first two terms which yield a parabola, this curve is fitted to the auto-correlation function for small time delays. For computation purposes, Eq. (18) is rewritten more conveniently as

$$\frac{R(u, u, \tau)}{p^2} = 1 - \left( \frac{\tau}{\tau_0} \right)^2, \quad (19)$$

where  $\lambda_\xi = \tau_0 U_c$ .

Using this estimation, the longitudinal microscale was found to be approximately 12.5% of  $\delta$  for the zero-pressure gradient, 18% of  $\delta$  for the favorable, and 14% of  $\delta$  for the adverse pressure gradient case.

#### LATERAL CROSS-SPECTRAL MEASUREMENTS

The function  $B \left( \frac{\omega \eta}{U_\infty} \right)$  for the zero-pressure gradient is shown in Fig. 38 and the agreement with Bakewell and Willmarth is excellent. Again, as in the case of the function  $A \left( \frac{\omega \xi}{U_\infty} \right)$ , no dependence on the  $\frac{\omega \delta}{U_\infty}$  parameter was found. Departure of the function  $B$  for both the favorable (Fig. 39) and adverse (Fig. 40) pressure gradients from the zero-pressure gradient values is slight. This is in line with White's theoretical work, which shows little difference between pressure gradients for the magnitude of the normalized lateral cross-spectral density. As in the case of the zero-pressure gradient, no dependence on the  $\frac{\omega \delta}{U_\infty}$  parameter was found for either the favorable or adverse pressure gradient. Very little change in the lateral decay process with the moderate pressure gradients used in this experiment is to be expected, as the boundary layers were still two-dimensional and from the previous discussion, the shape of the mean velocity profile rather than the details of the longitudinal and lateral turbulent intensities is the dominant cause in the differences between favorable, zero, and adverse pressure gradients insofar as correlation measurements are concerned.

## CHAPTER 7

### ACCURACY OF THE EXPERIMENTAL MEASUREMENTS

The absolute accuracy of the flow velocity, as derived from probe total pressure - wall static pressure measurements was estimated to be  $\pm 0.55\%$ . As shown by Rayle,<sup>29</sup> the error due to the finite size of the wall static tap (0.028 inches) is 0.3% of the dynamic head, which is about a 0.15% error in velocity determination. The resolution of the draft gauges used was 0.01" of water; this could account for a very small error, about  $\pm 0.15\%$  for  $\pm 0.005$ " of water resolution error in the range of pressures used. Since the error in measuring stagnation pressure with the total pressure probe used was nil, and the error in assuming incompressible flow is 0.15% at a Mach number of 0.1, the estimate of  $\pm 0.55\%$  absolute accuracy for velocity measurements seems reasonable. The calibration of the hot wire was accurate to  $\pm 2\%$ , as discussed by Rakowsky.<sup>16</sup>

For the boundary-layer profiles the location of the probe could be determined to within 0.0001", once the "zero" point or contact with the plate was established. This contact was determined electrically and was repeatable to within  $\pm 0.0005$ ". However, because of the asymptotic behavior of the boundary-layer velocity distribution as it approaches free-stream conditions, the determination of  $\delta$  is more dependent on the precision of the velocity measurement than on the accurate location of the probe. Because of the above reasons, the value of  $\delta$  is estimated to be accurate within the range +2 to -5% and +5 to -15% for the favorable pressure gradient. The other boundary-layer parameters  $\delta^*$  and  $\theta$  are considerably more accurate as they are obtained by integration of the velocity profile. For this reason  $\delta^*$  and  $\theta$  were used as parameters instead of  $\delta$  whenever possible. The inaccuracy due to integration of the profile was found to be +0.36% for  $\delta^*$  and +0.09% for  $\theta$  when compared to results for a 1/7-power velocity distribution. This was well below the experimental measurement accuracy for the input data.



The calibration error of the pressure transducers when compared to the standard transducer was approximately  $\pm 0.5$  db. Accuracy of the standard over the frequency range used was better than  $\pm 0.5$  db. For the frequency spectrum measurements, which includes the amplification system and the spectrum analyzer, the error is estimated to be  $\pm 1.75$  db, with most of this occurring in the analyzer. Hence the measurements of frequency spectrum are believed to be accurate to within  $\pm 1.75$  db and probably closer to  $\pm 1.5$  db.

As indicated in Chapter 6, the maximum value of correlation was repeatable to within  $\pm 3\%$  of 100% correlation for the same reel of magnetic tape run through the correlation computer. The same percentage difference was noted for reels taken at different times with the same signals on them. From this information it was concluded that the maximum amplitudes of the cross-correlations were determinable to within  $\pm 3\%$  of 100% correlation regardless of the maximum amplitude value.

The difference in the time delay to the peak of correlation was as much as  $\pm 10$   $\mu$ sec at time delays of about 200  $\mu$ sec for the same reels of tape processed with the correlation computer. When the same reiterative procedure was used with data having longer time delays to the correlation peak, the differences increased to about  $\pm 20$   $\mu$ sec for delay times up to 1500  $\mu$ sec. To improve accuracy an average of 3 to 4 values of time delay was used in the shorter runs so that the maximum error was cut from  $\pm 5\%$  to less than  $\pm 3\%$ . An error due to pressure transducer misalignment of  $\pm 0.002''$  at the most, results in apparent time delay errors of less than  $\pm 2$   $\mu$ sec for the speeds used. This is smaller than the errors due to head misalignment, tape stretch, flutter, etc. in the tape recorder, which, as indicated previously, amounted to  $\pm 10$   $\mu$ sec for short time delays. To conclude, the accuracy of the determination of time delay to the peak of correlation ( $\tau_{MAX}$ ) or the convection velocity ranged from  $\pm 3\%$  at small transducer spacing to  $\pm 2\%$  at the maximum spacings.

## CHAPTER 8

### CONCLUSIONS

The effects of mild pressure gradients, both adverse and favorable, on the turbulent boundary-layer pressure fluctuations have been examined in detail. Comparison was made to the zero-pressure gradient case, which agreed well with results reported by other investigators, thereby confirming the validity of the measurements presented.

Several important conclusions are:

(a) The most striking differences are the changes in convection velocities due to distortion of the mean velocity profiles, which are caused by the imposed pressure gradients. Convection velocity ratios  $U_c/U_\infty$  were higher in the favorable pressure gradient case and lower in the adverse pressure gradient when compared to zero pressure gradient data. This conclusion is true, when comparisons are made at like non-dimensional frequencies and longitudinal separations.

(b) Convection velocity increases with longitudinal separation and decreases with increasing frequency for the adverse and favorable pressure gradient as well as the zero-pressure gradient.

(c) Loss of coherence or decay of a particular frequency component in the longitudinal direction was more rapid in the adverse than in the zero pressure gradient. Conversely, a slower rate of decay in the favorable pressure gradient was measured.

(d) No significant differences in the lateral decay of a particular frequency component due to the favorable or adverse pressure gradient were observed.

(e) Root-mean-square pressure fluctuation levels for broad frequency bands are greater in the adverse pressure gradient and less in the favorable pressure gradient when compared to zero-pressure gradient levels. This difference is further emphasized when comparison is made on the basis of wall shear stress rather than free-stream dynamic pressure.

(f) The spectral density is altered in such a manner as to reflect the changes in longitudinal turbulent intensity with distance from the wall due to the imposed pressure distributions. When non-dimensionalized against  $\delta^*$ , the adverse pressure gradient spectrum is higher at lower non-dimensional frequencies than the zero-pressure gradient spectrum. At higher non-dimensional frequencies the two are almost identical.

For the favorable pressure gradient spectrum the pressure fluctuation level is slightly higher than in the zero-pressure gradient spectrum at  $\frac{f \delta^*}{U_\infty} = 0.03$  but then falls off at lower values of  $\frac{f \delta^*}{U_\infty}$ . As inferred by the longitudinal turbulent intensity profile, the spectral curve drops off quite sharply at the higher non-dimensional frequencies.

(g) Comparison of zero-pressure gradient spectral densities with data of other investigators indicates that using  $\phi(f)/\rho^2 \delta^* U_\infty^3$  as a parameter rather than  $\phi(f) U_\infty / \delta^* \tau_w^2$  or  $\phi(f)/\rho^2 \delta U_\infty^3$  reduces the differences in spectra between them.

(h) The qualitative agreement with White's predictions (Ref. 13 and 15) for the adverse and favorable pressure gradients for lateral and longitudinal cross-spectral densities is as good as that indicated for the zero-pressure gradient as depicted in Figs. 5 and 6 of Ref. 13. Specifically, the experimentally determined functions B and A are always lower by 5 to 25% of 100% correlation.

In the zero-pressure gradient the measurements of convection velocity ratios are always lower than White's predictions by 10 or 15%. For the favorable pressure gradients the measured values of convection velocity ratios are higher than theoretical predictions by 0 to 10%. Convection velocity ratios in the adverse pressure gradients exceed White's predictions by 5 to 15%. In all three pressure gradients the theoretical predictions followed the general trends of the experimental measurements with regard to the effects of longitudinal separation and frequency on convection velocity ratios.

## APPENDIX A

The corrections used in accounting for the finite size of the pressure transducer in the zero, adverse, and favorable pressure gradients are those computed by Corcos for the zero-pressure gradient. His correction is

$$\frac{\Phi_M(\omega)}{\Phi(\omega)} = \int_{\omega} \phi(\tilde{r}) A\left(\frac{\omega \epsilon_x}{U_c}\right) B\left(\frac{\omega \epsilon_y}{U_c}\right) e^{-\frac{\omega \epsilon_x}{U_c}} dA(\tilde{r}), \quad (1-A)$$

where  $\epsilon_x$  and  $\epsilon_y$  are the components of the vector  $\tilde{r}$ , where  $\phi(\tilde{r})$  depends on the physical characteristics of the pressure transducer only. The effect of the different functions  $A\left(\frac{\omega \epsilon_x}{U_c}\right)$  on the ratio  $\Phi_M(\omega)$  (measured spectral density) and  $\Phi(\omega)$  (actual spectral density) were investigated by approximating these functions with an exponential decay, i. e.,  $A\left(\frac{\omega \epsilon_x}{U_c}\right) \sim e^{-c\left(\frac{\omega \epsilon_x}{U_c}\right)}$  where the constant  $c$  took on a different numerical value for each pressure gradient. The calculations showed a difference of less than 1 db between all three pressure gradients when the correction  $\frac{\Phi_M(\omega)}{\Phi(\omega)}$  was 17 db for the zero pressure gradient case. The difference in  $\frac{\Phi_M(\omega)}{\Phi(\omega)}$  between pressure gradients decreased with a decrease in the correction factor for the zero pressure gradient case. Hence, within the experimental accuracy of the data and the simplifying assumptions which were used by Corcos in developing Eq. (1-A), the use of this equation in all three pressure gradients is justified.

FIGURES 1 THROUGH 40

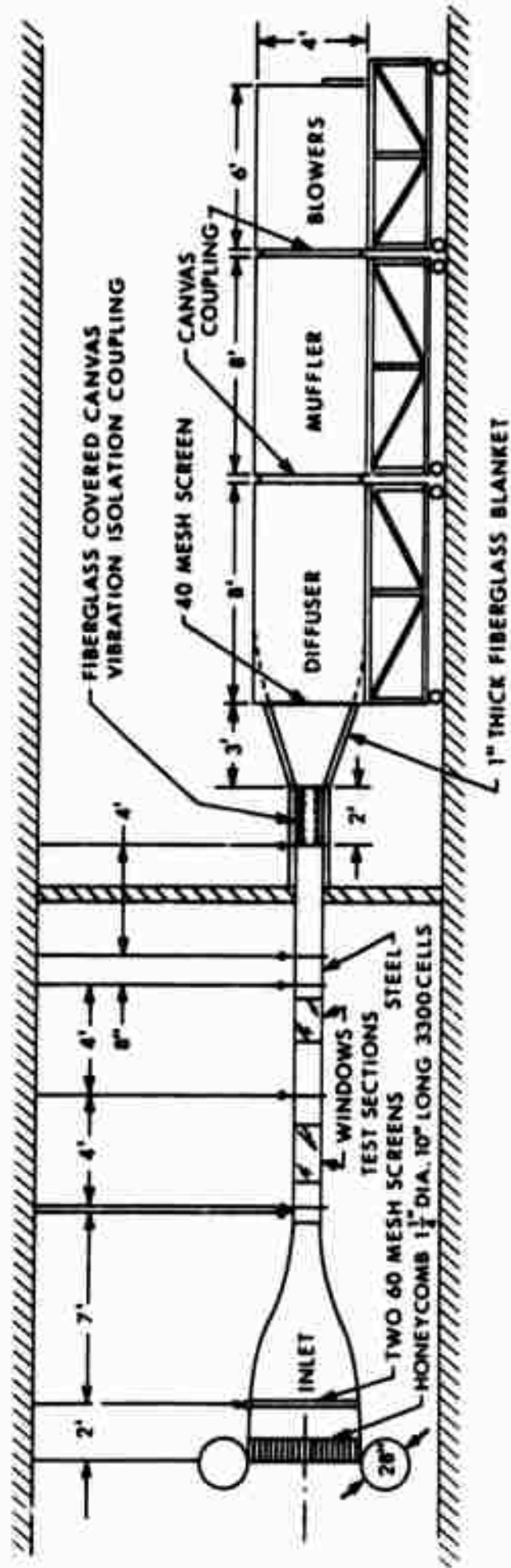


Figure 1. Schematic of Subsonic Wind Tunnel

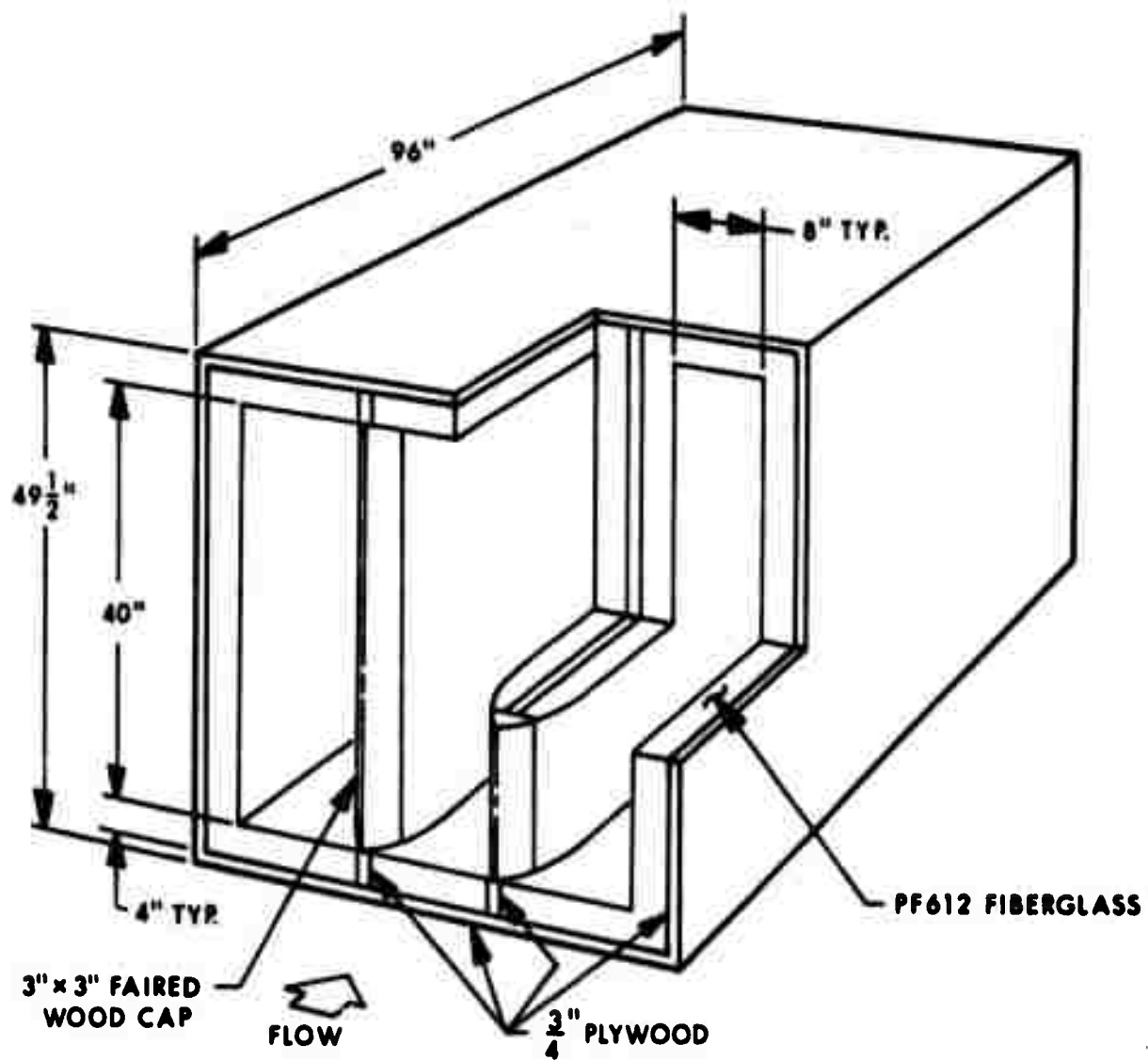


Figure 2. Muffler Details

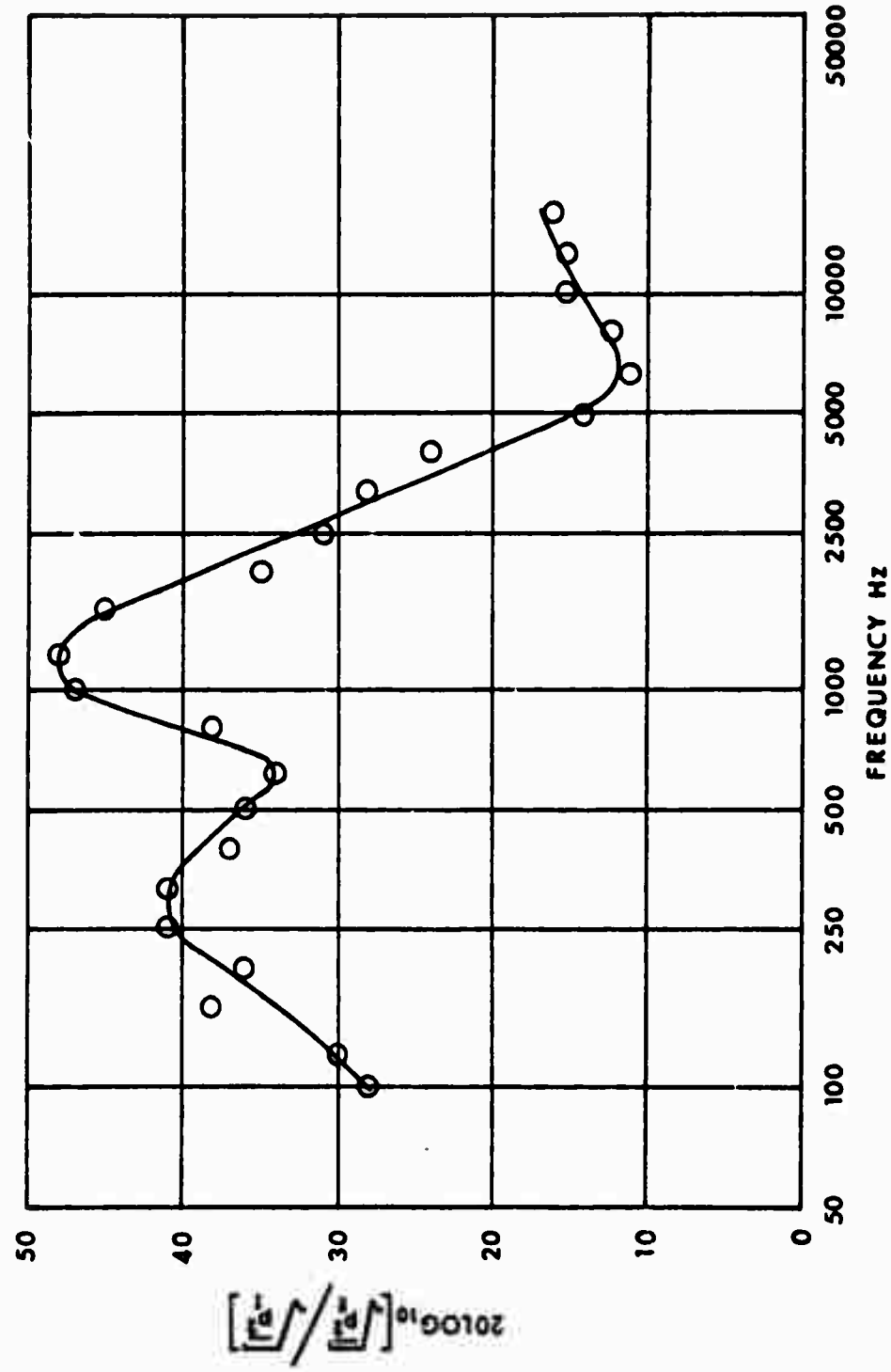
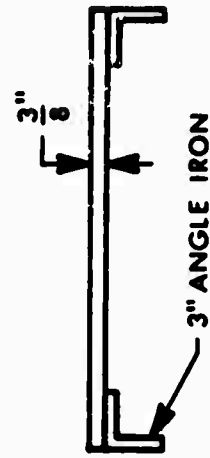
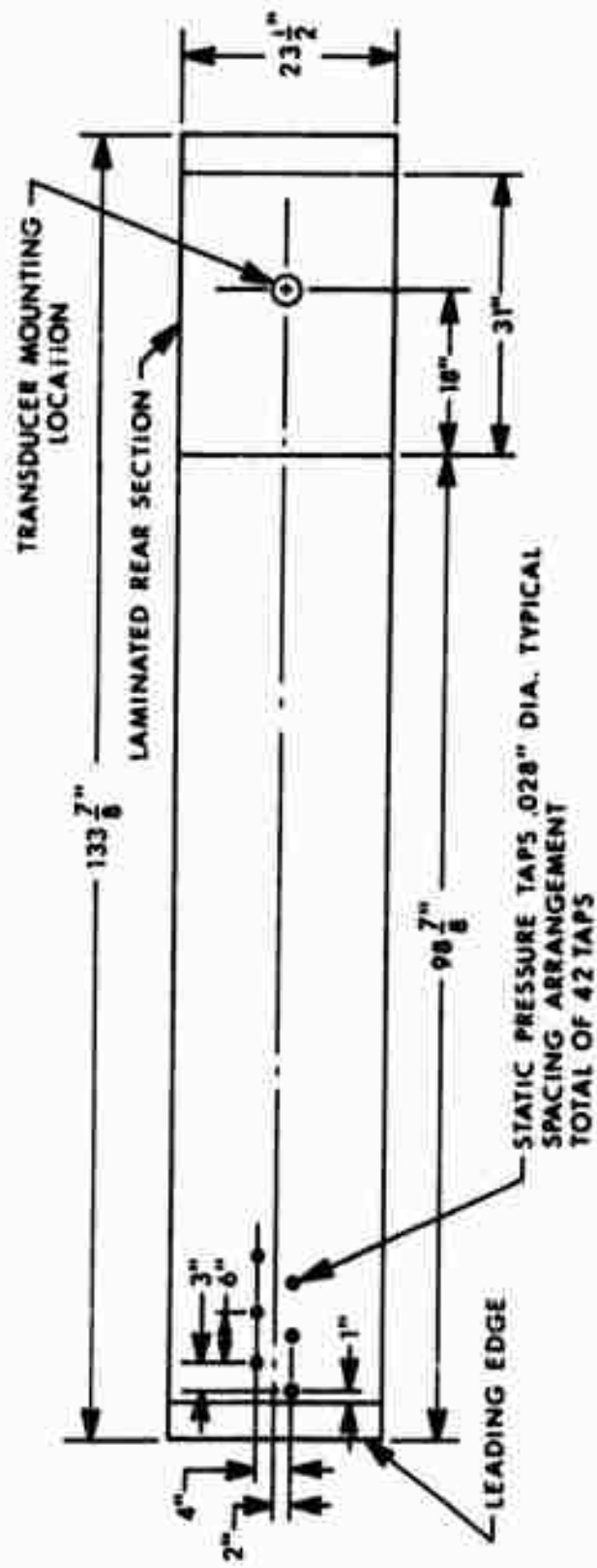
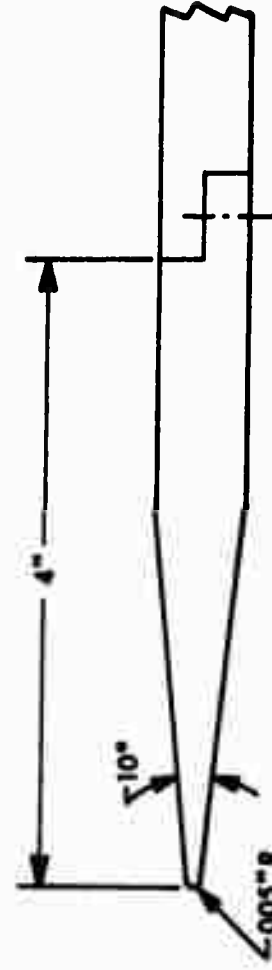


Figure 3. Muffler and Diffuser Attenuation as a Function of Frequency





ANGLE IRON  
MOUNTING DETAIL



LEADING EDGE DETAIL

Figure 4. Flat Plate and Leading Edge Details

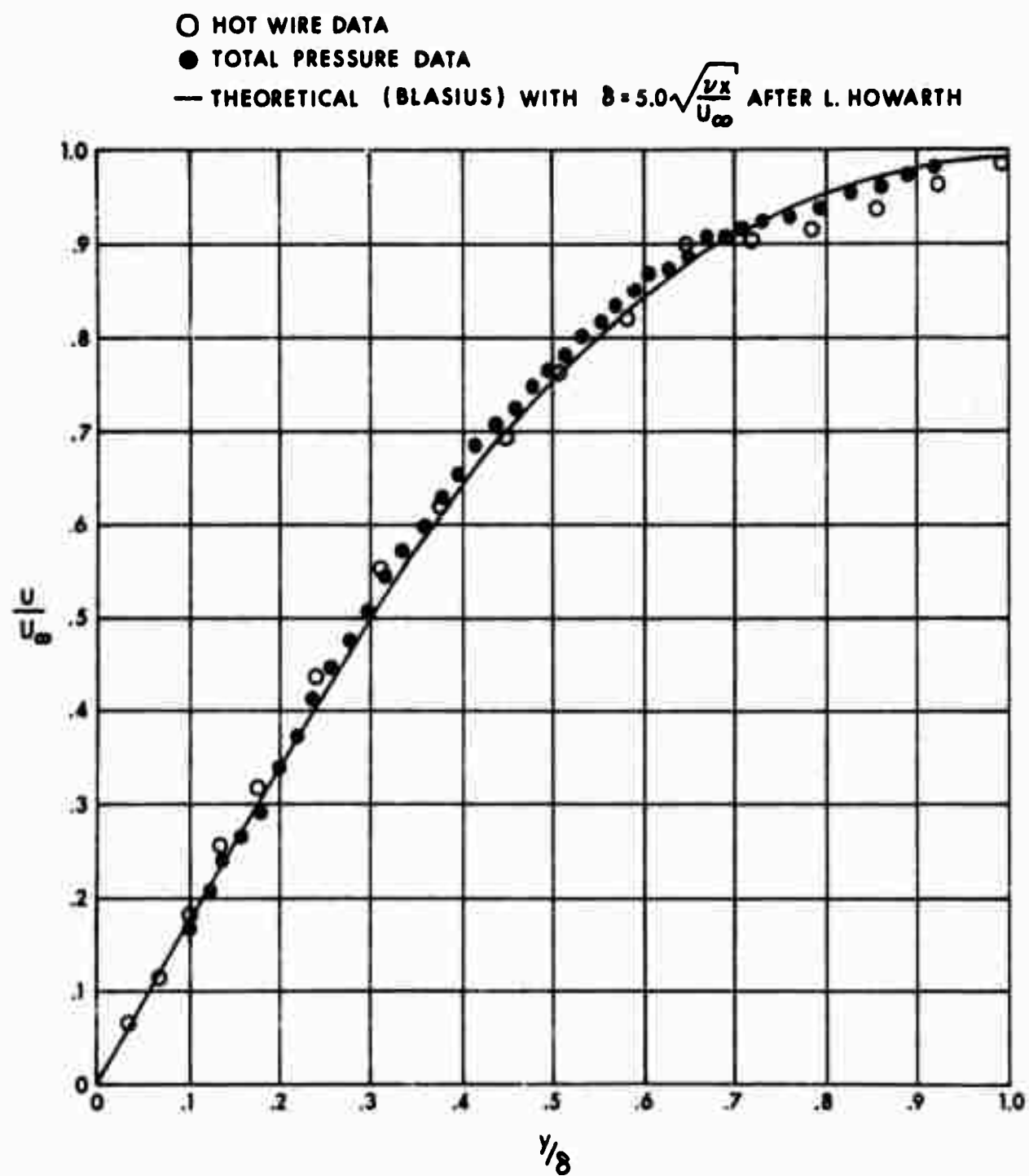


Figure 5. Comparison of Experimental Laminar Velocity Profile to Blasius Profile

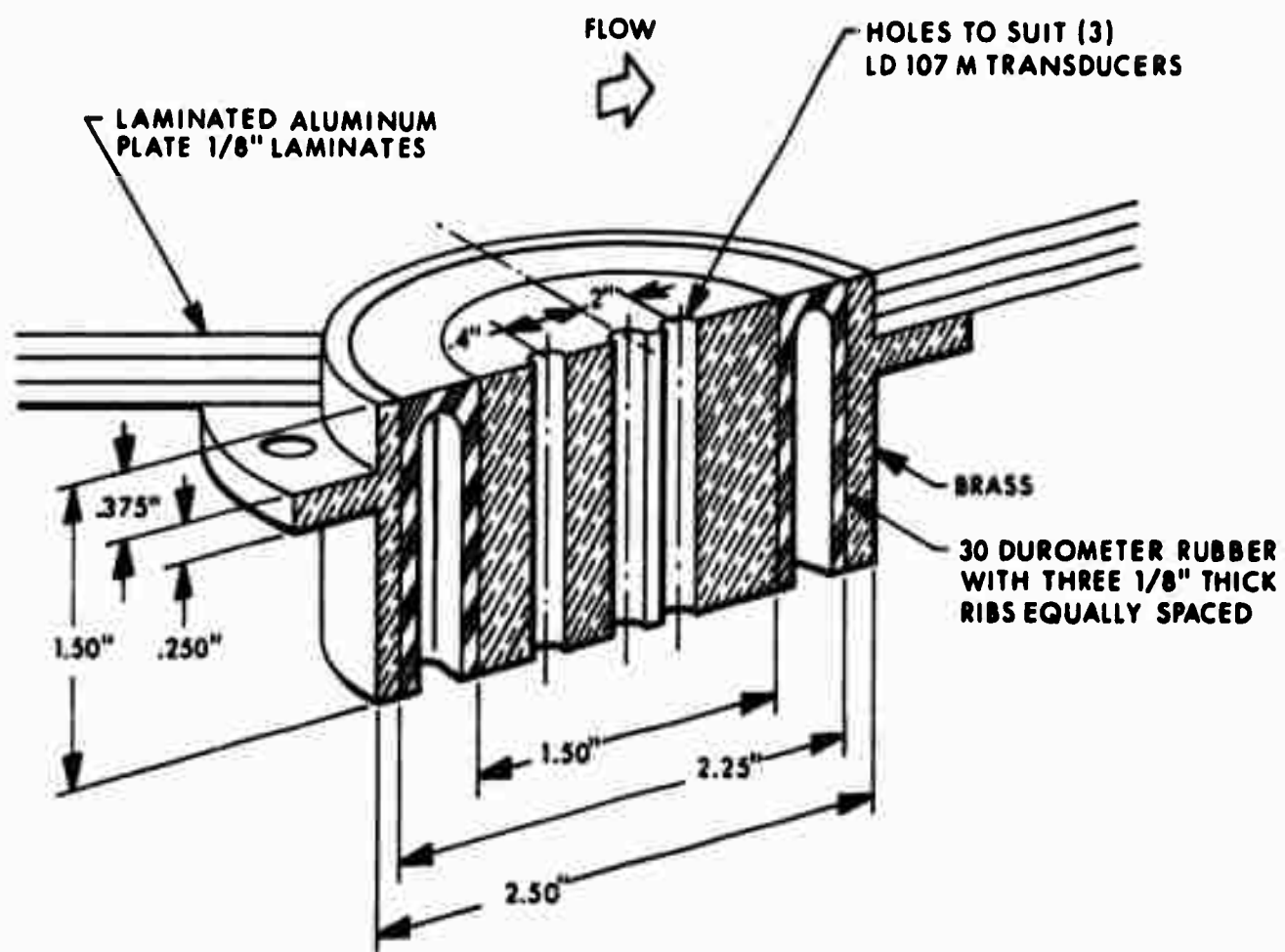


Figure 6. Transducer Mounting Details

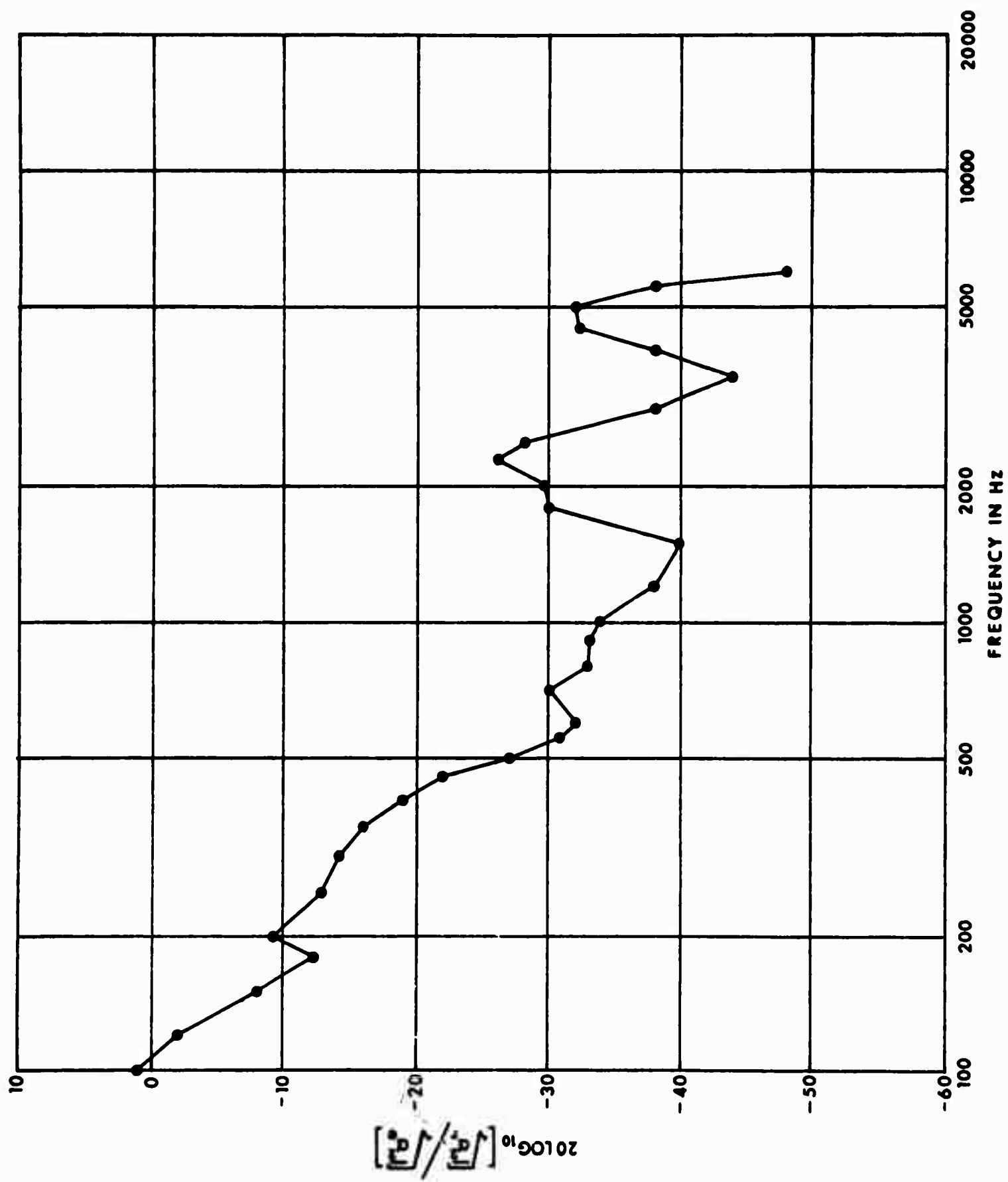
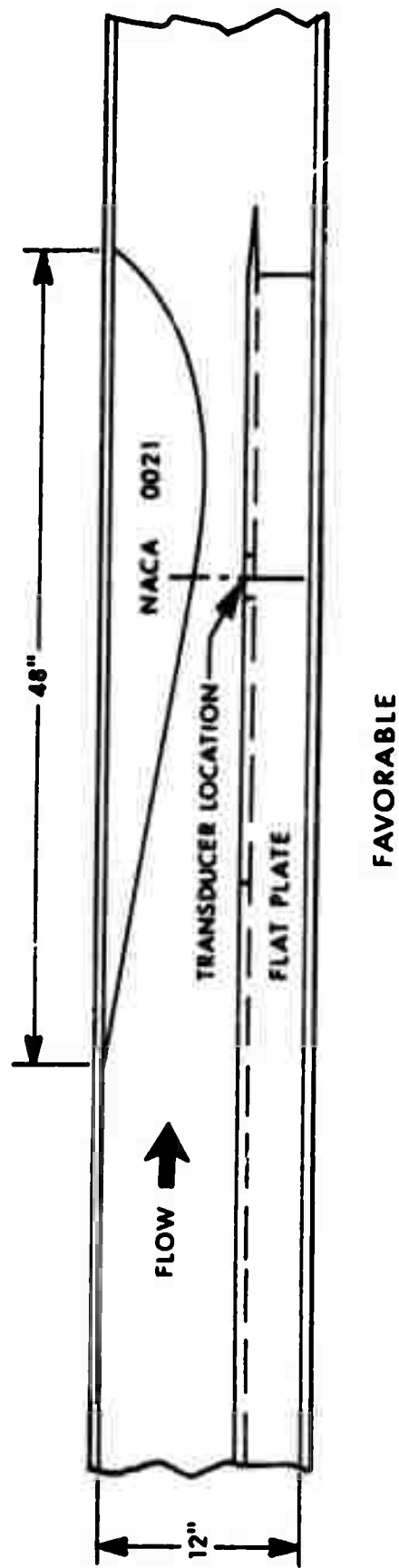
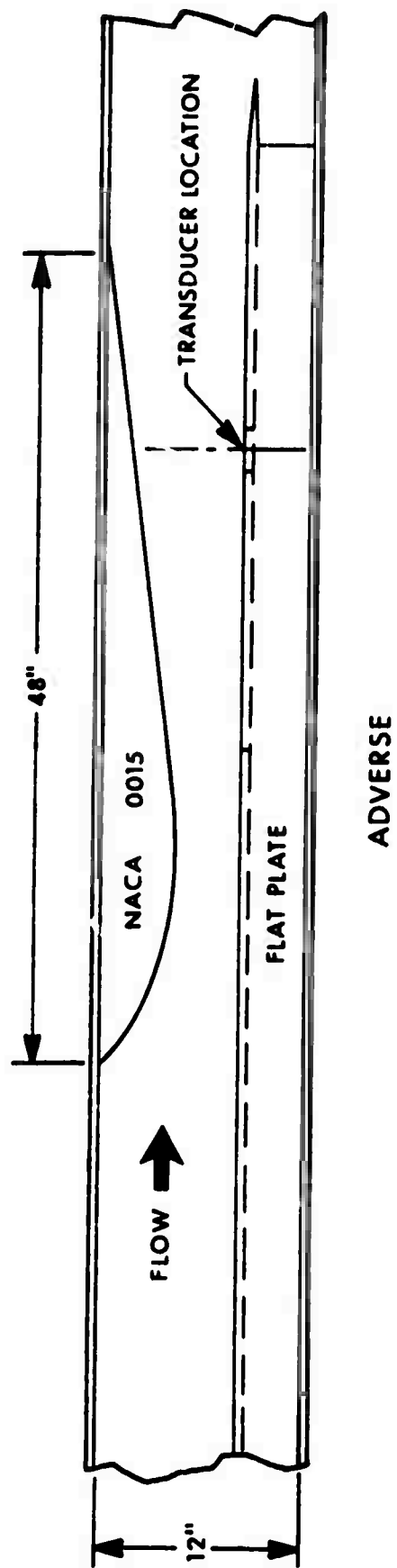


Figure 7. Vibration Isolation of Transducer Mount from Aluminum Plate



### MAXIMUM AIRFOIL THICKNESS AT 30% CHORD

Figure 8. Schematic of Airfoil Sections Used in Obtaining Pressure Gradients

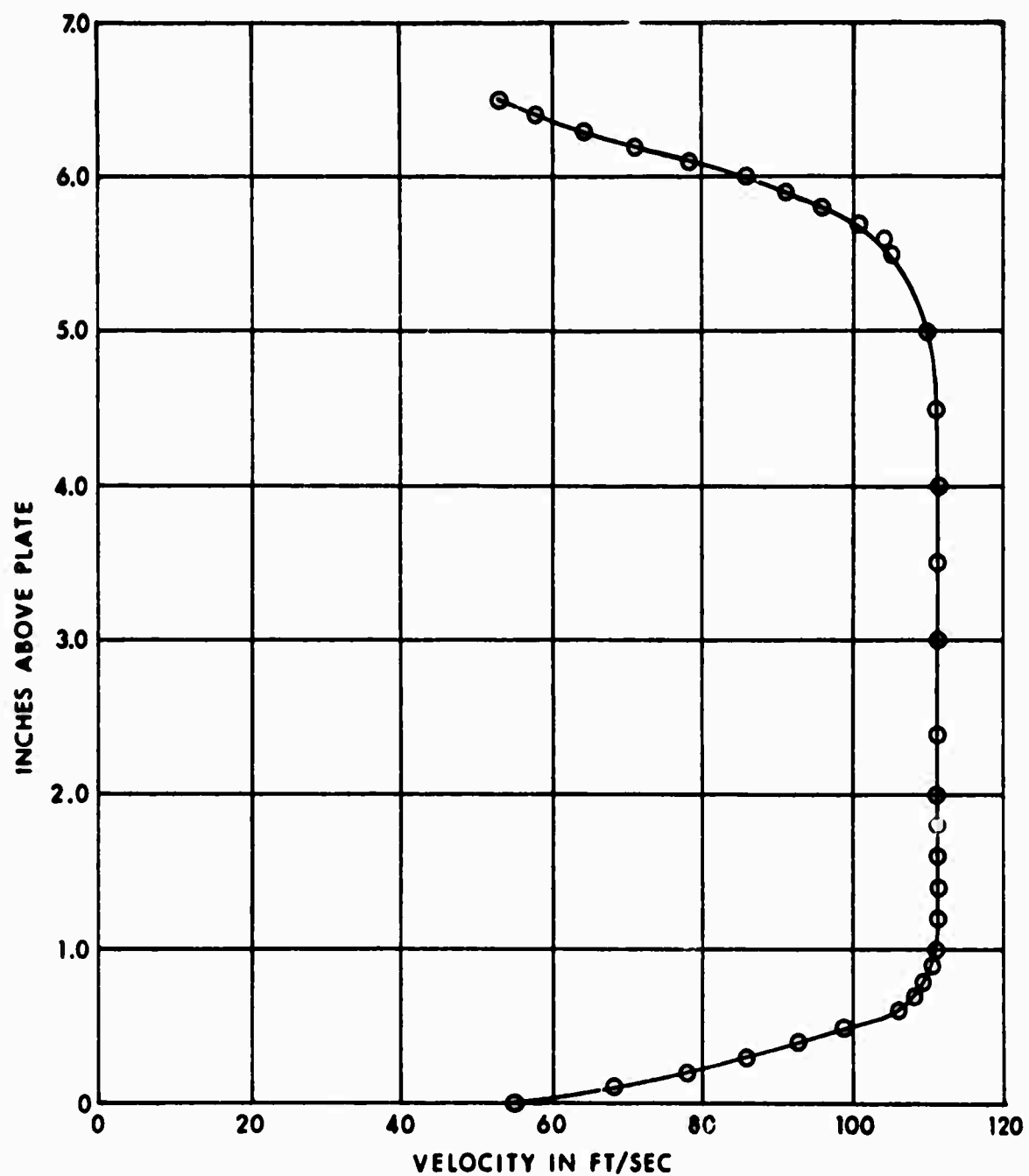


Figure 9. Typical Vertical Velocity Profile Upstream of Transducer Location ( $U_{\infty} = 105$  ft/sec at Transducer Location) Adverse Pressure Gradient

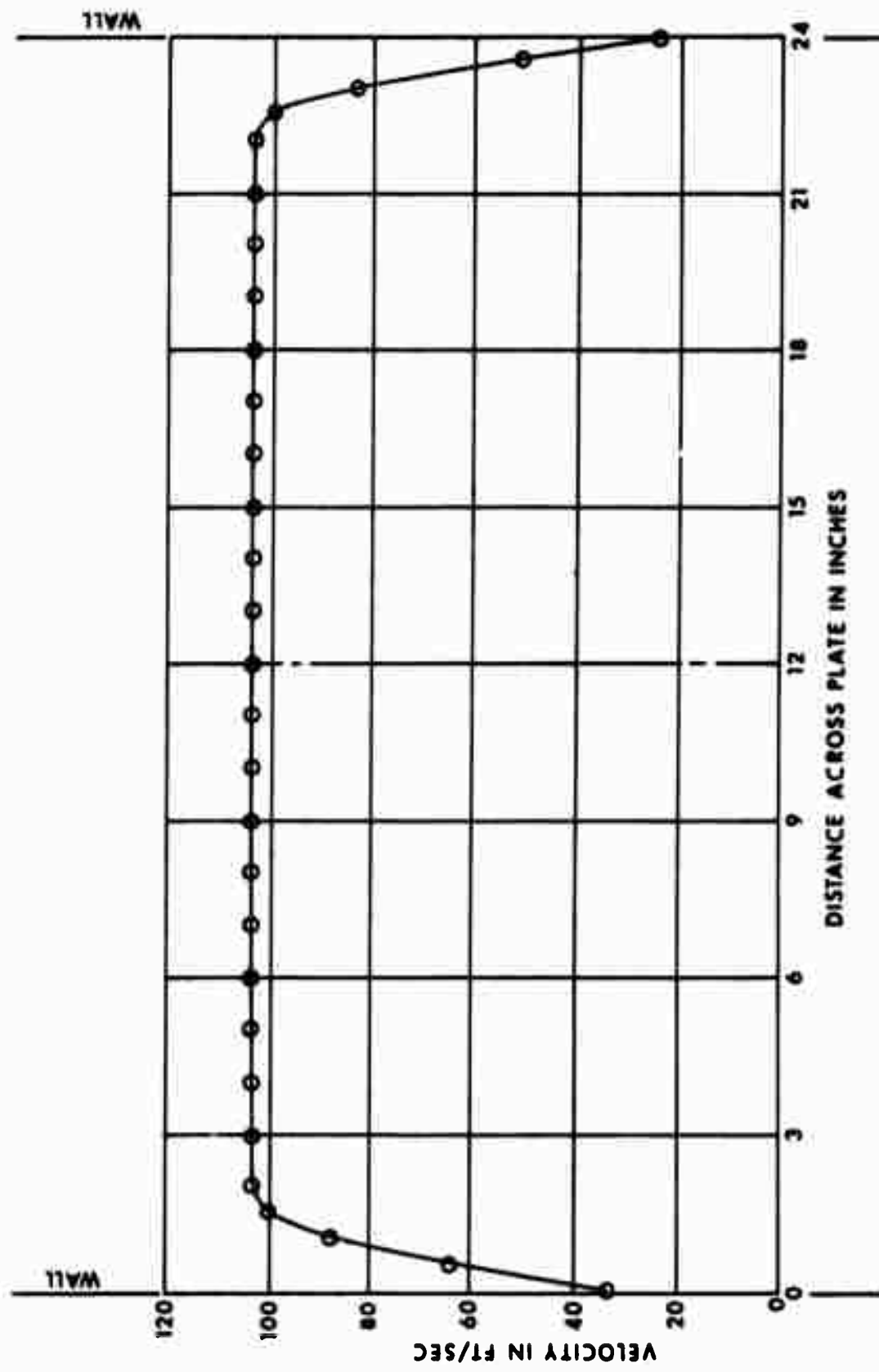


Figure 10. Typical Horizontal Velocity Profile ( $U_{\infty} = 105$  ft/sec at Transducer Location)  
Adverse Pressure Gradient

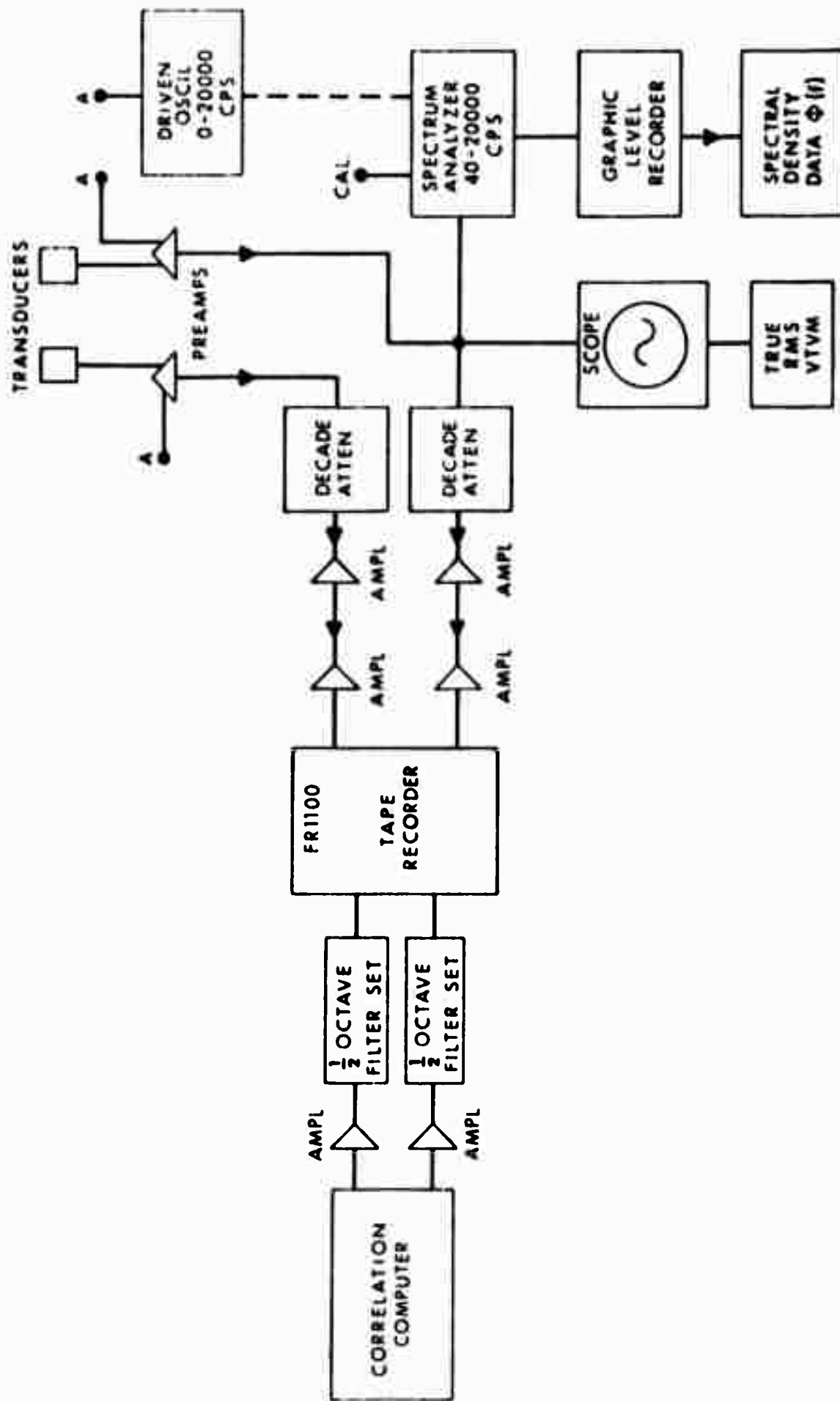


Figure 11. Block Diagram of Instrumentation System



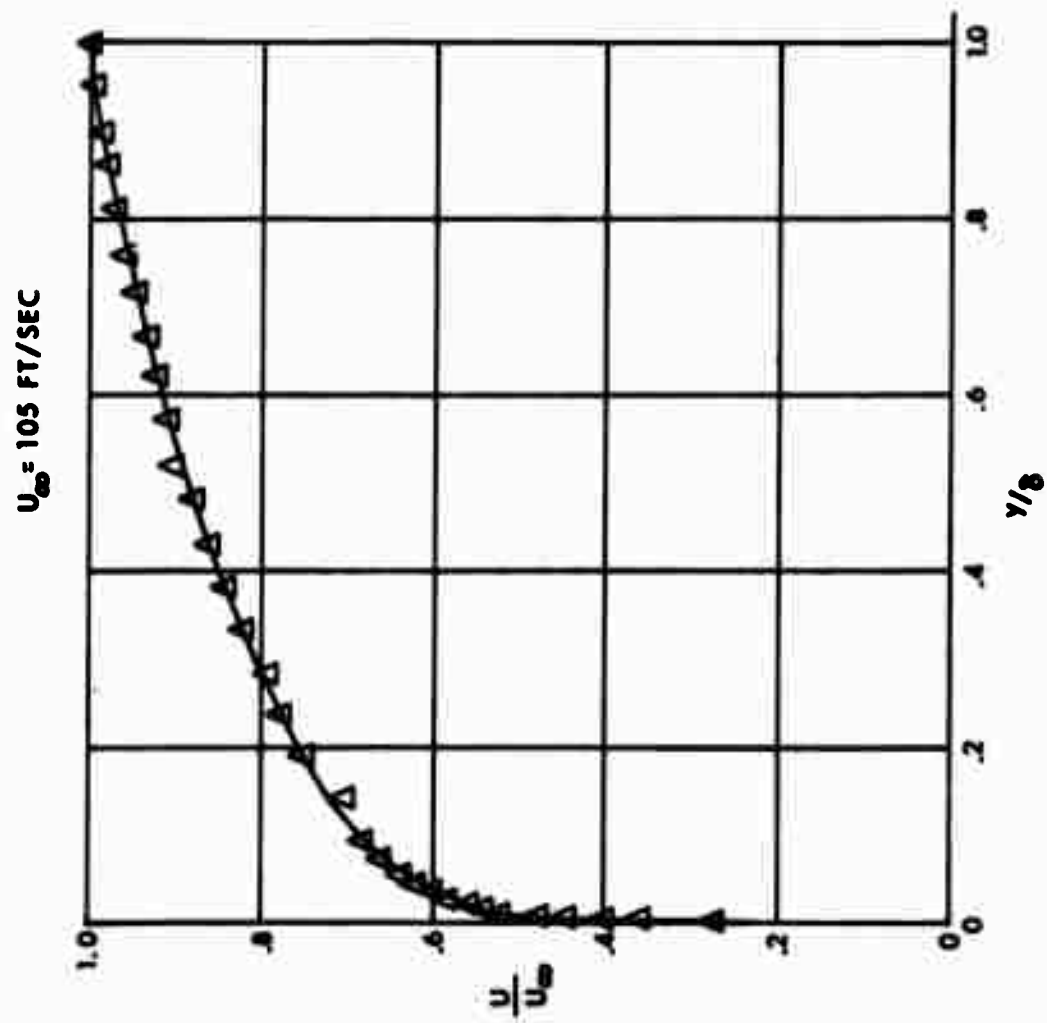


Figure 12. Typical Non-Dimensional Velocity Profile for the Zero Pressure Gradient

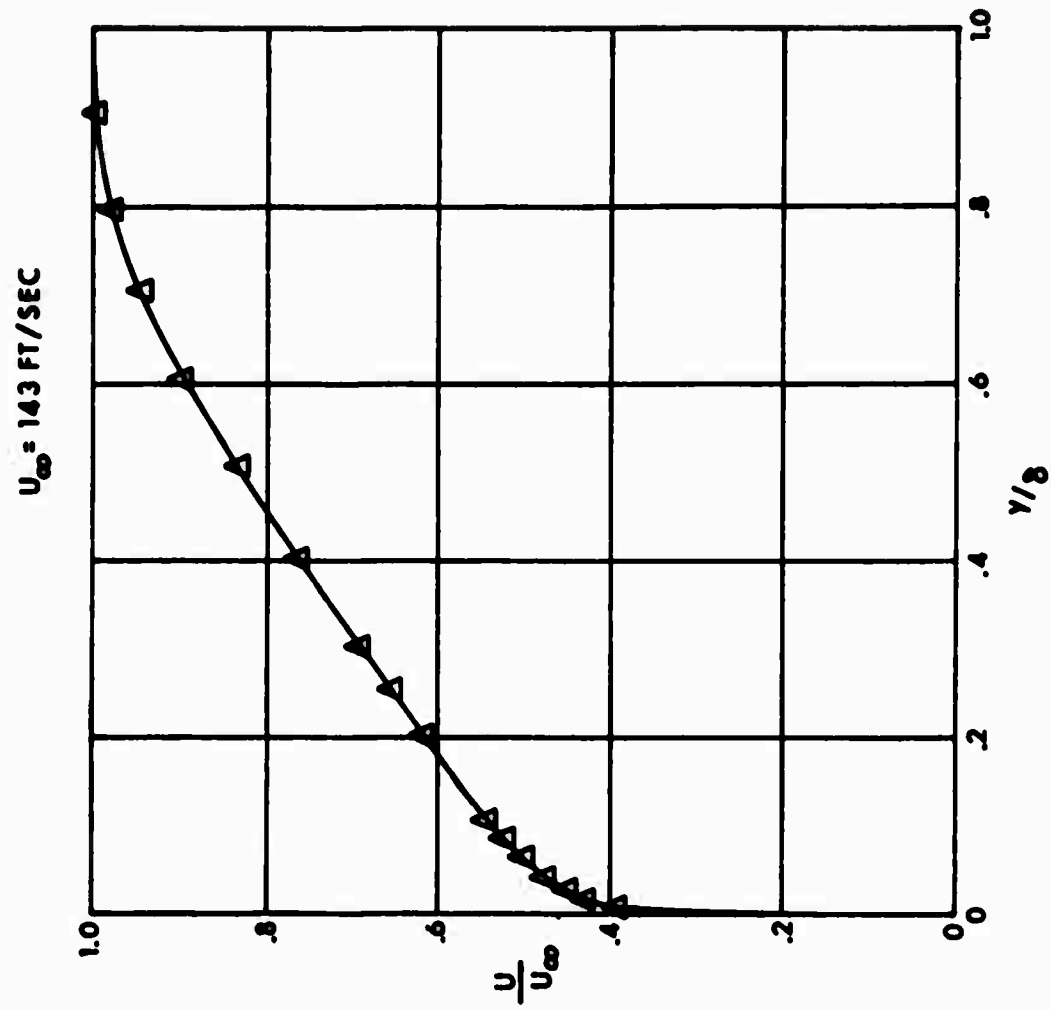


Figure 13. Typical Non-Dimensional Velocity Profile for the Adverse Pressure Gradient

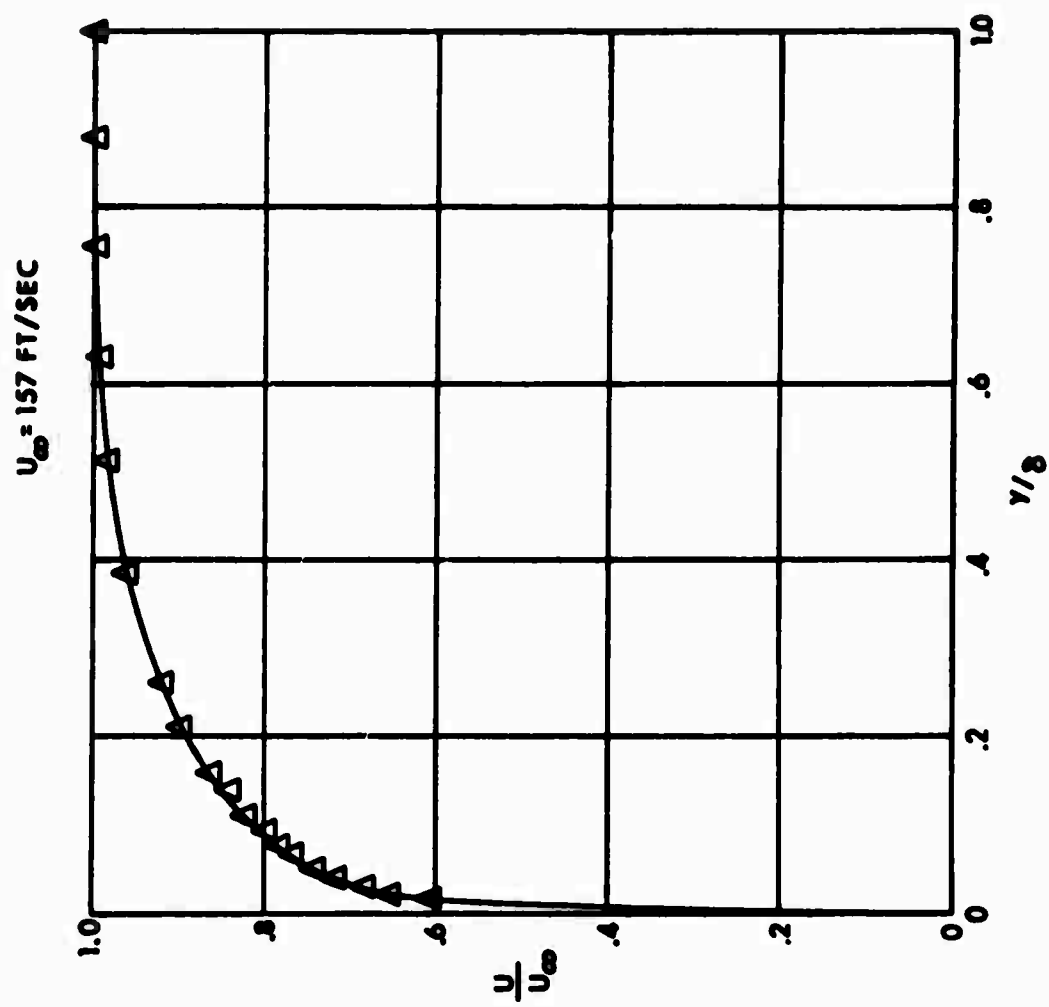


Figure 14. Typical Non-Dimensional Velocity Profile for the Favorable Pressure Gradient

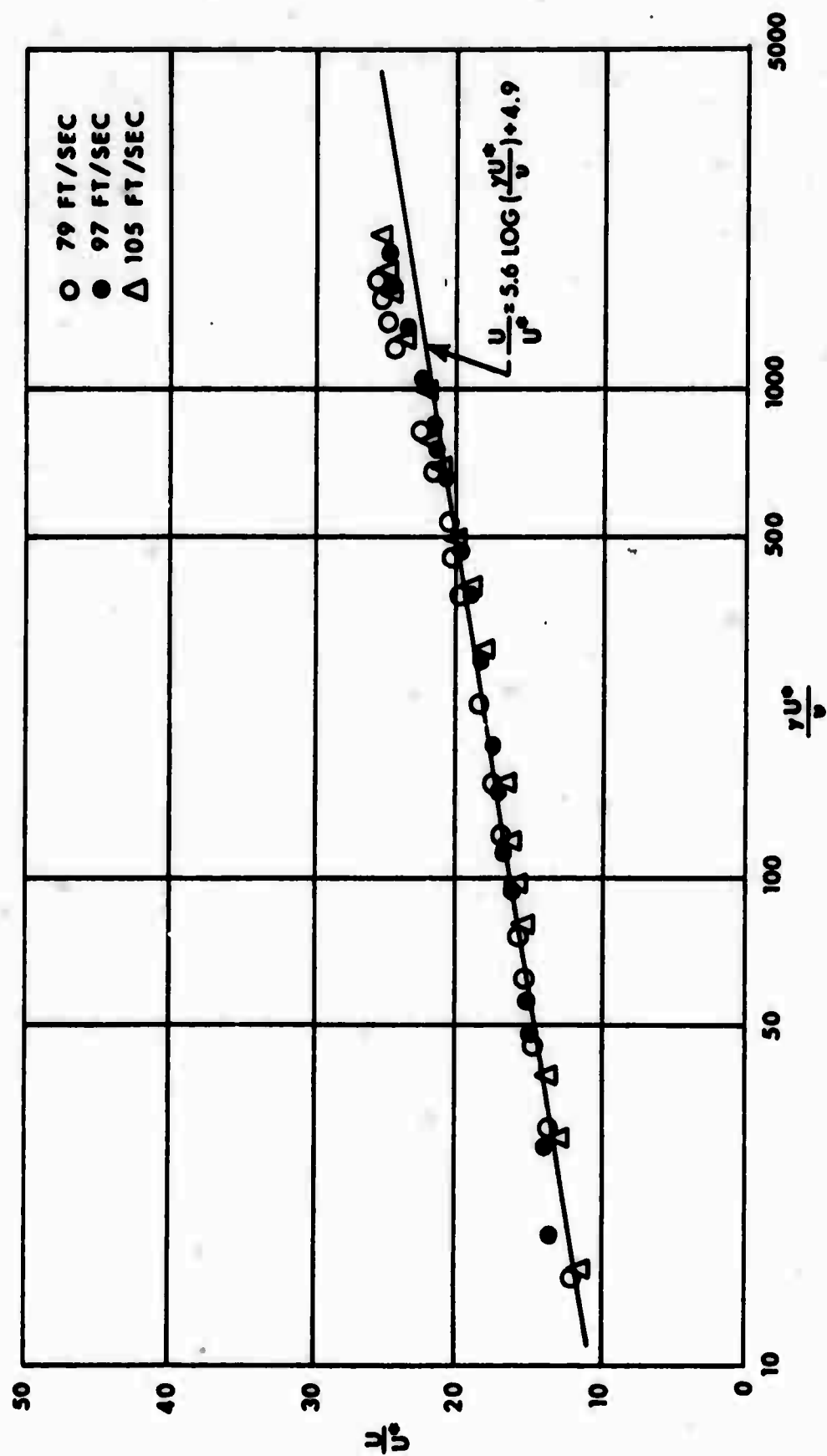


Figure 15. Universal Mean Velocity Profile for the Zero Pressure Gradient

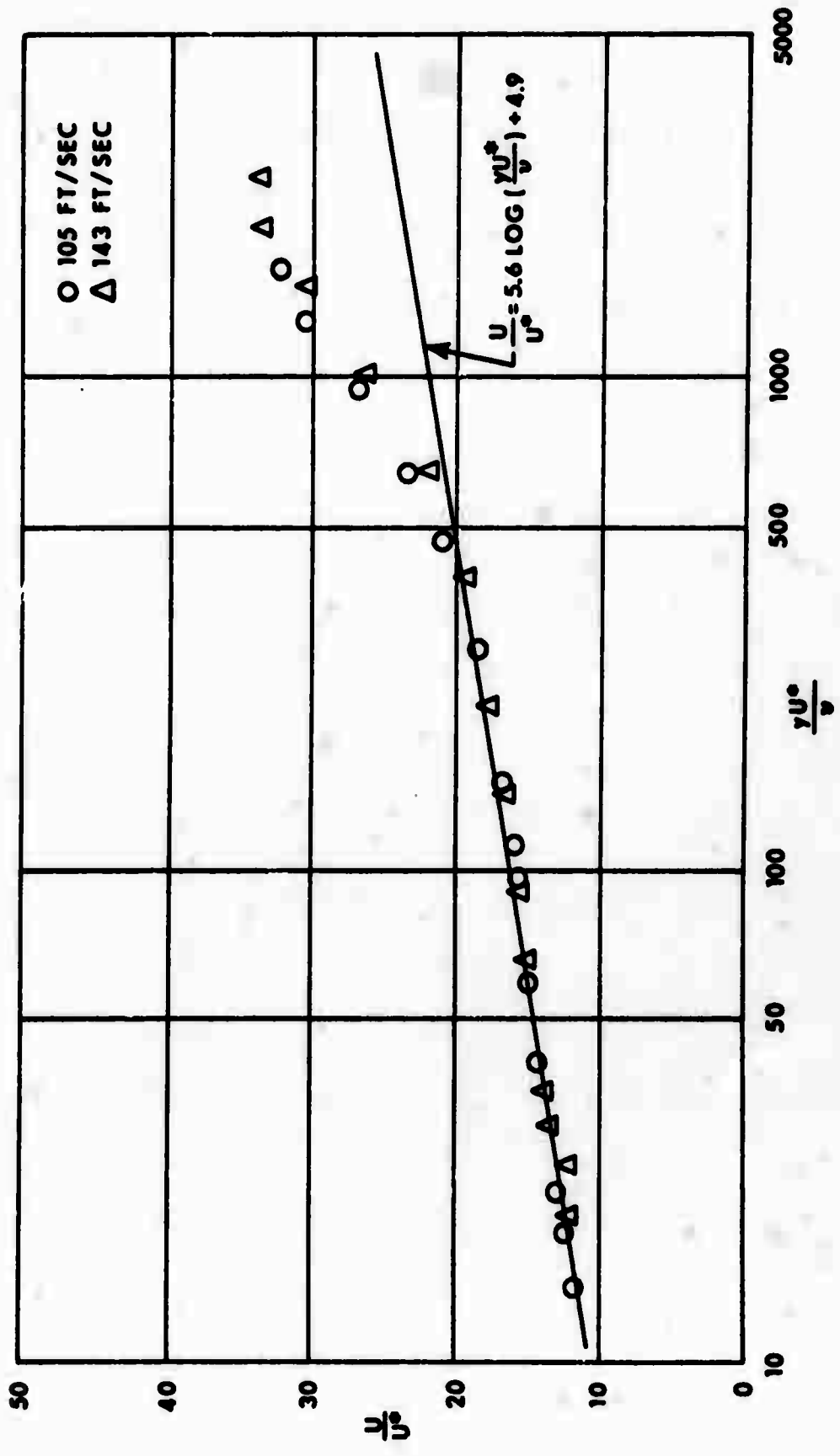


Figure 16. Universal Mean Velocity Profile for the Adverse Pressure Gradient

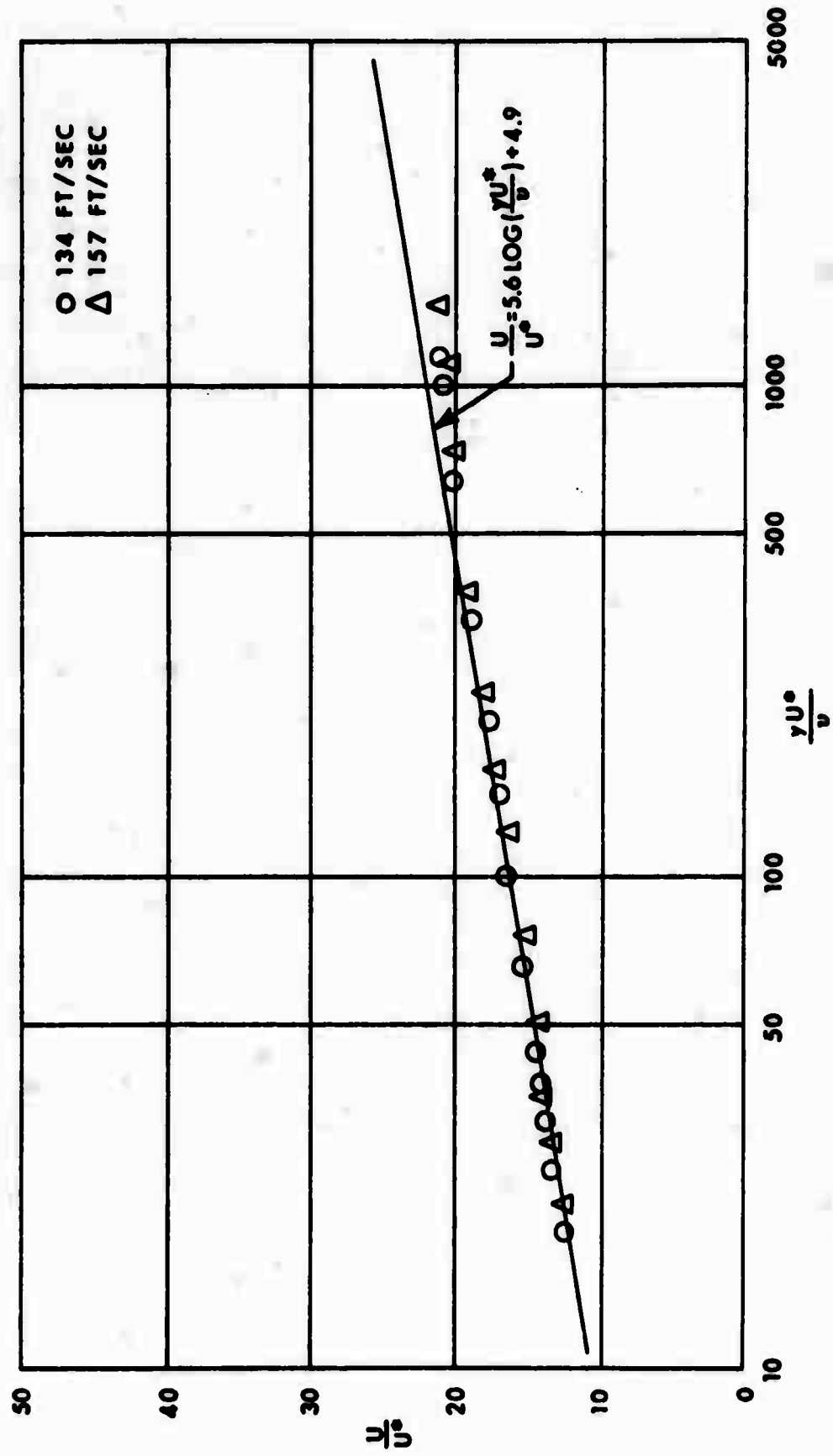


Figure 17. Universal Mean Velocity Profile for the Favorable Pressure Gradient

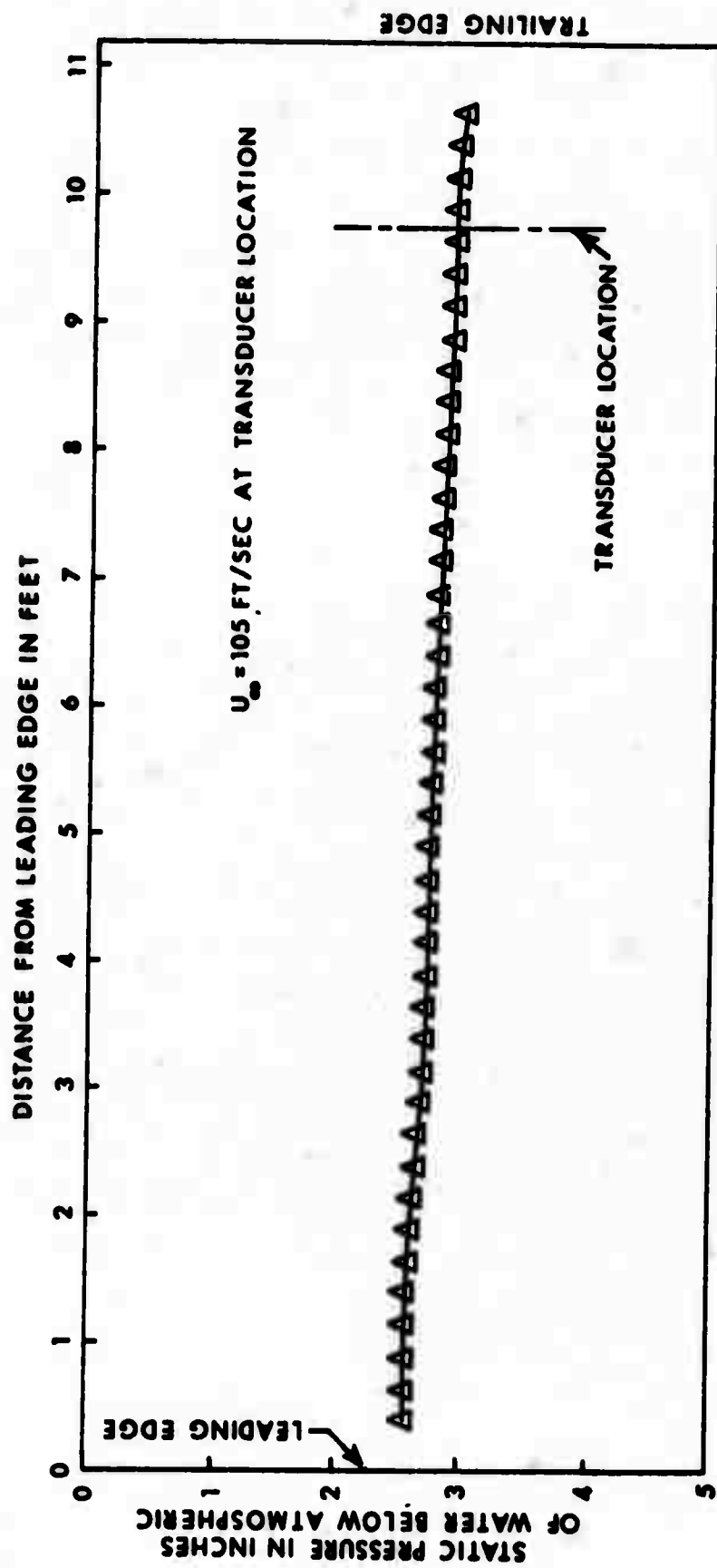


Figure 18. Typical Static Pressure Distribution for the Zero Pressure Gradient

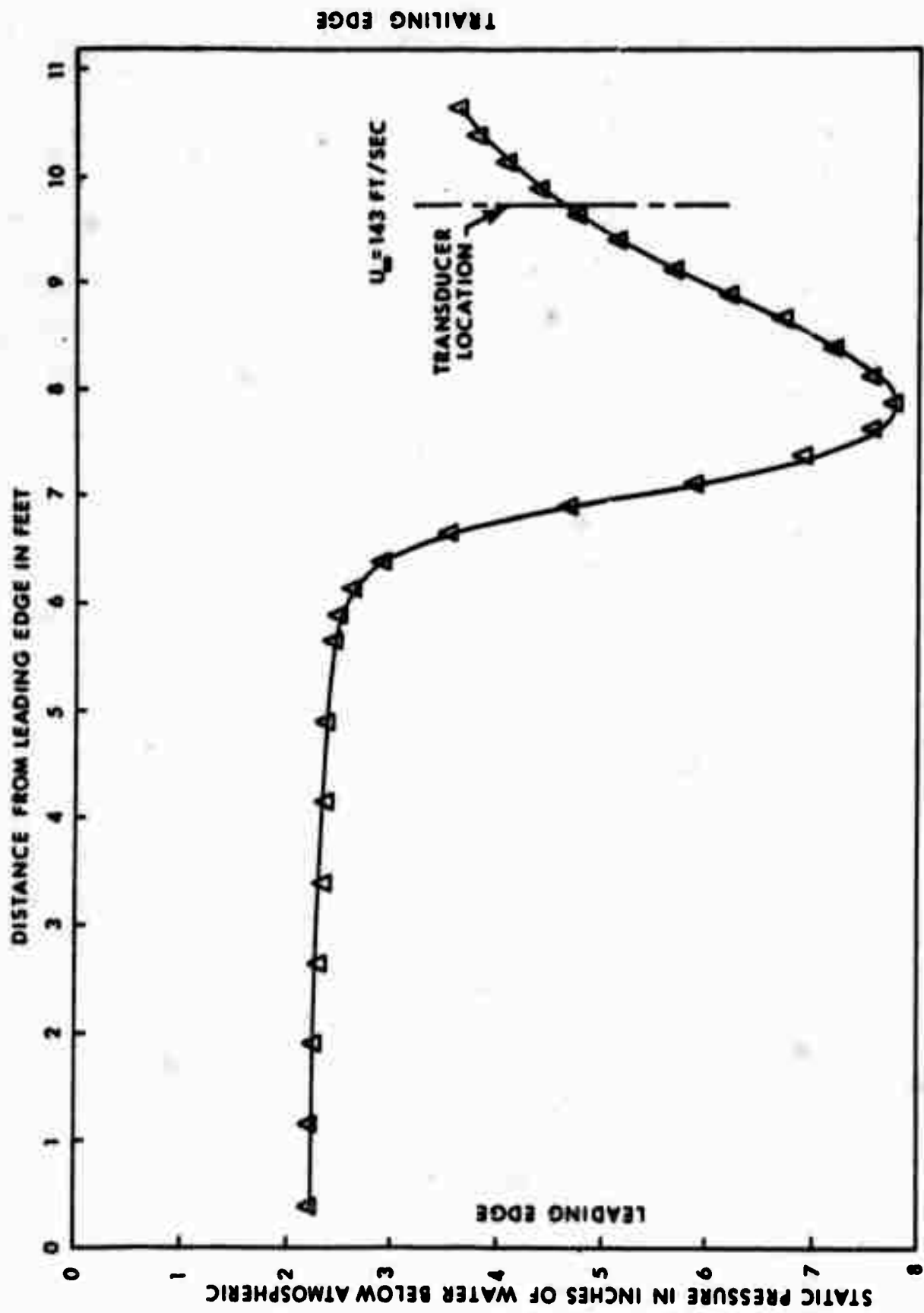


Figure 19. Typical Static Pressure Distribution for the Adverse Pressure Gradient



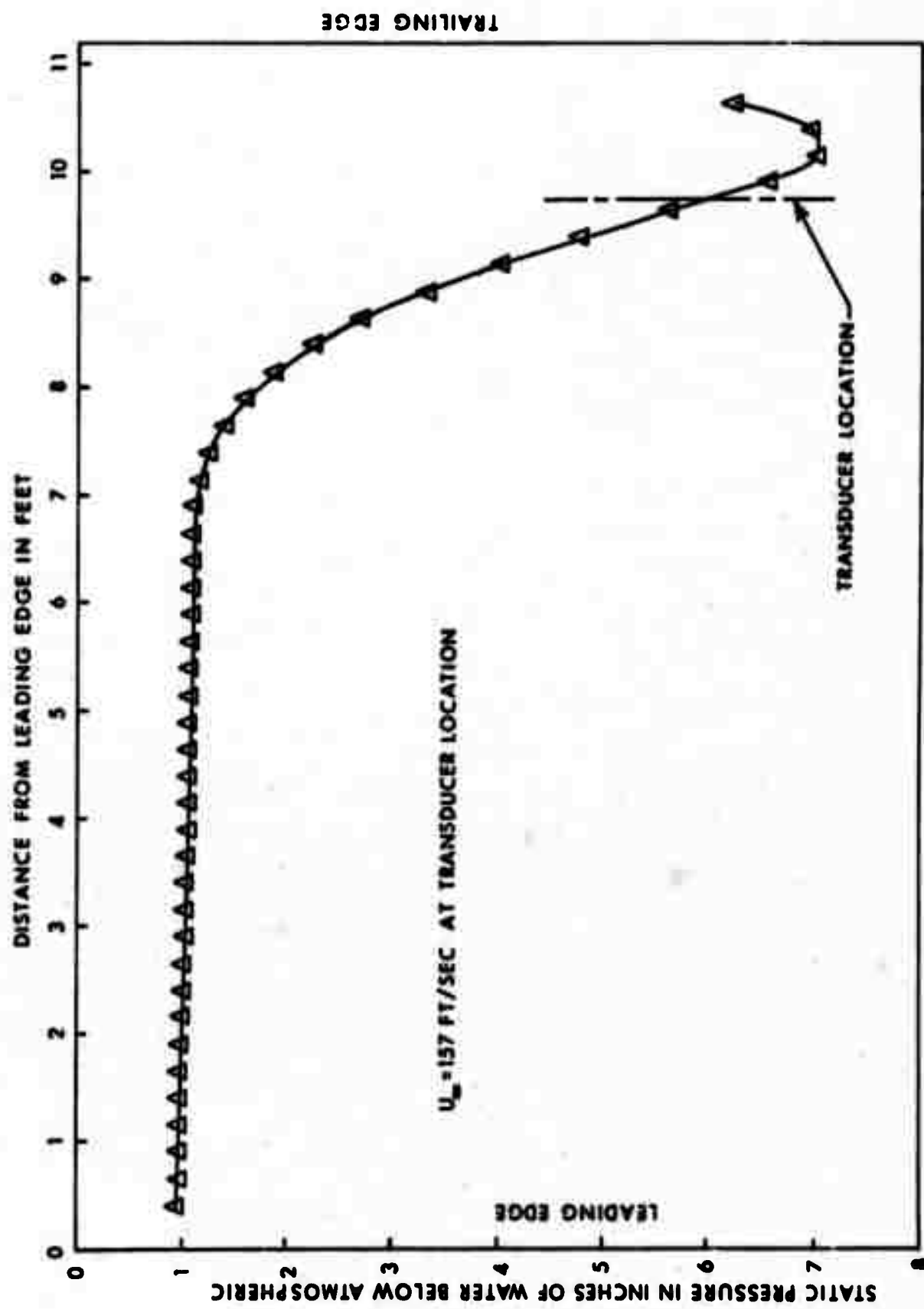


Figure 20. Typical Static Pressure Distribution for the Favorable Pressure Gradient

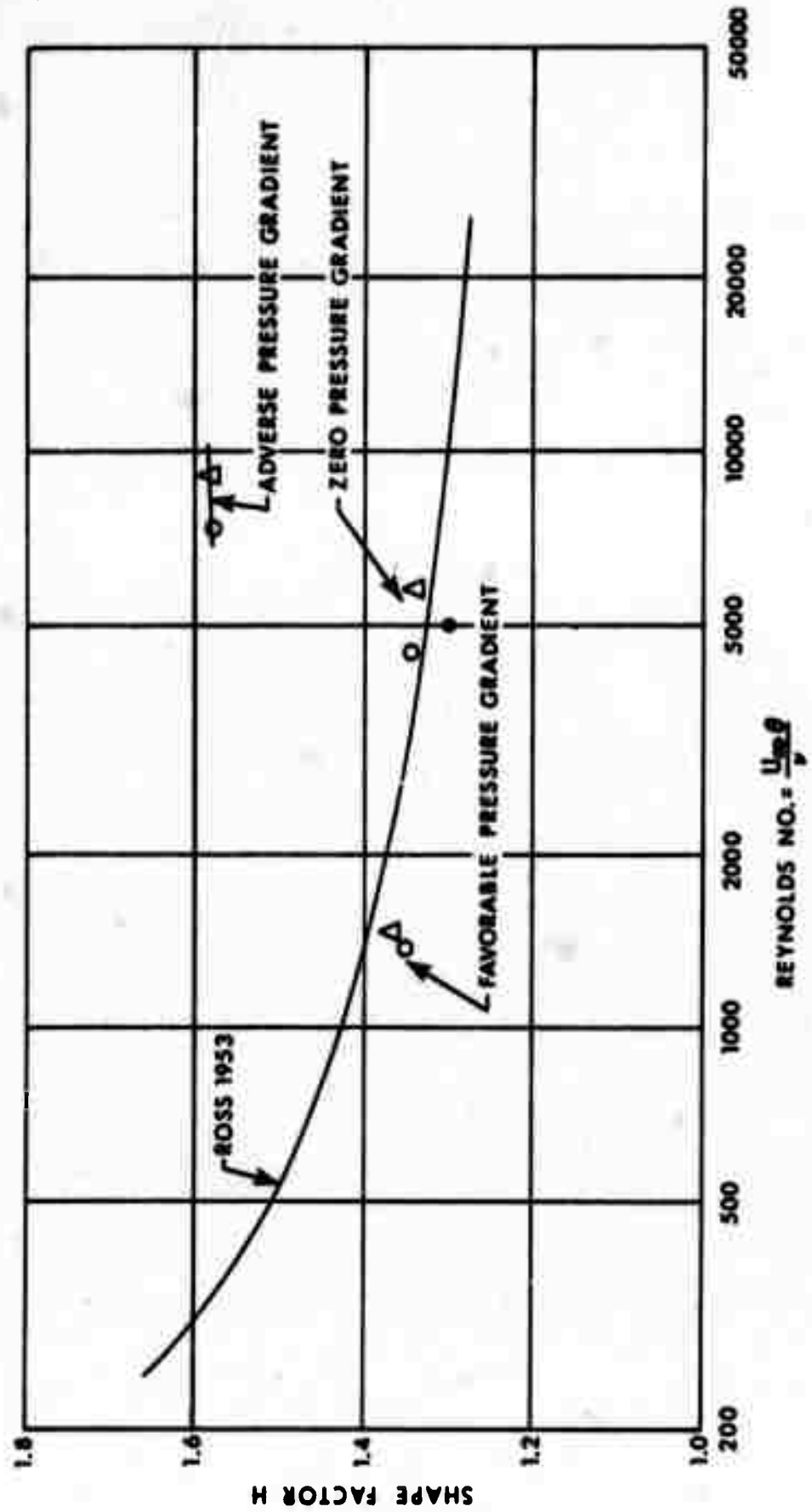


Figure 21. Shape Factor as a Function of Reynolds Number

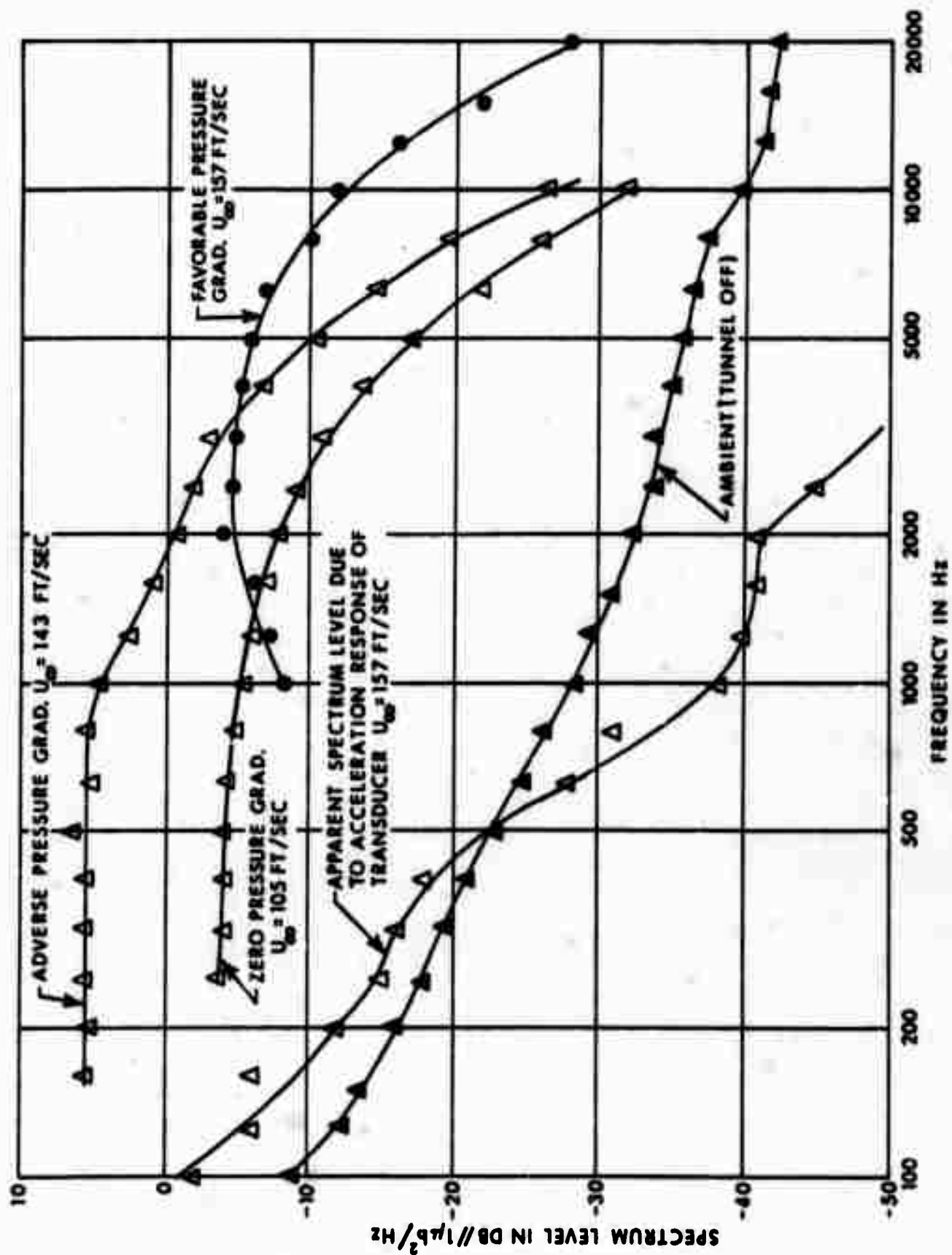


Figure 22. Comparison of Spectrum Levels for Each Pressure Gradient to Ambient and Apparent Spectrum Levels due to Acceleration Response of Pressure Transducer

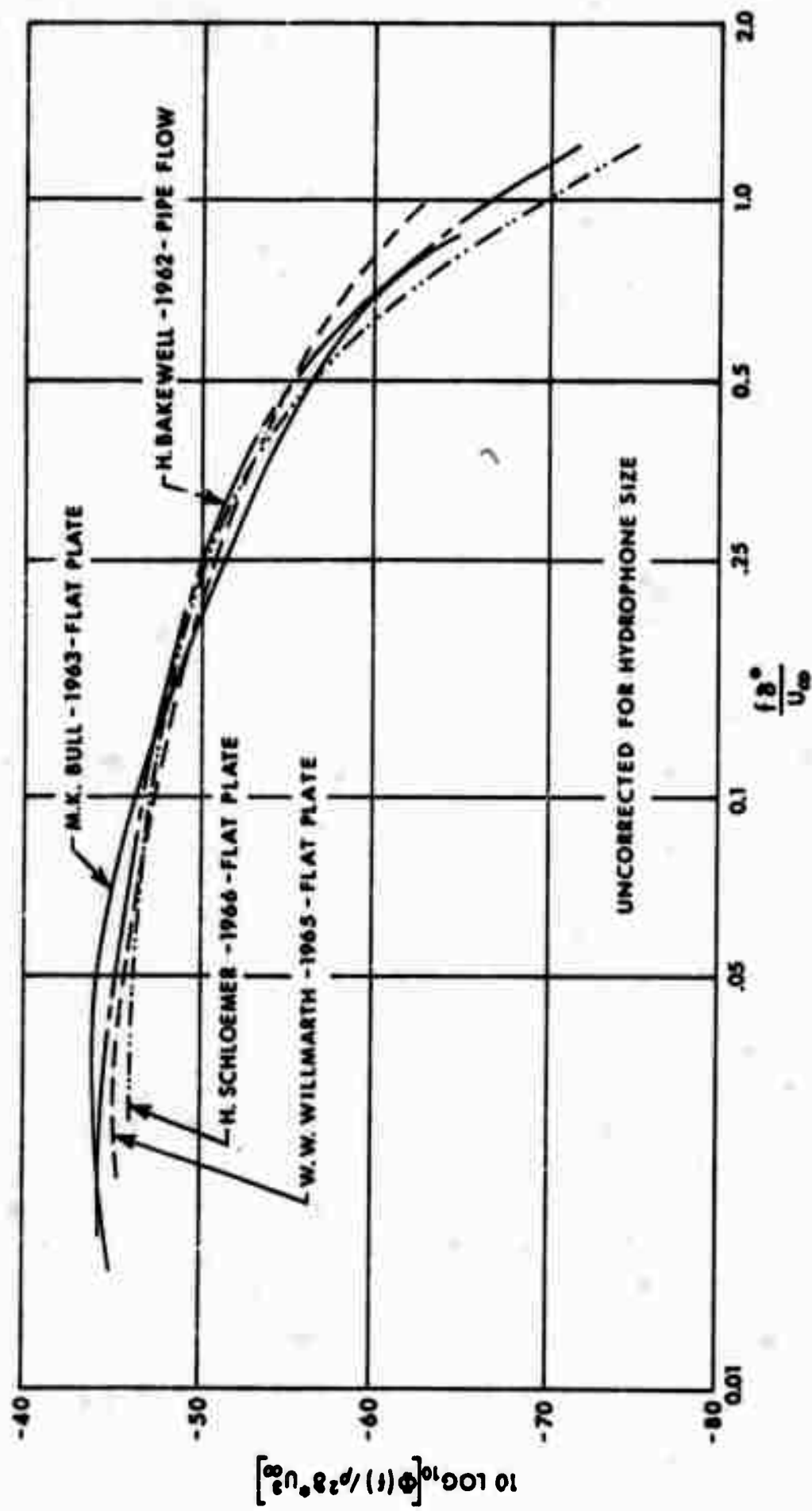


Figure 23. Comparison of Non-Dimensional Spectral Density for the Zero Pressure Gradient to Other Investigators

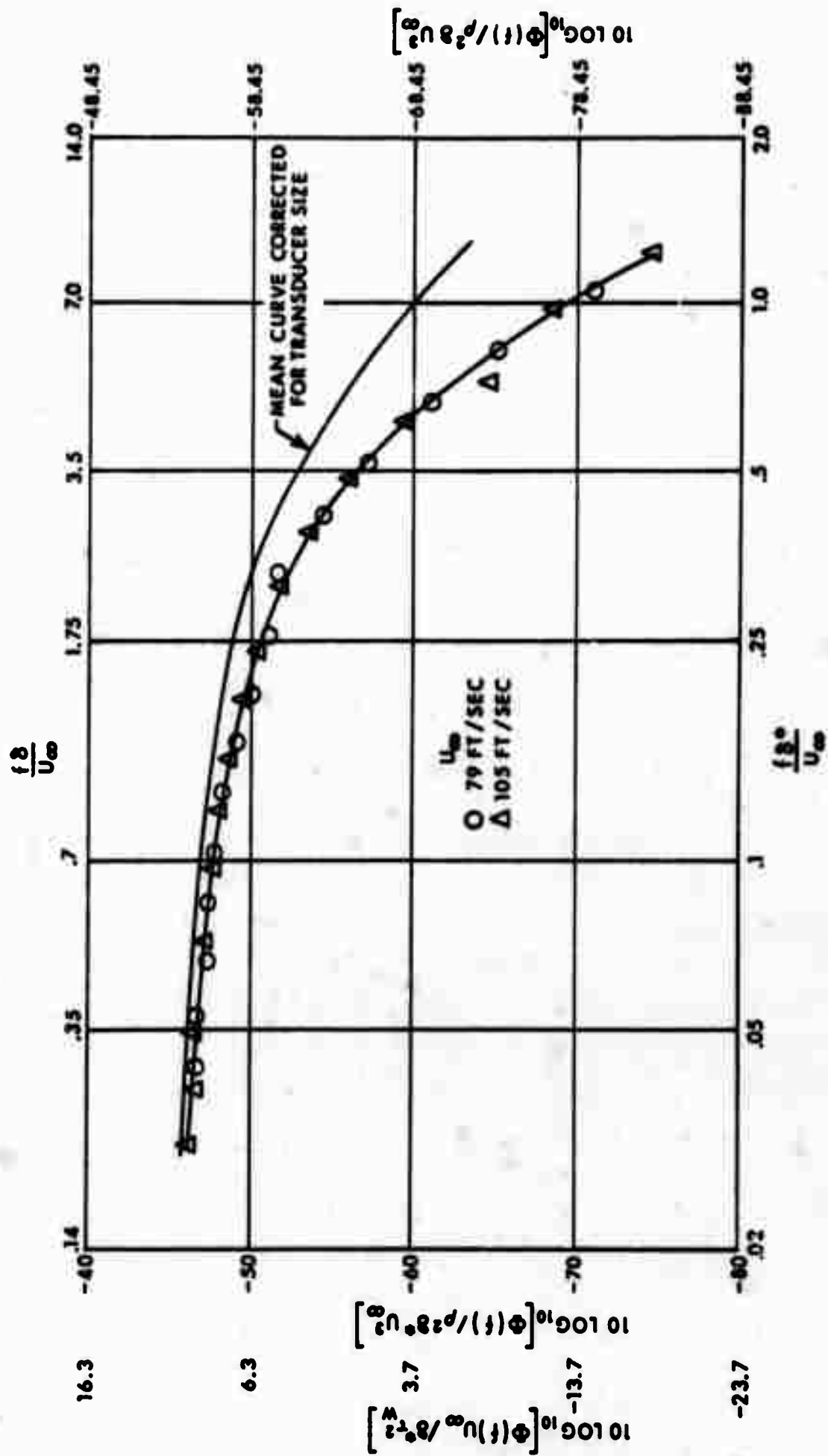


Figure 24. Non-Dimensional Spectral Density for the Zero Pressure Gradient

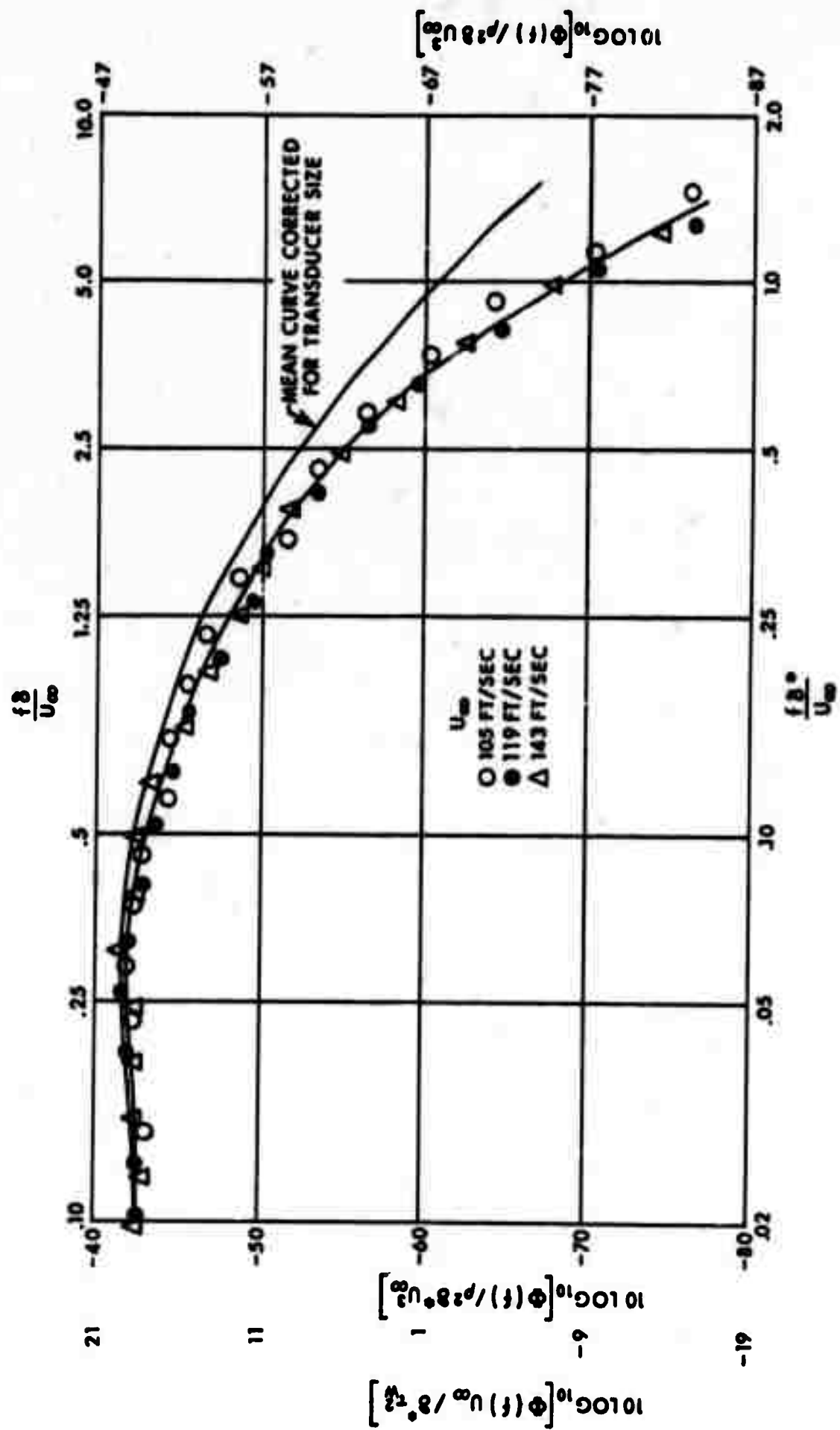


Figure 25. Non-Dimensional Spectral Density for the Adverse Pressure Gradient

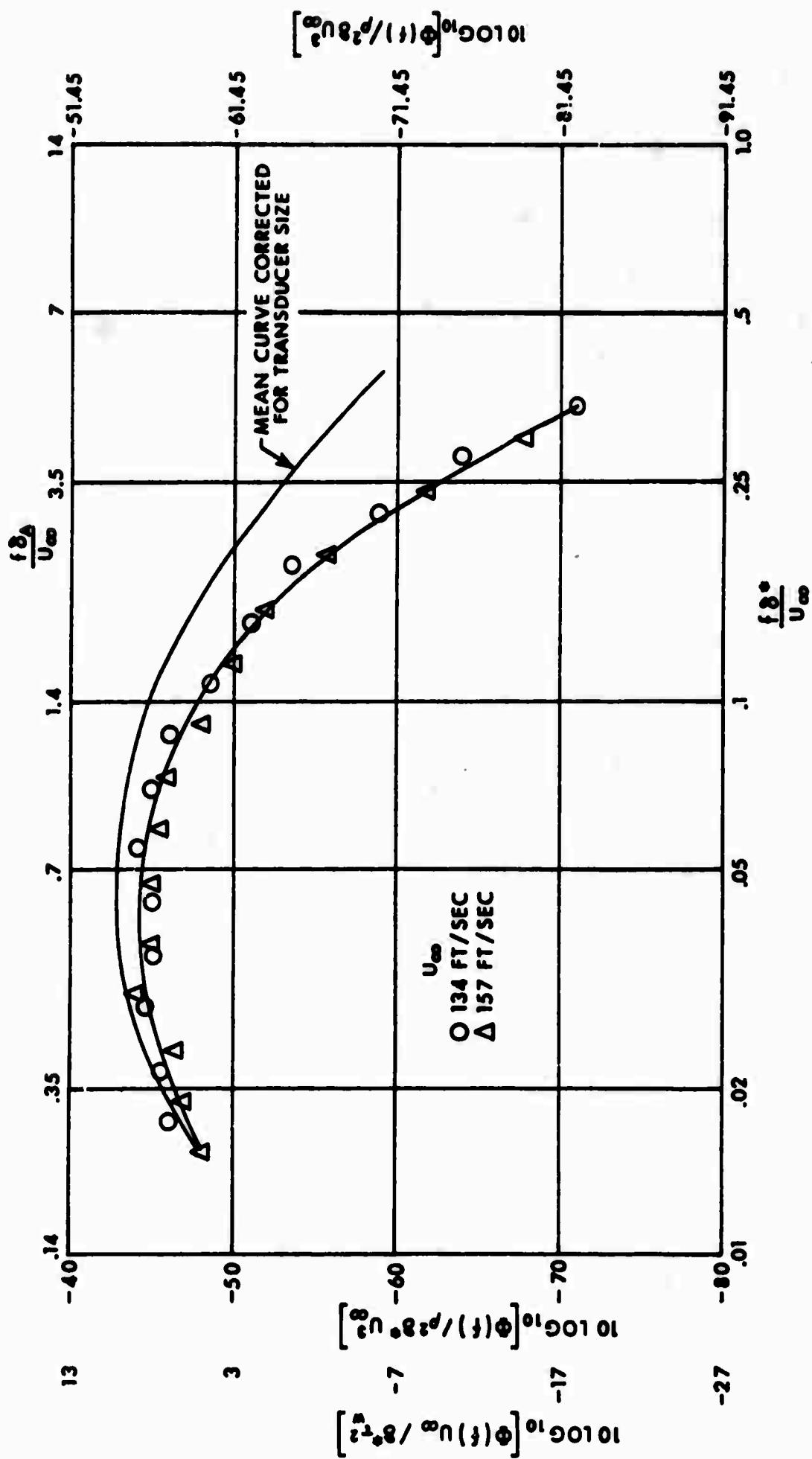


Figure 26. Non-Dimensional Spectral Density for the Favorable Pressure Gradient

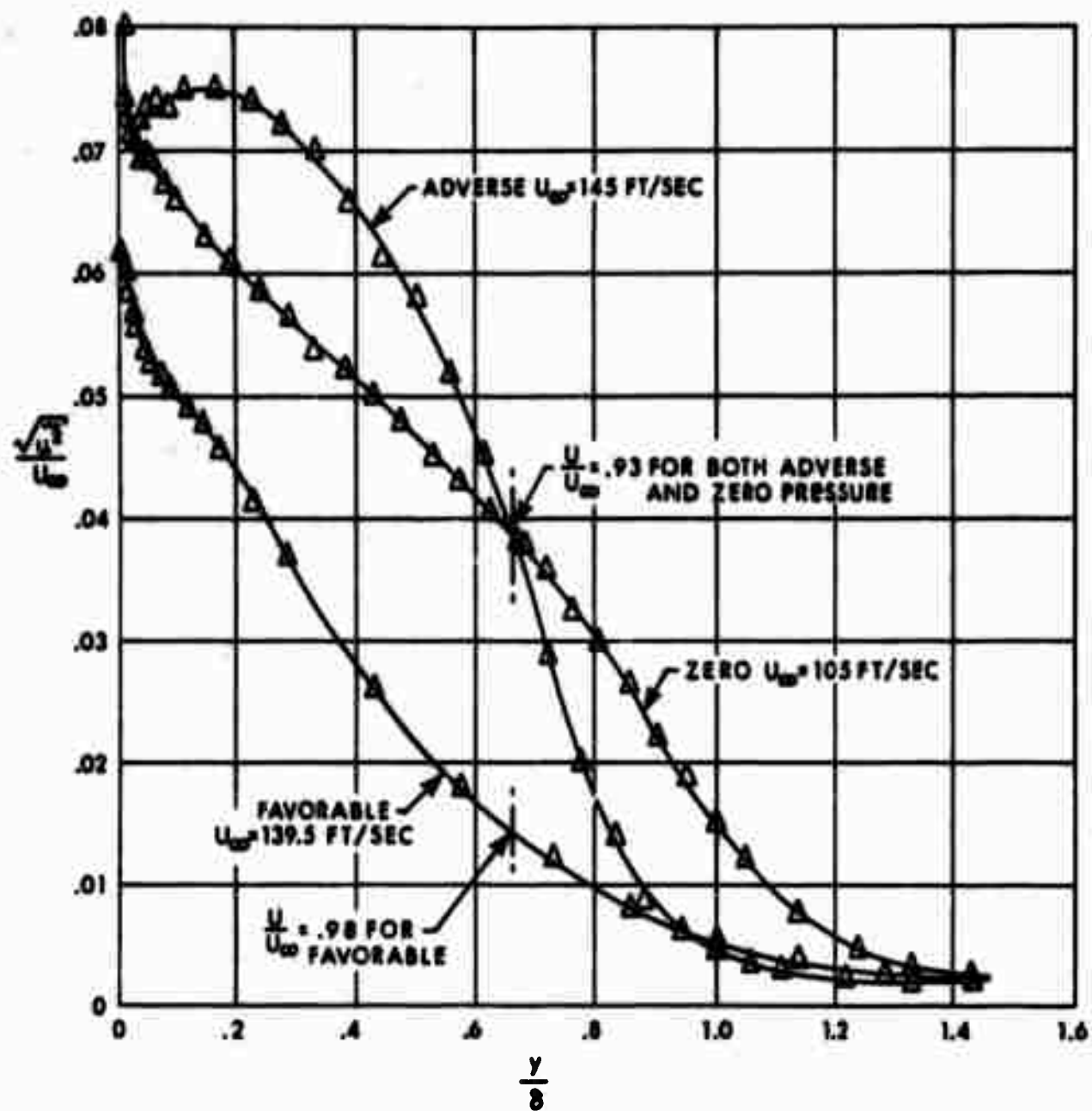


Figure 27. Longitudinal Turbulence Intensity Profiles in the Zero, Adverse and Favorable Pressure Gradients



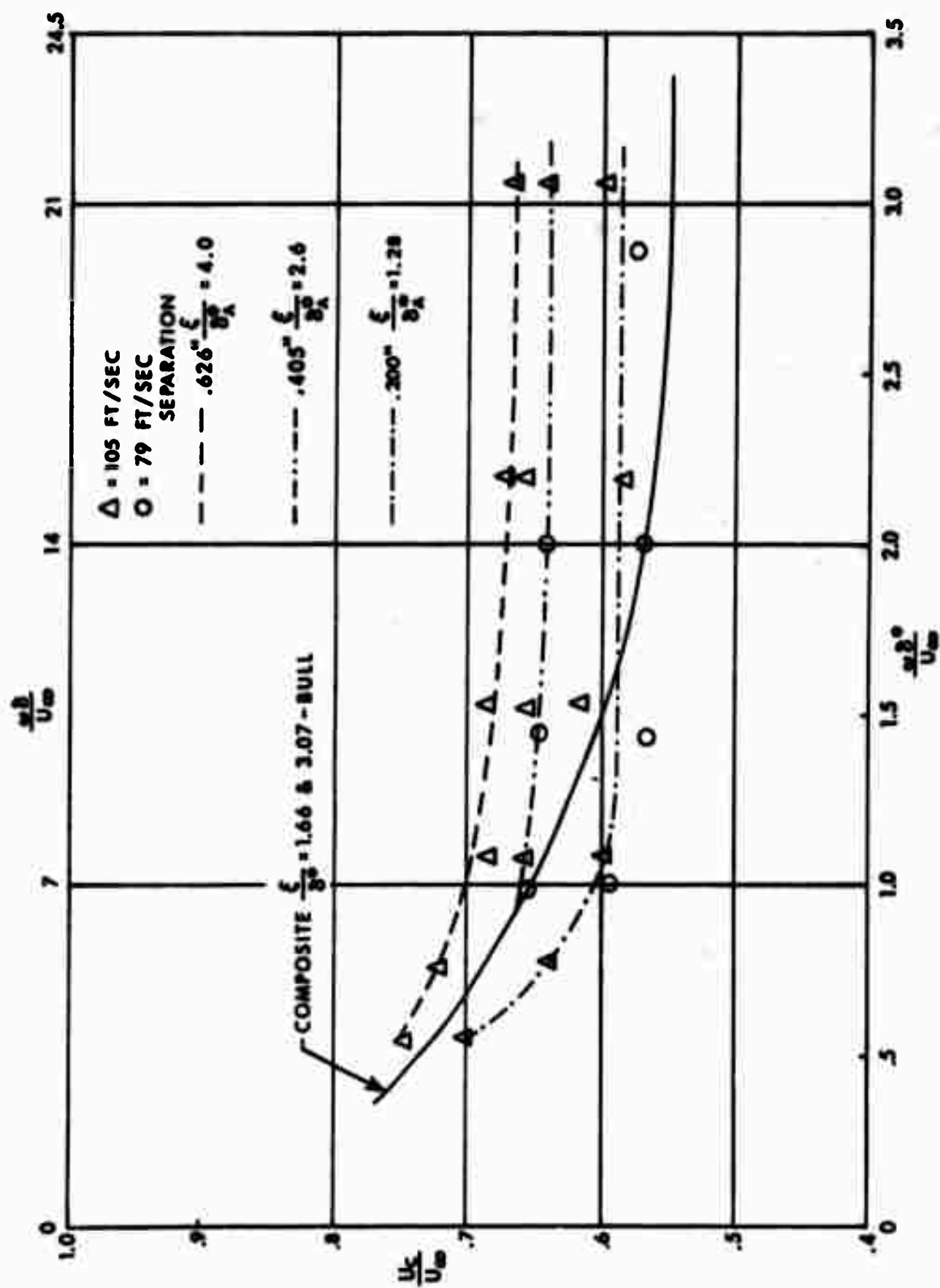


Figure 28. Convection Velocities as a Function of Frequency at Different Longitudinal Separations for the Zero Pressure Gradients

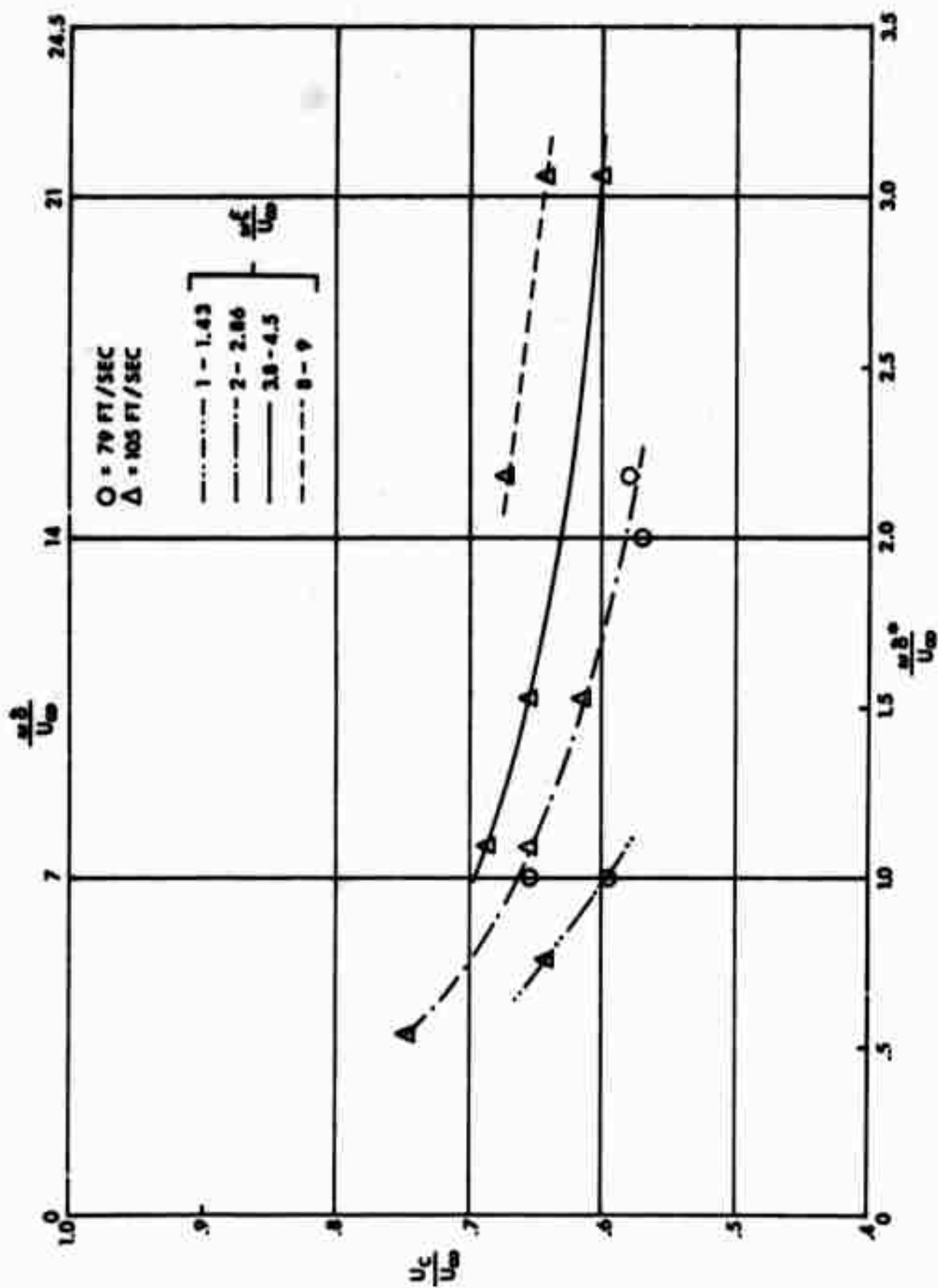


Figure 29. Convection Velocities as a Function of Frequency and Non-Dimensional Longitudinal Separation for the Zero-Pressure Gradient

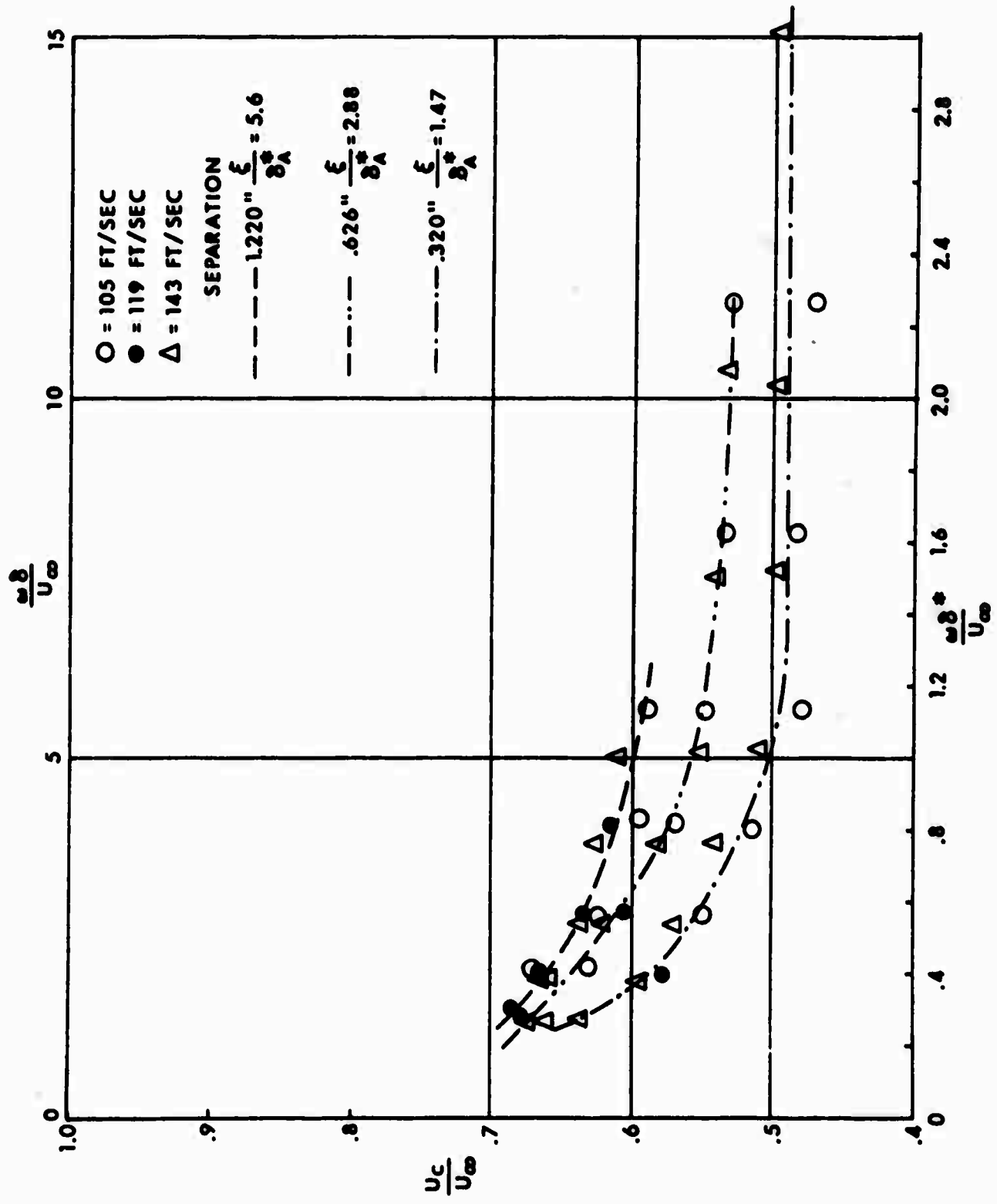


Figure 30. Convection Velocities as a Function of Frequency at Different Longitudinal Separations for the Adverse Pressure Gradient

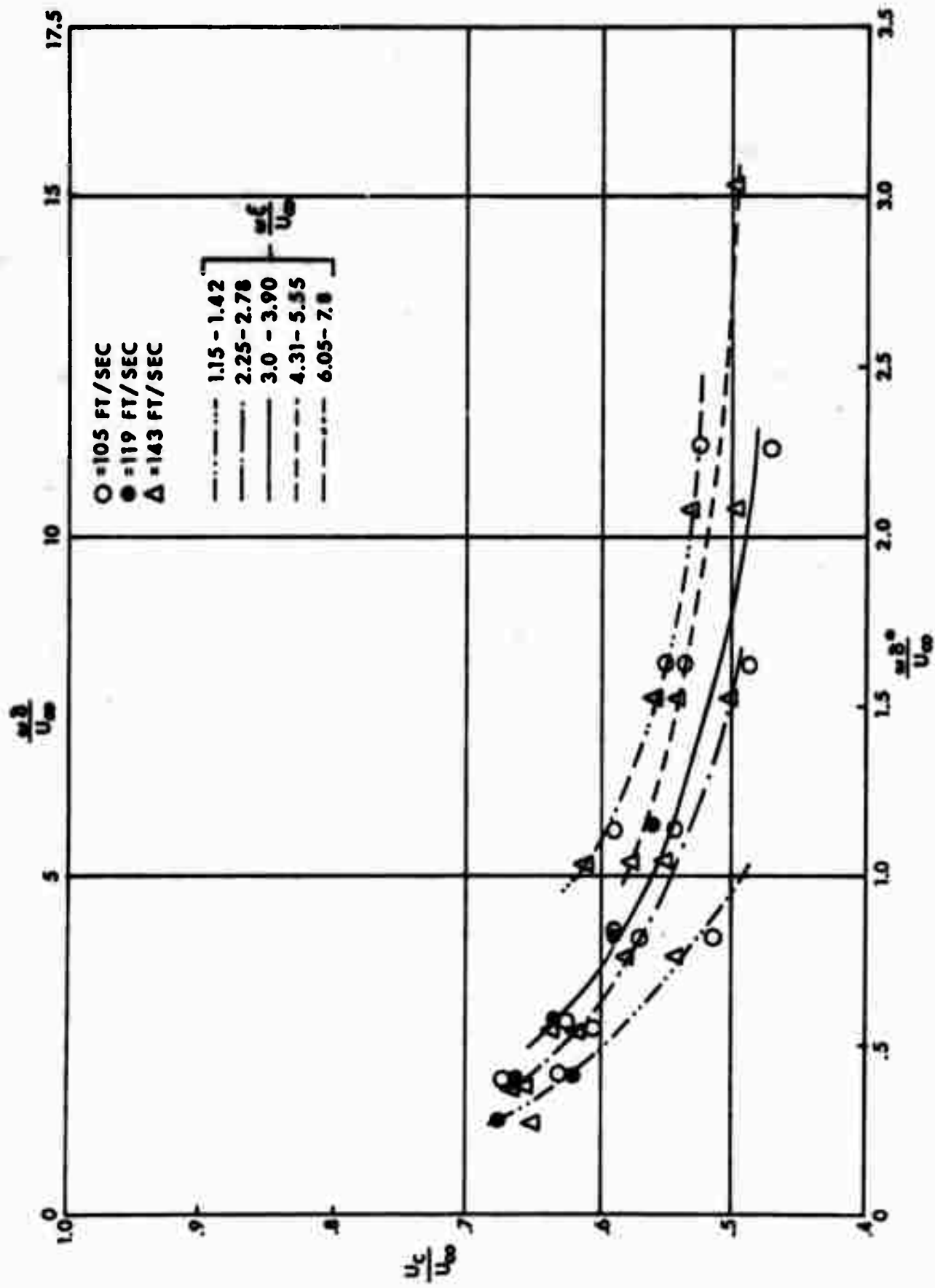


Figure 31. Convection Velocities as a Function of Frequency and Non-Dimensional Longitudinal Separations for the Adverse Pressure Gradient

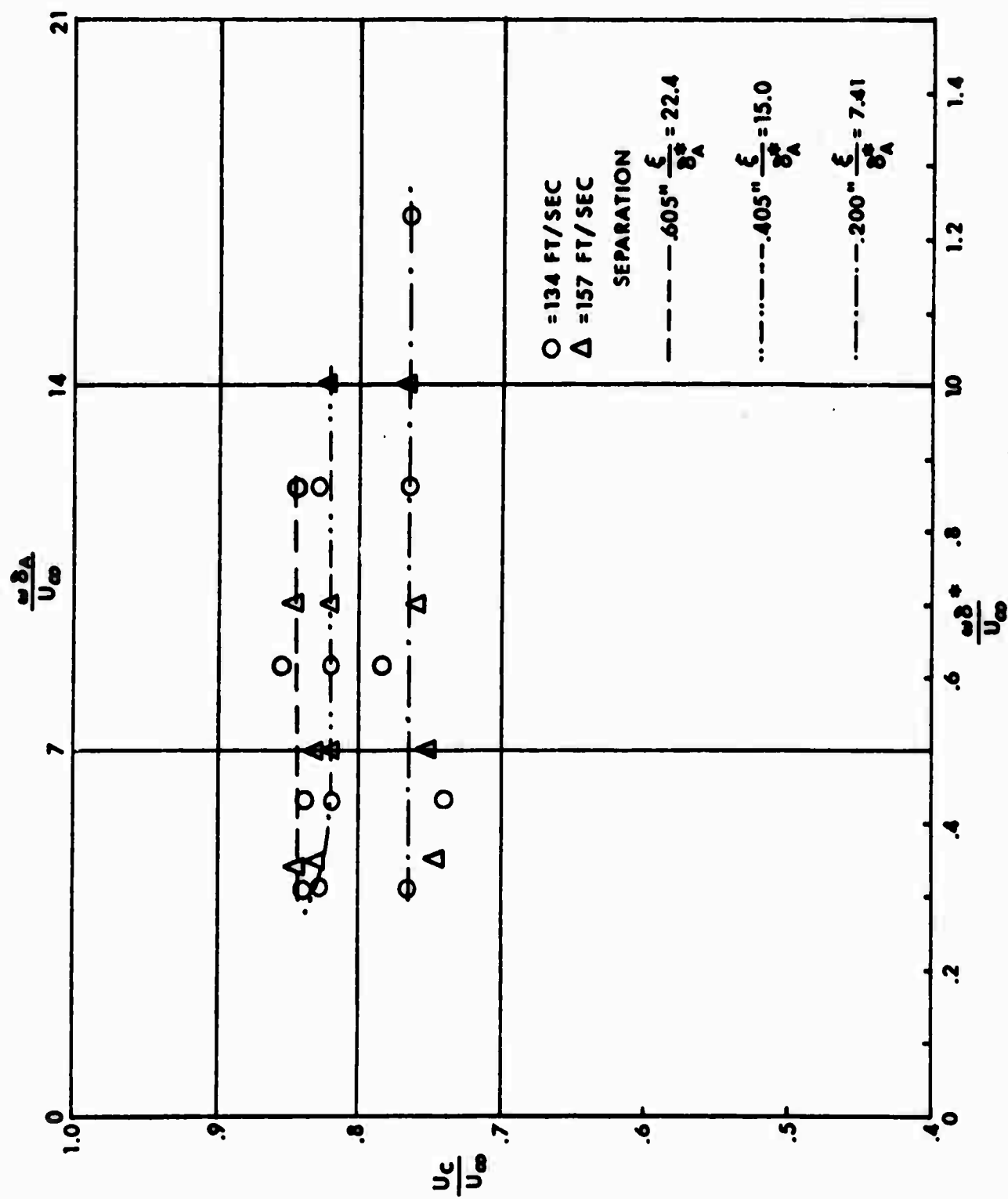


Figure 32. Convection Velocities as a Function of Frequency at Different Longitudinal Separations for the Favorable Pressure Gradient

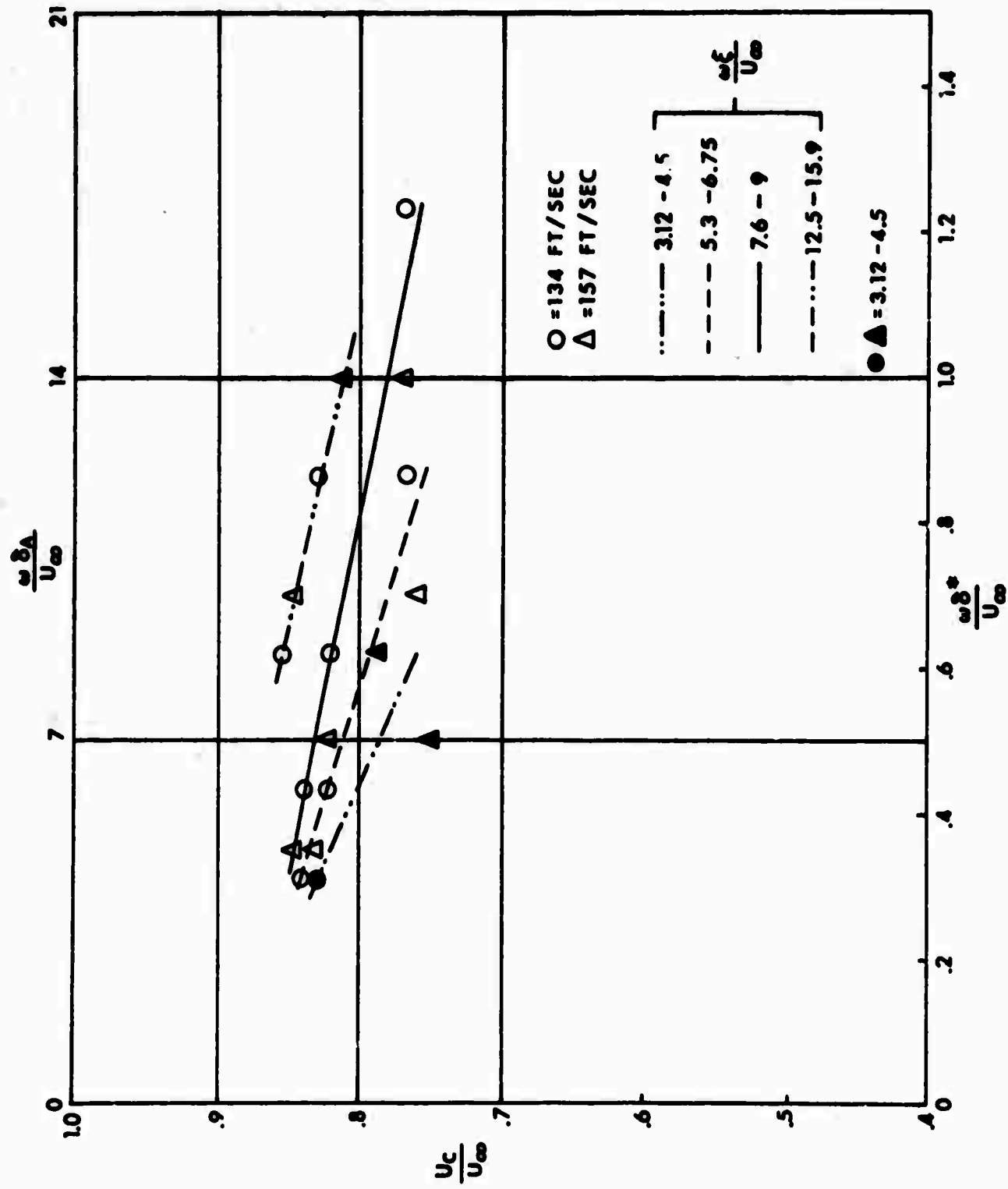


Figure 33. Convection Velocities as a Function of Frequency and Non-Dimensional Longitudinal Separation for the Favorable Pressure Gradient

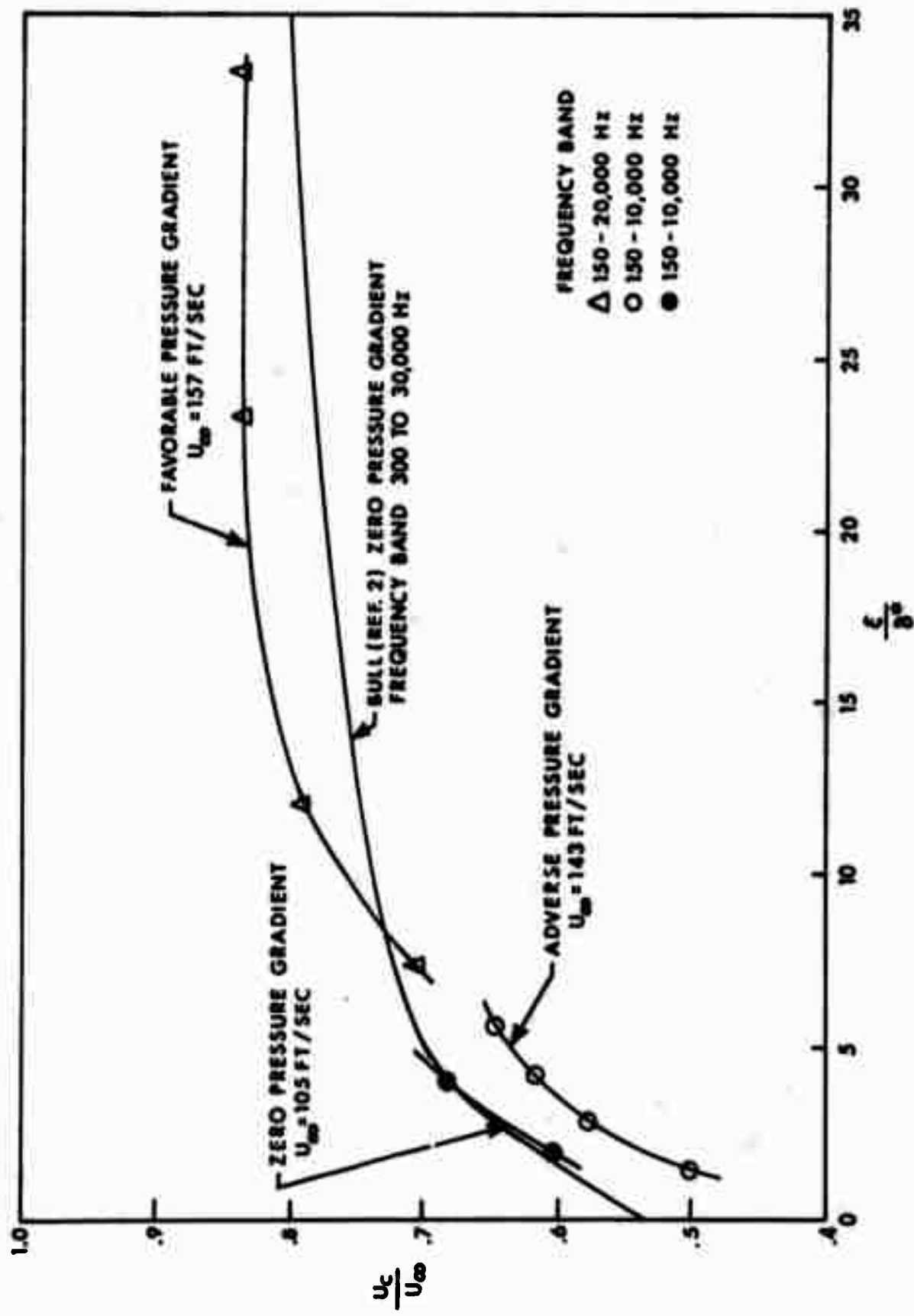


Figure 34. Broad-Band Convection Velocities as a Function of Pressure Gradient and Longitudinal Separation

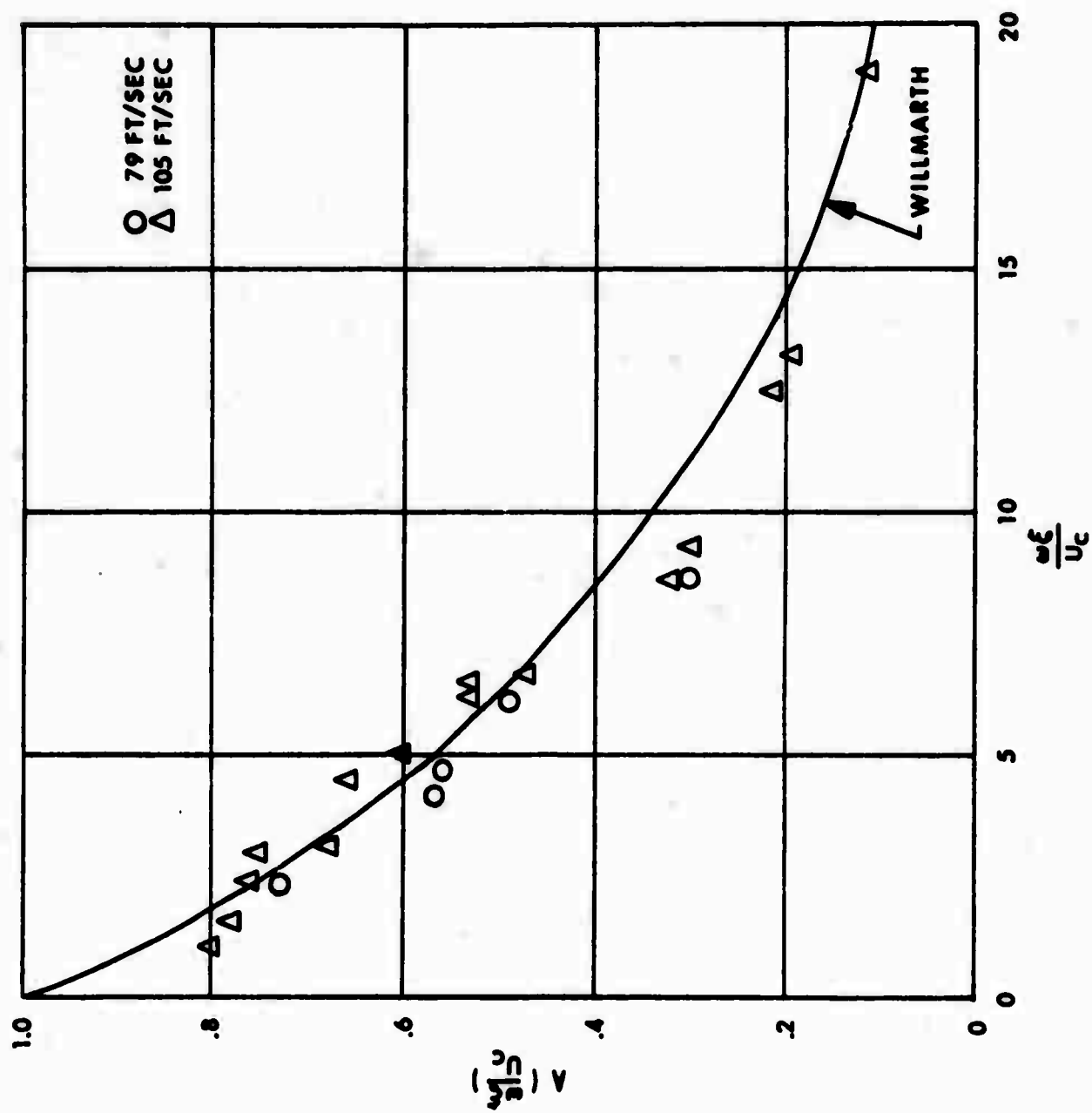


Figure 35. Magnitude of the Normalized Longitudinal Cross-Spectral Density for the Zero Pressure Gradient



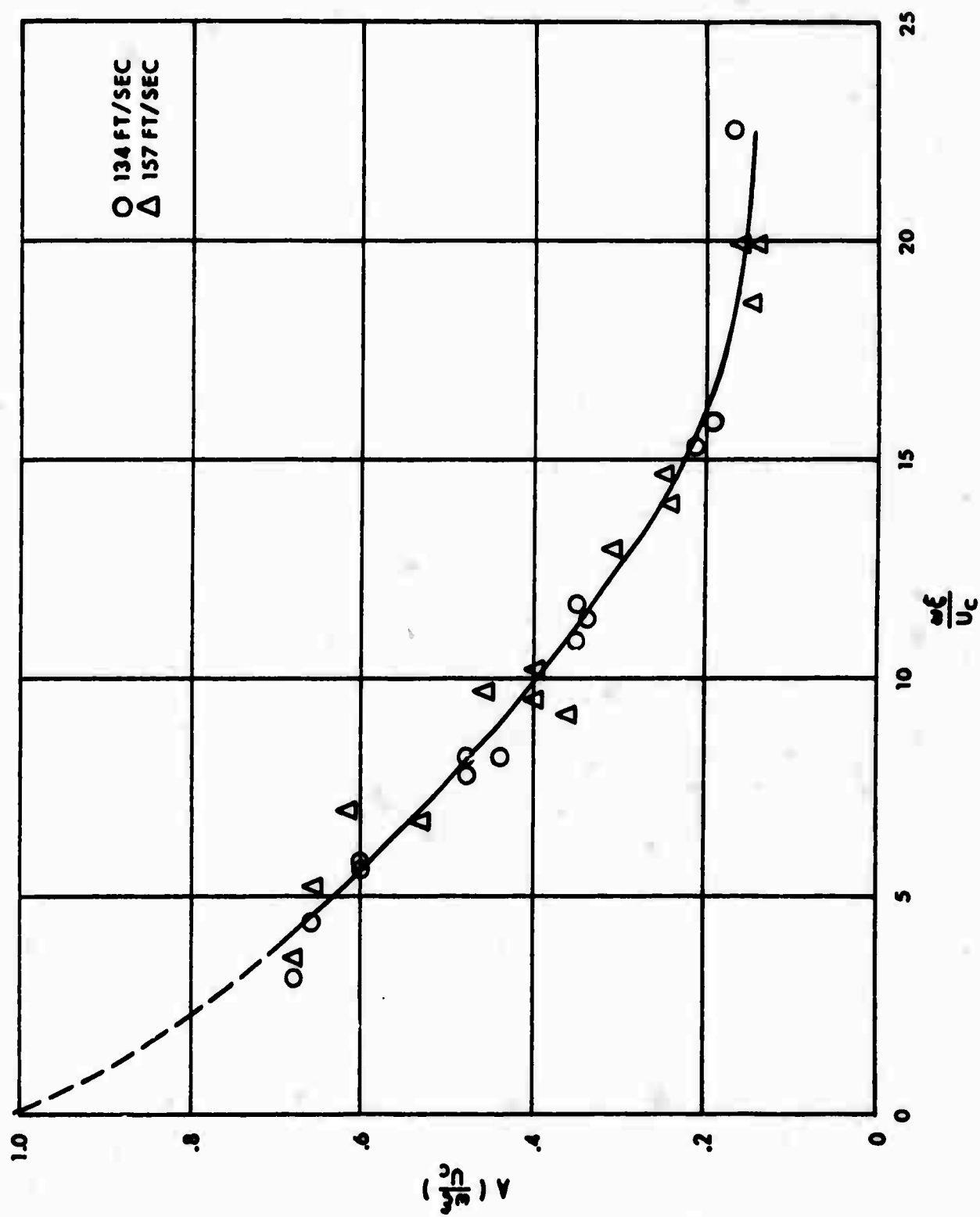


Figure 36. Magnitude of the Normalized Longitudinal Cross-Spectral Density for the Favorable Pressure Gradient

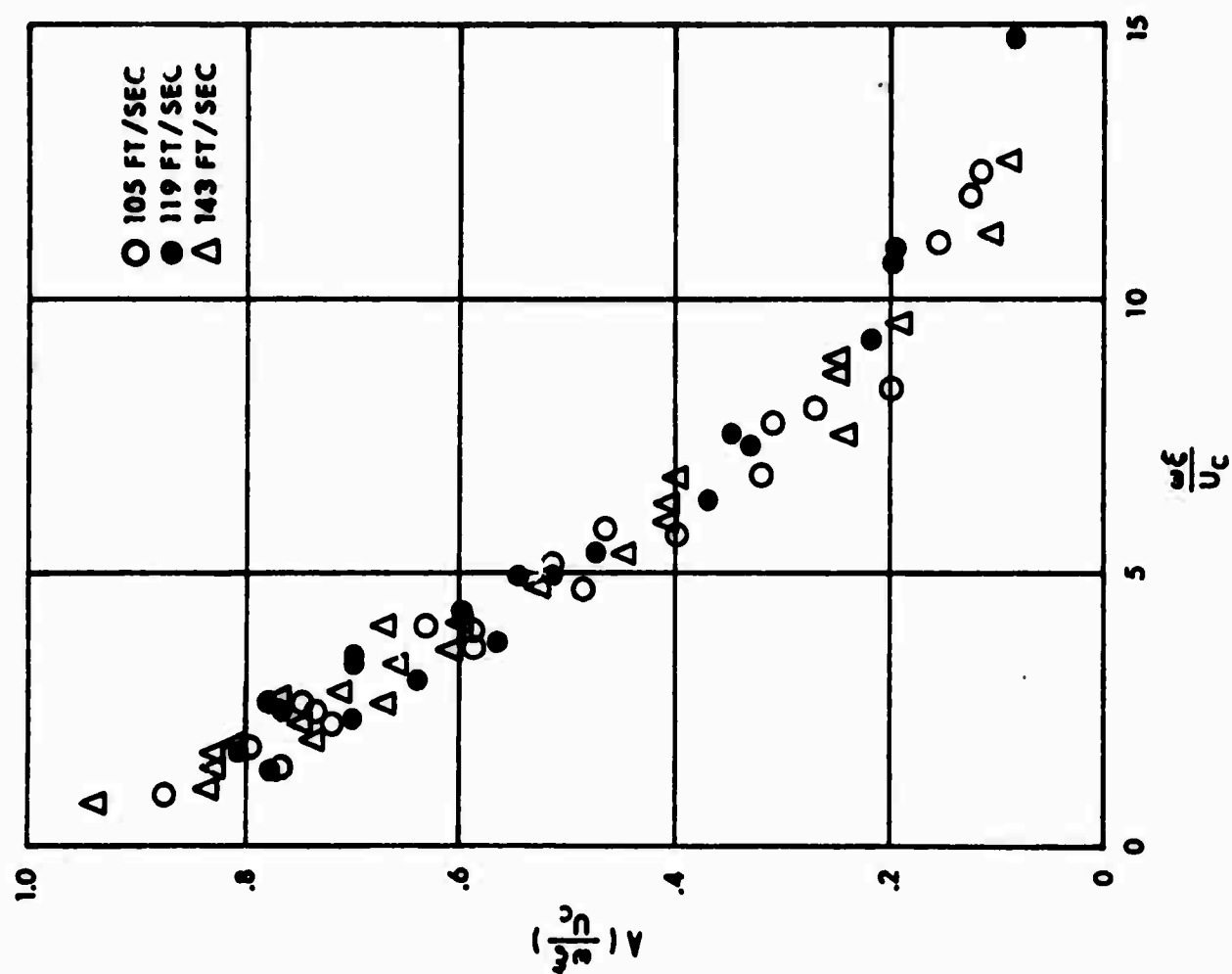


Figure 37. Magnitude of the Normalized Longitudinal Cross-Spectral Density for the Adverse Pressure Gradient

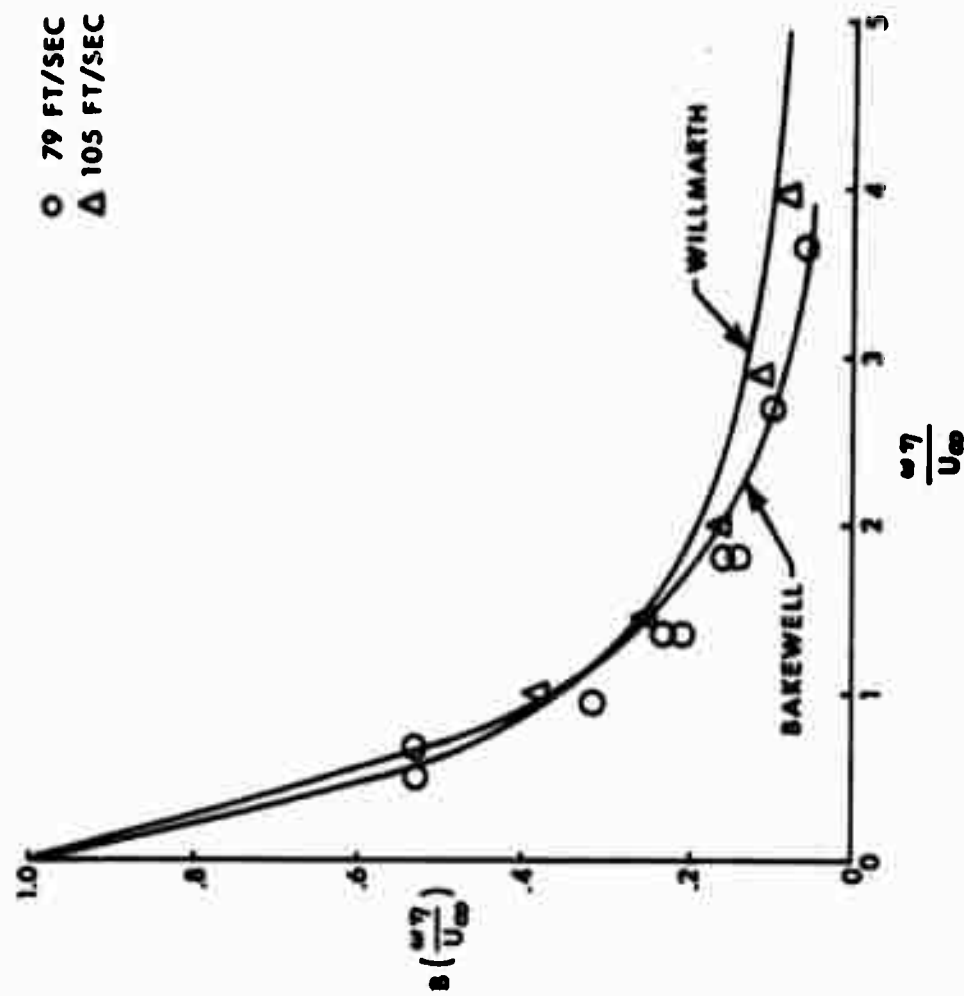


Figure 38. Magnitude of the Normalized Lateral Cross-Spectral Density for the Zero Pressure Gradient

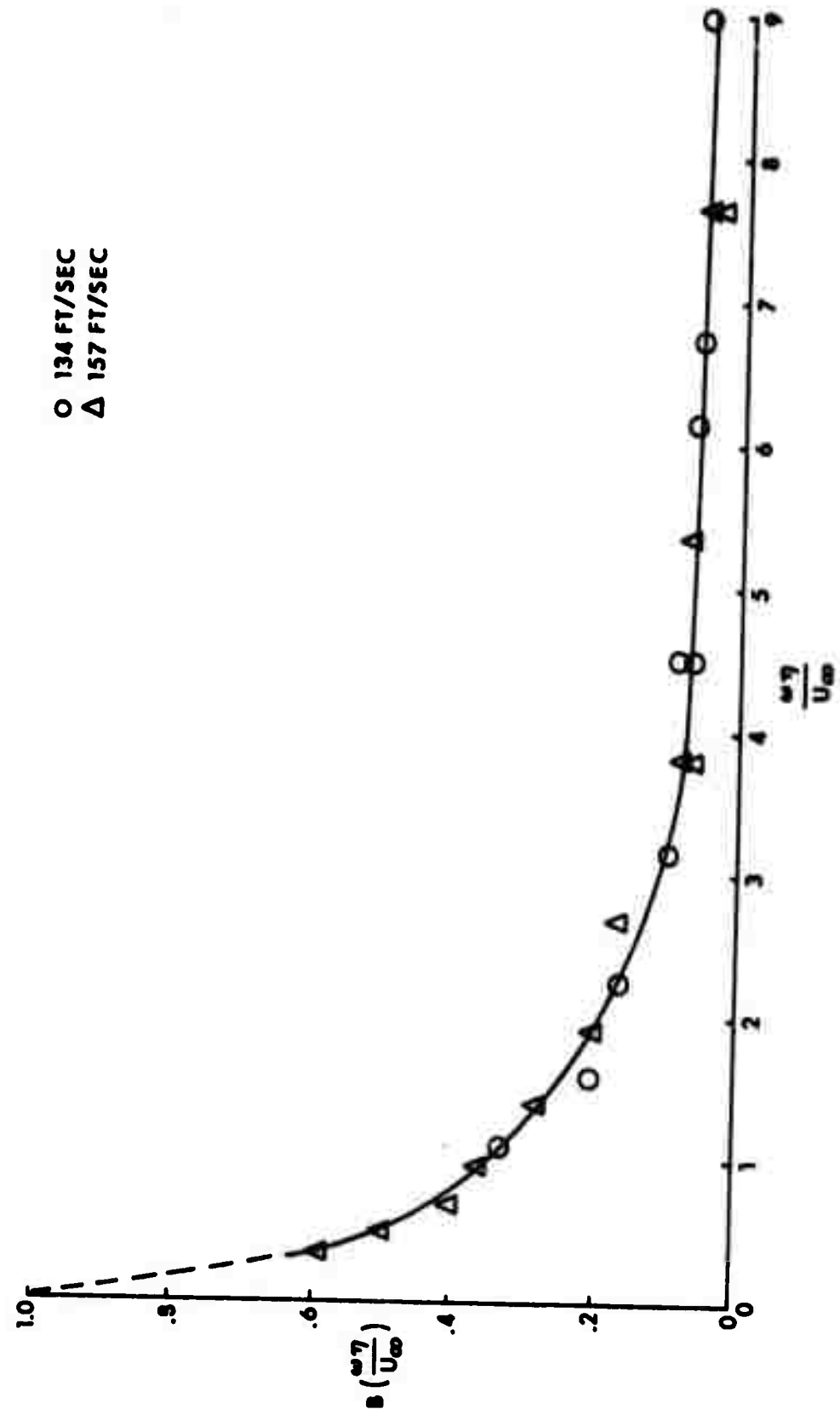


Figure 39. Magnitude of the Normalized Lateral Cross-Spectral Density for the Favorable Pressure Gradient

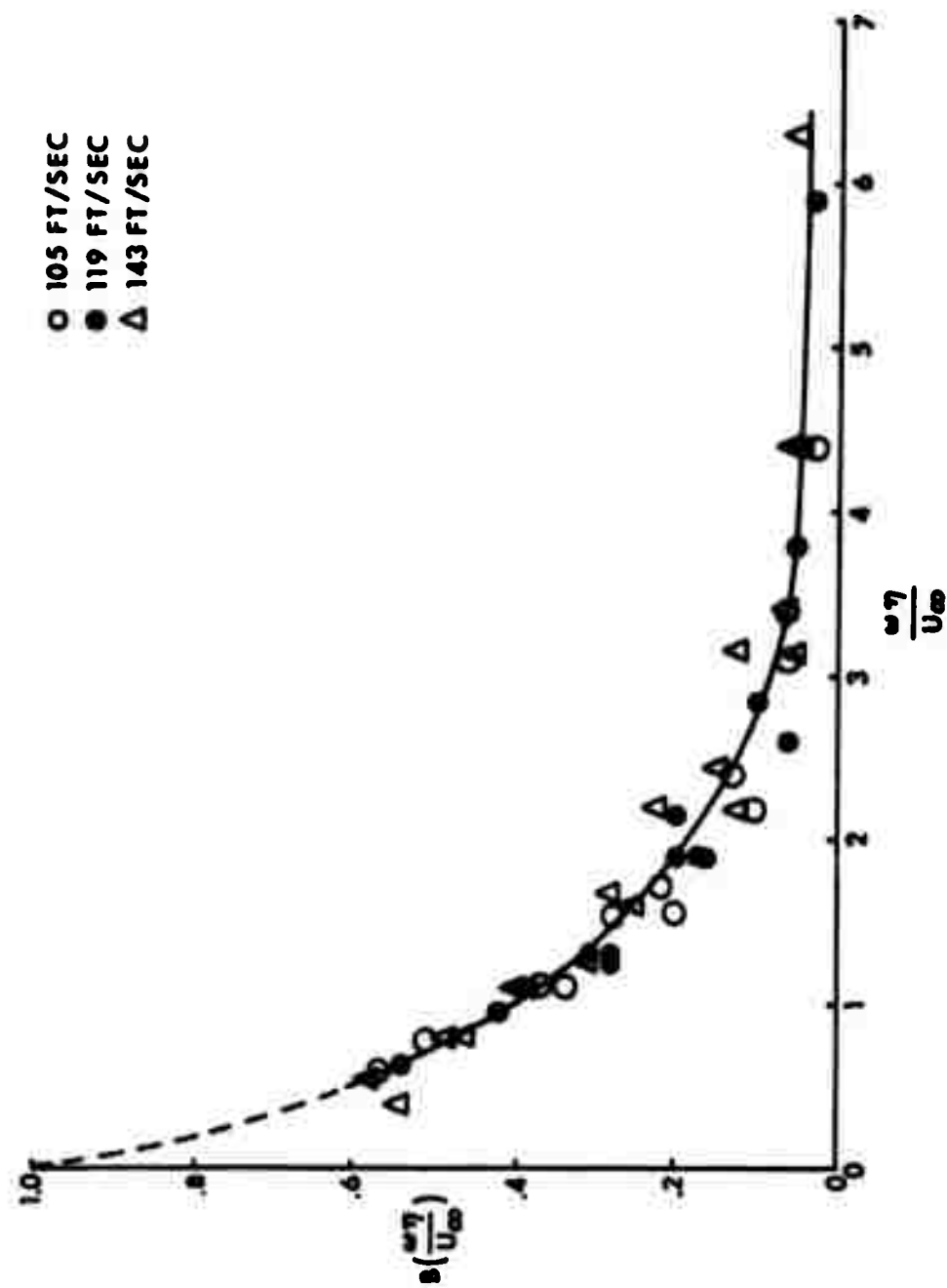


Figure 40. Magnitude of the Normalized Lateral Cross-Spectral Density for the Adverse Pressure Gradient

## LIST OF REFERENCES

1. W. W. Willmarth and C. E. Wooldridge, "Measurements of the Fluctuating Pressure at the Wall Beneath a Thick Turbulent Boundary Layer," Journal of Fluid Mechanics, vol 14, part 2, pp.187-210, 1962.
2. M. K. Bull, Properties of the Fluctuating Wall-Pressure Field of a Turbulent Boundary Layer, Advisory Group for Aeronautical Research and Development, North Atlantic Treaty Organization, Report No. 455 April 1963.
3. E. J. Skudrzyk and G. P. Haddle, "Noise Production in a Turbulent Boundary Layer by Smooth and Rough Surfaces," Journal of the Acoustical Society of America vol. 32, no. 1 pp. 19-34, January 1960.
4. H. P. Bakewell, G. F. Carey, J. J. Libuha, H. H. Schloemer, and W. A. VonWinkle, Wall Pressure Correlations in Turbulent Pipe Flow, USL Report No. 559, August 1962.
5. G. M. Corcos, Pressure Fluctuations in Shear Flows, University of California Institute of Engineering Research, series 183, no. 2, July 1962.
6. M. K. Bull and J. L. Willis, Some Results of Experimental Investigations of the Surface Pressure Field due to a Turbulent Boundary Layer, University of Southampton A.A.S.U. Rep. no. 199, 1961.
7. W. A. VonWinkle, Some Measurements of Longitudinal Space-Time Correlations of Wall Pressure Fluctuations in Turbulent Pipe Flow, Ph.D. Thesis, University of California, 1960.
8. J. S. Murphy, D. A. Bies, W. W. Speaker, and P. A. Franken, Wind Tunnel Investigation of Turbulent Boundary Layer Noise as Related to Design Criteria for High Performance Vehicles NASA TND-2247, April 1964.
9. M. J. Lighthill, "On Sound Generated Aerodynamically I - General Theory," Proceedings of the Royal Society (London), series A, vol 211, no. 1107, 20 March 1952, pp. 564-587.
10. M. J. Lighthill "On Sound Generated Aerodynamically II - Turbulence as a Source of Sound," Proceedings of the Royal Society (London), series A, vol 222, no. 1184, 23 February 1954, pp.1-32.
11. R. H. Kraichnan, "Pressure Fluctuations in Turbulent Flow over a Flat Plate," Journal of the Acoustical Society of America, vol 28, no. 3, May 1956, pp 378-390.

## LIST OF REFERENCES (cont)

12. G. M. Lilley and T. H. Hodgson, On Surface Pressure Fluctuations in Turbulent Boundary Layers, Advisory Group for Aeronautical Research and Development, North Atlantic Treaty Organization, Report no. 276, April 1960.
13. F. M. White, A Unified Theory of Turbulent Wall Pressure Fluctuations, USL Report no. 629, December 1964.
14. S. Gardner, Surface Pressure Fluctuations Produced by Boundary Layer Turbulence, Technical Research Group, Inc., Report no. TRG-142-TN-63-5, October 1963.
15. F. M. White, Private Communication
16. E. L. Rakowsky, The Effect of Free Stream Oscillations on the Incompressible Turbulent Boundary Layer on a Flat Plate with Pressure Gradients, D. Sc. Thesis, Stevens Institute of Technology, (to be published).
17. L. L. Beranek, Noise Reduction, McGraw Hill Book Company, Inc., New York, chap. 17, 1960.
18. F. H. Clauser, "Turbulent Boundary Layers in Adverse Pressure Gradients," Journal of the Aeronautical Sciences, vol. 21, no. 2, pp. 91-108, 1954.
19. J. M. Robertson, A Turbulence Primer, Illinois Engineering Experiment Station Circular no. 79.
20. D. Coles, "The Law of the Wake in the Turbulent Boundary Layer," Journal of Fluid Mechanics, vol. 1, pp. 191-226, 1956.
21. A. P. Peterson and E. E. Gross, Jr., Handbook of Noise Measurements, General Radio Company, West Concord, Mass., 1963.
22. W. W. Willmarth, "Corrigendum: Measurements of the Fluctuating Pressure at the Wall Beneath a Thick Turbulent Boundary Layer," Journal of Fluid Mechanics, vol 21, part 1, pp 107-109, 1965.
23. V. A. Sandborn and R. J. Slogar, Study of the Momentum Distribution of Turbulent Boundary Layers in Adverse Pressure Gradients, NACA, TN 3264, January 1955.
24. G. B. Schubauer and P. S. Klebanoff, Investigation of Separation of the Turbulent Boundary Layer, NACA, Report 1030, June 1949.
25. G. M. Corcos, "Resolution of Pressure in Turbulence," Journal of the Acoustical Society of America, vol. 35, no. 2, pp. 192-199, Feb 1963.

## LIST OF REFERENCES (cont)

26. R. B. Gilchrist and W. A. Strawderman, "Experimental Hydrophone-Size Correction Factor for Boundary-Layer Pressure Fluctuations," Journal of the Acoustical Society of America, vol. 38, no. 2, pp. 298-302, August 1965.
27. G. M. Corcos, "The Structure of the Turbulent Pressure Field in Boundary-Layer Flows," Journal of Fluid Mechanics, vol. 18, part 3, pp 353-378, 1965.
28. C. E. Wooldridge and W. W. Willmarth, "Measurements of the Correlation Between the Fluctuating Velocities and the Fluctuating Wall Pressure in a Thick Turbulent Boundary Layer," The University of Michigan, College of Engineering Report 02920-2-T, April 1962.
29. R. E. Rayle, Influence of Orifice Geometry on Static Pressure Measurements, Paper 59-A-234 presented at the 1959 Annual Meeting of The American Society of Mechanical Engineers.



UNCLASSIFIED

Security Classification

DOCUMENT CONTROL DATA - R&D		
(Security classification of title, body of abstract and indexing annotation must be entered when the overall report is classified)		
1. ORIGINATING ACTIVITY (Corporate author)		2a. REPORT SECURITY CLASSIFICATION
U. S. Navy Underwater Sound Laboratory Fort Trumbull, New London, Connecticut		UNCLASSIFIED
		2b. GROUP
3. REPORT TITLE		
EFFECTS OF PRESSURE GRADIENTS ON TURBULENT BOUNDARY-LAYER WALL-PRESSURE FLUCTUATIONS		
4. DESCRIPTIVE NOTES (Type of report and inclusive dates)		
Research Report		
5. AUTHOR(S) (Last name, first name, initial)		
Schloemer, Howard H.		
6. REPORT DATE	7a. TOTAL NO. OF PAGES	7b. NO. OF REFS
1 July 1966	85	29
8a. CONTRACT OR GRANT NO.	8a. ORIGINATOR'S REPORT NUMBER(S)	
b. PROJECT NO.	747	
c.	9b. OTHER REPORT NO(S) (Any other numbers that may be assigned this report)	
d.		
10. AVAILABILITY/LIMITATION NOTICES		
Distribution of this document is unlimited.		
11. SUPPLEMENTARY NOTES		12. SPONSORING MILITARY ACTIVITY
		U. S. Navy
13. ABSTRACT The low-turbulence subsonic wind tunnel at Stevens Institute of Technology was significantly modified so that turbulent boundary-layer pressure fluctuation measurements could be made with adequate signal-to-noise ratio over a wide frequency range. Measurements were made in a mild adverse and a mild favorable pressure gradient with natural transition occurring in the boundary layer. To make certain that the facility was operating correctly and to establish a basis for comparison, the zero-pressure gradient case was investigated. For this case, the spectral density, magnitude of the normalized longitudinal and lateral cross-spectral density functions, and convection velocity as a function of longitudinal separation and frequency were in excellent agreement with other experimenters. When comparison is made to the zero-pressure gradient in the same non-dimensionalized frequency band and at similar non-dimensionalized longitudinal spacings, the convection velocity ratio is higher in the favorable and lower in the adverse pressure gradients, primarily due to the change in shape of the mean velocity profile. As in the zero-pressure gradient case, the increase in convection velocity with increasing longitudinal separation and decrease with increasing frequency was observed for both the adverse and favorable pressure gradient. The longitudinal decay of a particular frequency component was more rapid for the adverse gradient and slower for the favorable gradient than for the zero-pressure gradient, as indicated by the magnitude of the normalized longitudinal cross-spectral density measured for each gradient. Within the experimental accuracy of the measurements no differences were found for the magnitude of the normalized lateral cross-spectral density due to the pressure gradients imposed. The effect of an adverse pressure gradient on the non-dimensionalized spectral density is to increase the low-frequency content without influencing the high-frequency portion appreciably, when compared to the zero-pressure gradient case. As expected the root-mean-square values (for a broad frequency band) are greater in the adverse pressure gradient when non-dimensionalized with respect to free stream dynamic pressure. The major change due to the favorable pressure gradient is a sharp decrease in the high-frequency content, with a resultant lowering of the root-mean-square values. The spectral densities were corrected for finite pressure transducer size, using Corcos' correction factors. Qualitative agreement with theoretical predictions by White, as to the effects of favorable and adverse pressure gradients, was found for convection velocities, including the effects of spatial separations and frequency, and the general shape of the magnitude of the normalized longitudinal and lateral cross-spectral density curves.		

DD FORM 1473  
1 JAN 64

UNCLASSIFIED

Security Classification

14. KEY WORDS	LINK A		LINK B		LINK C	
	ROLE	WT	ROLE	WT	ROLE	WT
Pressure Gradients Boundary Layer, Turbulent Wall-pressure Fluctuations						

#### INSTRUCTIONS

1. **ORIGINATING ACTIVITY:** Enter the name and address of the contractor, subcontractor, grantee, Department of Defense activity or other organization (*corporate author*) issuing the report.

2a. **REPORT SECURITY CLASSIFICATION:** Enter the overall security classification of the report. Indicate whether "Restricted Data" is included. Marking is to be in accordance with appropriate security regulations.

2b. **GROUP:** Automatic downgrading is specified in DoD Directive 5200.10 and Armed Forces Industrial Manual. Enter the group number. Also, when applicable, show that optional markings have been used for Group 3 and Group 4 as authorized.

3. **REPORT TITLE:** Enter the complete report title in all capital letters. Titles in all cases should be unclassified. If a meaningful title cannot be selected without classification, show title classification in all capitals in parenthesis immediately following the title.

4. **DESCRIPTIVE NOTES:** If appropriate, enter the type of report, e.g., interim, progress, summary, annual, or final. Give the inclusive dates when a specific reporting period is covered.

5. **AUTHOR(S):** Enter the name(s) of author(s) as shown on or in the report. Enter last name, first name, middle initial. If military, show rank and branch of service. The name of the principal author is an absolute minimum requirement.

6. **REPORT DATE:** Enter the date of the report as day, month, year; or month, year. If more than one date appears on the report, use date of publication.

7a. **TOTAL NUMBER OF PAGES:** The total page count should follow normal pagination procedures, i.e., enter the number of pages containing information.

7b. **NUMBER OF REFERENCES:** Enter the total number of references cited in the report.

8a. **CONTRACT OR GRANT NUMBER:** If appropriate, enter the applicable number of the contract or grant under which the report was written.

8b, 8c, & 8d. **PROJECT NUMBER:** Enter the appropriate military department identification, such as project number, subproject number, system numbers, task number, etc.

9a. **ORIGINATOR'S REPORT NUMBER(S):** Enter the official report number by which the document will be identified and controlled by the originating activity. This number must be unique to this report.

9b. **OTHER REPORT NUMBER(S):** If the report has been assigned any other report numbers (*either by the originator or by the sponsor*), also enter this number(s).

10. **AVAILABILITY/LIMITATION NOTICES:** Enter any limitations on further dissemination of the report, other than those

imposed by security classification, using standard statements such as:

- (1) "Qualified requesters may obtain copies of this report from DDC."
- (2) "Foreign announcement and dissemination of this report by DDC is not authorized."
- (3) "U. S. Government agencies may obtain copies of this report directly from DDC. Other qualified DDC users shall request through \_\_\_\_\_."
- (4) "U. S. military agencies may obtain copies of this report directly from DDC. Other qualified users shall request through \_\_\_\_\_."
- (5) "All distribution of this report is controlled. Qualified DDC users shall request through \_\_\_\_\_."

If the report has been furnished to the Office of Technical Services, Department of Commerce, for sale to the public, indicate this fact and enter the price, if known.

11. **SUPPLEMENTARY NOTES:** Use for additional explanatory notes.

12. **SPONSORING MILITARY ACTIVITY:** Enter the name of the departmental project office or laboratory sponsoring (*paying for*) the research and development. Include address.

13. **ABSTRACT:** Enter an abstract giving a brief and factual summary of the document indicative of the report, even though it may also appear elsewhere in the body of the technical report. If additional space is required, a continuation sheet shall be attached.

It is highly desirable that the abstract of classified reports be unclassified. Each paragraph of the abstract shall end with an indication of the military security classification of the information in the paragraph, represented as (TS), (S), (C), or (U).

There is no limitation on the length of the abstract. However, the suggested length is from 150 to 225 words.

14. **KEY WORDS:** Key words are technically meaningful terms or short phrases that characterize a report and may be used as index entries for cataloging the report. Key words must be selected so that no security classification is required. Identifiers, such as equipment model designation, trade name, military project code name, geographic location, may be used as key words but will be followed by an indication of technical context. The assignment of links, roles, and weights is optional.